



# NAVAL POSTGRADUATE SCHOOL

MONTEREY, CALIFORNIA

## THESIS

### **SENSOR MODEL REQUIREMENTS FOR TAWS/IRTSS OPERATION**

by

Rachel Hughes

September 2007

Advisors:

Andreas Goroeh  
Kenneth Davidson

**Approved for public release; distribution is unlimited**

THIS PAGE INTENTIONALLY LEFT BLANK

<b>REPORT DOCUMENTATION PAGE</b>			<i>Form Approved OMB No. 0704-0188</i>	
Public reporting burden for this collection of information is estimated to average 1 hour per response, including the time for reviewing instruction, searching existing data sources, gathering and maintaining the data needed, and completing and reviewing the collection of information. Send comments regarding this burden estimate or any other aspect of this collection of information, including suggestions for reducing this burden, to Washington headquarters Services, Directorate for Information Operations and Reports, 1215 Jefferson Davis Highway, Suite 1204, Arlington, VA 22202-4302, and to the Office of Management and Budget, Paperwork Reduction Project (0704-0188) Washington DC 20503.				
<b>1. AGENCY USE ONLY (Leave blank)</b>		<b>2. REPORT DATE</b> September 2007	<b>3. REPORT TYPE AND DATES COVERED</b> Master's Thesis	
<b>4. TITLE AND SUBTITLE</b> Sensor Model Requirements for TAWS/IRTSS Operation			<b>5. FUNDING NUMBERS</b>	
<b>6. AUTHOR(S)</b> Rachel Hughes				
<b>7. PERFORMING ORGANIZATION NAME(S) AND ADDRESS(ES)</b> Naval Postgraduate School Monterey, CA 93943-5000			<b>8. PERFORMING ORGANIZATION REPORT NUMBER</b>	
<b>9. SPONSORING /MONITORING AGENCY NAME(S) AND ADDRESS(ES)</b> N/A			<b>10. SPONSORING/MONITORING AGENCY REPORT NUMBER</b>	
<b>11. SUPPLEMENTARY NOTES</b> The views expressed in this thesis are those of the author and do not reflect the official policy or position of the Department of Defense or the U.S. Government.				
<b>12a. DISTRIBUTION / AVAILABILITY STATEMENT</b> Approved for public release; distribution is unlimited			<b>12b. DISTRIBUTION CODE</b>	
<b>13. ABSTRACT (maximum 200 words)</b> Possible improvements to the minimum resolvable temperature difference (MRTD) entered into TAWS are considered. FLIR92 is modified to include atmospheric turbulence that depends on height in the atmosphere. Resultant MRTDs are compared to the operational FLIR92 MRTD predictions excluding atmospheric turbulence. The difference in the MRTD is only apparent in the higher frequency regime and is less than 0.05% of the MRTD values for a typical test case. MRTD is calculated by FLIR92 and NVThermIP over desert and marine locations and the resultant MRTDs entered into TAWS to compare maximum detection range. NVThermIP yielded a larger maximum detection range by up to 1.5% over the desert and 2% over water.				
<b>14. SUBJECT TERMS</b> TAWS, FLIR92, NVThermIP, Atmospheric Turbulence, MRTD			<b>15. NUMBER OF PAGES</b> 123	
			<b>16. PRICE CODE</b>	
<b>17. SECURITY CLASSIFICATION OF REPORT</b> Unclassified	<b>18. SECURITY CLASSIFICATION OF THIS PAGE</b> Unclassified	<b>19. SECURITY CLASSIFICATION OF ABSTRACT</b> Unclassified	<b>20. LIMITATION OF ABSTRACT</b> UU	

NSN 7540-01-280-5500

Standard Form 298 (Rev. 2-89)  
Prescribed by ANSI Std. Z39-18

THIS PAGE INTENTIONALLY LEFT BLANK

Approved for public release; distribution is unlimited

# **SENSOR MODEL REQUIREMENTS FOR TAWS/IRTSS OPERATION**

Rachel Hughes  
Second Lieutenant, United States Air Force  
B.S., Houghton College, 2003

Submitted in partial fulfillment of the  
requirements for the degree of

**MASTER OF SCIENCE IN METEOROLOGY**

from the

**NAVAL POSTGRADUATE SCHOOL  
September 2007**

Author: Rachel Hughes

Approved by: Dr. Andreas Goroch  
Co-Advisor

Dr. Kenneth Davidson  
Co-Advisor

Dr. Philip Durkee  
Chairman, Department of Meteorology

THIS PAGE INTENTIONALLY LEFT BLANK

# ABSTRACT

Possible improvements to the minimum resolvable temperature difference (MRTD) entered into TAWS are considered. FLIR92 is modified to include atmospheric turbulence that depends on height in the atmosphere. Resultant MRTDs are compared to the operational FLIR92 MRTD predictions excluding atmospheric turbulence. The difference in the MRTD is only apparent in the higher frequency regime and is less than 0.05% of the MRTD values for a typical test case. MRTD is calculated by FLIR92 and NVThermIP over desert and marine locations and the resultant MRTDs entered into TAWS to compare maximum detection range. NVThermIP yielded a larger maximum detection range by up to 1.5% over the desert and 2% over water.

THIS PAGE INTENTIONALLY LEFT BLANK



# TABLE OF CONTENTS

<b>I.</b>	<b>INTRODUCTION . . . . .</b>	<b>1</b>
A.	MOTIVATION FOR COMPARISON . . . . .	1
1.	Current Status of TAWS . . . . .	1
2.	Differences Between FLIR92 and NVThermIP . . . . .	2
3.	Advantages and Disadvantages of FLIR92 . . . . .	4
4.	Advantages and Disadvantages of NVThermIP . . . . .	5
5.	Phenomena Missing from FLIR92 and NVThermIP . . . . .	6
B.	MOTIVATION TO TEST IMPORTANCE OF OPTICAL TUR- BULENCE . . . . .	6
C.	PROJECT OVERVIEW . . . . .	7
1.	Comparison Parameters . . . . .	7
2.	Comparisons in TAWS . . . . .	8
<b>II.</b>	<b>THERMAL IMAGING SYSTEMS PERFORMANCE MODELS</b>	<b>9</b>
A.	FLIR92 . . . . .	9
1.	MTFs Included in FLIR92 . . . . .	9
2.	Sampling . . . . .	23
3.	System Noise . . . . .	25
4.	Calculating the Predicted MRTD . . . . .	30
5.	Calculating the Predicted MDTD . . . . .	32
6.	MRTD and MDTD Temperature Dependence . . . . .	33
7.	Johnson Criteria and FLIR92 . . . . .	33
B.	NVTHERMIP . . . . .	34
1.	MTFs Included in NVThermIP . . . . .	34
2.	Sampling . . . . .	40
3.	System Noise . . . . .	41
4.	Calculating the Predicted MRTD . . . . .	43

5.	Detector Cooling in NVThermIP . . . . .	44
6.	Targeting Task Performance (TTP) Metric and NVThermIP . . . . .	45
<b>III.</b>	<b>OPTICAL TURBULENCE MODEL CHOICE . . . . .</b>	<b>47</b>
A.	OPTICAL TURBULENCE AND ATMOSPHERIC $C_N^2$ . . . . .	47
1.	Turbulence Near the Ground . . . . .	49
2.	Turbulence Above the Surface Layer . . . . .	51
3.	Turbulence Through Whole Atmosphere . . . . .	52
B.	MTF FOR OPTICAL TURBULENCE . . . . .	54
<b>IV.</b>	<b>METHODS AND DATA SETS . . . . .</b>	<b>59</b>
A.	SELECTION OF DATA LOCATIONS . . . . .	59
B.	SELECTION OF ATMOSPHERIC DATA . . . . .	59
C.	SELECTION OF TARGET LOCATIONS . . . . .	60
D.	PROCEDURES . . . . .	60
1.	Parameters Used in Calculations . . . . .	60
2.	FLIR92 Calculations . . . . .	60
3.	NVThermIP Calculations . . . . .	62
4.	TAWS Calculations . . . . .	62
<b>V.</b>	<b>RESULTS . . . . .</b>	<b>63</b>
A.	ATMOSPHERIC TURBULENCE IN FLIR92 . . . . .	63
B.	COMPARING FLIR92 AND NVTHERMIP . . . . .	65
1.	Comparing Resultant MRTDs . . . . .	65
2.	Comparing Detection Range . . . . .	66
3.	Comparing Marine/Desert Conditions . . . . .	68
<b>VI.</b>	<b>CONCLUSIONS AND RECOMMENDATIONS . . . . .</b>	<b>77</b>
A.	CONCLUSIONS FLIR92 WITH/WITHOUT ATMOSPHERIC TURBULENCE . . . . .	77
B.	CONCLUSIONS FLIR92 VERSUS NVTHERMIP . . . . .	78
C.	RECOMMENDATIONS . . . . .	79

APPENDIX A. GOODMAN DERIVATION FOR LONG EXPOSURE	81
APPENDIX B. EXACT FORM EYE/BRAIN SPATIAL INTEGRATION . . . . .	91
APPENDIX C. TEMPERATURE SCALING OF $\sigma_{TVH}$ . . . . .	93
APPENDIX D. TABLES OF INPUTS TO FLIR92, NVTHERMIP	95
APPENDIX E. ACRONYMS USED . . . . .	101
LIST OF REFERENCES . . . . .	103
INITIAL DISTRIBUTION LIST . . . . .	105

THIS PAGE INTENTIONALLY LEFT BLANK

# LIST OF FIGURES

1.	Horizontal and Vertical Directions with Respect to a 4-Bar Target. . .	8
2.	Diffraction Limited MTF in the Horizontal Direction. . . . .	11
3.	Geometric Blur MTF in the Horizontal Direction. . . . .	12
4.	Detector Spatial MTF in the Horizontal Direction. . . . .	13
5.	Random Motion MTF in the Horizontal Direction. . . . .	16
6.	Zeroth Order Bessel Function . . . . .	17
7.	Display MTF. . . . .	19
8.	Display Sample and Hold MTF in the Horizontal Direction. . . . .	21
9.	Eye/Brain Response MTF. . . . .	22
10.	Horizontal System Noise MTF. . . . .	23
11.	Horizontal System MTF. . . . .	24
12.	System MRTD showing the Horizontal and Vertical Results. . . . .	31
13.	Comparing the Eye MTF in FLIR92 and NVThermIP in the Horizontal Direction. . . . .	39
14.	Comparison of the Bulk and Hufnagel Methods with Sfc Temp 28°C. .	54
15.	Comparison of the Bulk and Hufnagel Methods at White Sands. . . .	55
16.	Comparison of the Bulk and Hufnagel Methods at Pt Conception. . . .	56
17.	Goodman Long Exposure Atmospheric Turbulence MTF. . . . .	57
18.	Comparison of the Goodman MTF at Different Slant Angles. . . . .	58
19.	Horiz Difference Between MRTD Curves for Modified, Original FLIR92.	64
20.	Vert Difference Between MRTD Curves for Modified, Original FLIR92.	65
21.	Horizontal MRTD Curves for FLIR92, NVThermIP. . . . .	66
22.	Vertical MRTD Curves for FLIR92, NVThermIP. . . . .	67
23.	Comparing Maximum Detection Range at White Sands using FLIR92, NVThermIP. . . . .	69
24.	Maximum Detection Range for White Sands at Different Probabilities.	70

25.	Comparing Maximum Detection Range at Pt Conception using FLIR92, NVThermIP. . . . .	71
26.	Maximum Detection Range for Pt Conception at Different Probabilities.	72
27.	Comparing Maximum Detection Ranges at White Sands and Pt Con- ception at 35% Prob and 95% Prob. . . . .	73
28.	Comparing Maximum Detection Ranges at White Sands and Pt Con- ception at 35% Prob. . . . .	74
29.	Comparing Maximum Detection Ranges at White Sands and Point Conception at 95% Prob. . . . .	75
30.	Near Surface Behavior of the Bulk Model. . . . .	78
31.	The Kolmogorov and von Kármán Spectra. . . . .	83

# LIST OF TABLES

I.	3-D Noise Component Descriptions in FLIR92 . . . . .	25
II.	3-D Noise Components For Scanning Systems . . . . .	27
III.	3-D Noise Component For Staring Systems . . . . .	27
IV.	NVESD Recommended Settings for Psychophysical Constants . . . . .	31
V.	Ezoom Examples . . . . .	37
VI.	3-D Noise Component Descriptions in NVThermIP . . . . .	41
VII.	Noise Values for Scanning Systems in NVThermIP . . . . .	42
VIII.	Noise Values for Staring Systems in NVThermIP . . . . .	42
IX.	Parameters for $C_n^2$ Test Cases. . . . .	53
X.	Atmospheric Parameters around White Sands. . . . .	60
XI.	Atmospheric Parameters around Point Conception. . . . .	61
XII.	Target Locations. . . . .	61
XIII.	Atmospheric Condition Variables for Input into Modified FLIR92. . . . .	61
XIV.	MRTD for Modified, Original FLIR92 in the horizontal direction. . . . .	63
XV.	MRTD for Modified, Original FLIR92 in the vertical direction. . . . .	64
XVI.	Input Parameters NVThermIP Part I. . . . .	95
XVII.	Input Parameters NVThermIP Part II. . . . .	96
XVIII.	Input Parameters NVThermIP Part III. . . . .	97
XIX.	Input Parameters for FLIR92 Part I. . . . .	98
XX.	Input Parameters for FLIR92 Part II. . . . .	99
XXI.	Acronyms Used in this Study . . . . .	101

THIS PAGE INTENTIONALLY LEFT BLANK



# ACKNOWLEDGMENTS

Thanks to Jon Hixson at the Army Research Lab for informative teleconferences and helpful advice regarding NVThermIP. Thanks also to Prof Alf Cooper at the Naval Postgraduate School for useful insights on sensor operations. Thanks to the team at the Air Force Weather Agency (AFWA) for obtaining and interpreting observational data on very short notice. Particular appreciation to my husband for marshaling the AFWA team and for his thoughtful questions during late-night thesis discussions.

THIS PAGE INTENTIONALLY LEFT BLANK

# I. INTRODUCTION

Target Acquisition Weapons Software (TAWS) is used operationally to predict the performance of electro-optical weapons and their navigation systems. For sensors operating in the infrared (IR) spectral band, the minimum resolvable temperature difference (MRTD) is determined from a desktop computer model such as the Forward Looking Infrared 92 (FLIR92) or the Night Vision Thermal and Image Processing model (NVThermIP). Both models are capable of providing an MRTD, which may be manipulated for use in TAWS, but there are differences in their calculations that become apparent at high and low frequencies. Also, although FLIR92 does not operationally include the effects of atmospheric turbulence, NVThermIP does for limited conditions.

In this study, FLIR92 and NVThermIP are compared in their current operational forms for various atmospheric conditions. Then FLIR92 is modified to include atmospheric turbulence and the two version of FLIR92 are compared for the varied atmospheric conditions.

All acronyms in this report are listed in alphabetical order in Appendix E.

## A. MOTIVATION FOR COMPARISON

### 1. Current Status of TAWS

Currently, the MRTD used in TAWS predictions of target detection by IR sensor is calculated by FLIR92 from basic system parameters. While this has been sufficient for previous iterations of TAWS, recent improvements in model resolution and the image resolution of sensors being modeled suggest that perhaps NVThermIP may be a better choice. NVThermIP incorporates a number of improvements intended to improve the determined MRTDs for the sensors in the extrema of low and high spatial frequencies, in other words for very large and very small targets. NVThermIP also includes optical turbulence, which should improve the MRTD calculation. With

increased sensitivities of sensors, including optical turbulence should improve the MRTD prediction. Since FLIR92 and NVThermIP behave differently at high and low frequencies in marine or desert environments, one model may substantially improve the MRTD calculation, and thus the TAWS predictions, over the other model. In particular, the temperature difference between the surface and the ambient air may influence model calculations and this temperature difference is much greater during the day over a desert.

## 2. Differences Between FLIR92 and NVThermIP

Both FLIR92 and NVThermIP are desktop computer models developed to predict standard summary performance figures of merit for thermal imaging systems. They are PC based programs that model passive sensors which detect emitted and reflected radiation. Using basic system-level parameters, these models calculate the modulation transfer function (MTF), the noise equivalent temperature difference (NETD), the MRTD, and the minimum detectable temperature difference (MDTD) for sensors looking at specific targets. FLIR92 and NVThermIP both predict the MRTD that a human can discriminate when using a thermal imager operationally. NVThermIP also predicts the range at which target acquisition will be successful, using the specified thermal imager. Thus, the output from each model is used to determine whether or not a system will achieve the MTF, system noise, MRTD, and MDTD that is required to effectively perform a given mission. For each mission, the conditions necessary to meet the target acquisition and discrimination requirements may vary.

FLIR92 and NVThermIP share certain basic assumptions. These assumptions are stated in the *NVThermIP User's Manual* (NVESD 2001), and follow the steps of modeling FLIR systems outlined in the *Infrared and Electro-Optical (IREO) Handbook* Vol.4 (1993). All MTFs are assumed to be separable, so the total system MTF is calculated as the product of all sub-system MTFs. This approach reduces calculation complexities because the analysis is simplified to one dimension and cross-terms

are eliminated. However, there is almost always some calculation error associated with assuming separability. This error becomes significant in certain cases such as for diamond-shaped detectors, but is neglected in all FLIR92 and NVThermIP calculations regardless of detector shape and type (NVESD 2001).

An MTF describes the spatial frequency response of a system. It is the contrast at a given spatial frequency compared to the contrast at a lower frequency. The total system MTF is a product of all component MTFs. Each MTF may be calculated as the Fourier transform of the point spread function (PSF) of the component, or the response of the imaging component to a point of light. An imaging system will experience some degradation of the image due to imperfections in the optics, electronics, or even the observer eye and this degradation is what the MTF describes. If some system component did not contribute to the degradation, then the MTF for that component would be unity (Driggers 1999).

Both FLIR92 and NVThermIP assume all blurs to be symmetrical in order to keep all MTFs real. The models assume that there exists a region of the field of view (FOV) that is isoplanatic. Goodman (1968) explains that in an isoplanatic, or space-invariant, linear imaging system the image of a point-source will change location, but not functional form, as the point source moves. The approximately isoplanatic region of the FOV is modeled in FLIR92 and NVThermIP by a linear shift-invariant process and the MTF in that region is approximated by symmetrical blur. The blur is the result of real world effects on the image and can be due to aberrations and other manufacturing defects in the optical system. For a point source, the image is called a blur circle because diffraction, aberrations, manufacturing defects, and assembly tolerances prevent perfect resolution of the singularity (Driggers 1999). In FLIR92, the blur MTF is geometric and is discussed in further detail in the next chapter. The symmetrical blur approximation is not an accurate reflection of real world systems, so the blur approximation for the optics is not completely correct. Similarly, assuming symmetrical blurs does not accurately reflect the electronics used

in the various sensor systems under consideration: a low pass filter would not result in a time delay or phase shift using this assumption, for example (NVESD 2001).

NVThermIP provides some new capabilities beyond FLIR92. NVThermIP provides target acquisition performance predictions for staring imagers, not just the first and second generation thermal scanning sensors. In the NVThermIP calculation, the MTF representing the function of the human eye includes factors that are ignored in FLIR92. The MRTD prediction is changed from FLIR92; NVThermIP produces contrast transfer functions (CTFs) as the primary output. A laboratory MRTD is calculated, but is not comparable to the MRTD output from FLIR92. Also, NVThermIP now uses the Targeting Task Performance (TTP) metric to predict the probability of target detection, recognition, and identification at given ranges. FLIR92 uses the Johnson criteria, but does not predict probabilities of detection, recognition, or identification (NVESD 2001). In this report, the TTP capabilities in NVThermIP are neglected since only the MRTD results from FLIR92 are compared to those from NVThermIP.

### **3. Advantages and Disadvantages of FLIR92**

#### ***a. Advantages of FLIR92***

Since NVThermIP uses the same basic MRTD prediction theory with modifications to improve on FLIR92 (NVESD 2001), familiarity would be the primary benefit of continuing with FLIR92. These modifications are discussed in the next sections, regarding the advantages of NVThermIP. If FLIR92 operates at a sufficiently accurate and precise level to satisfy the increasingly more stringent requirements in operational use of TAWS, then there is no reason to change. Also, NVThermIP does not calculate a MDTD, which is more useful for indicating thermal imager performance for point sources and aperiodic targets. TAWS uses the MDTD for certain calculations, when available. For these two reasons, if a simple modification to FLIR92 to include optical turbulence improves the FLIR92 MRTD prediction, then it would be advantageous to continue using FLIR92.

***b. Disadvantages of FLIR92***

There are two major characteristics of FLIR92 that may lead to errors in performance predictions for staring arrays in sensors being modeled. Improved sensitivities in staring arrays mean that the limitations of the eye in detecting contrasts is now restricting the performance of these sensors (NVESD 2001), but FLIR92 MRTD calculations do not include any adjustments due to less-than-perfect contrast perceptions of the eye. Likewise, limitations on detector size, spacing, and fill factor (ratio of active cell area to total array area (Driggers 1999)) can cause under-sampled imagery for staring sensors. To avoid the under-sampled imagery, FLIR92 has an absolute cutoff at the half sample rates of imagers (Nyquist frequency), but when used with the Johnson criteria, it can lead to incorrectly negative predictions for most staring imagers (NVESD 2001). FLIR92 also does not account for atmospheric turbulence, which may be particularly significant in the highly turbulent regime just above a hot noon-time desert.

**4. Advantages and Disadvantages of NVThermIP**

***a. Advantages of NVThermIP***

NVThermIP is considered an advance over FLIR92 primarily because it addresses the two possible errors in FLIR92 performance predictions regarding staring arrays, as discussed above. NVThermIP also does include atmospheric turbulence in a fairly rudimentary form.

***b. Disadvantages of NVThermIP***

There are three major hesitations in switching to use NVThermIP with TAWS. First is a lack of familiarity. Otherwise, since NVThermIP was developed to address weaknesses in FLIR92, it should be advantageous to use. For instance, NVThermIP uses the Targeted Task Performance (TTP) Metric instead of the Johnson Metric to provide a better performance estimate. This result is then used, like with FLIR92, to predict the target acquisition range performance for given sensors. Second, while NVThermIP predicts the MRTD, it is a laboratory MRTD that is not

comparable to the MRTD from FLIR92. Instead, NVThermIP predicts the CTF (NVESD 2001), which must be manipulated before insertion into TAWS. Finally, NVThermIP does not produce an MDTT, but TAWS uses the MDTT for certain applications.

## **5. Phenomena Missing from FLIR92 and NVThermIP**

Despite improvements in NVThermIP, there are details missing from both FLIR92 and NVThermIP. One important lack is the optical turbulence. NVThermIP does include an average optical transmission input, but neither model considers the effect of optical turbulence variations along the optical path from the target to the sensor. The next section discusses this in more detail.

Neither FLIR92 nor NVThermIP have any adjustments for polarization of the target. Since the system response varies depending on the polarization, this lack will be especially apparent as imager sensitivities increase. Both models work best for nearly symmetric targets, but may poorly represent more realistic cases.

## **B. MOTIVATION TO TEST IMPORTANCE OF OPTICAL TURBULENCE**

Recently, sensors with higher resolution have been developed. These IR imagers are more sensitive to smaller targets, or a higher spatial frequency. In order to effectively model the responses of these sensors, it is becoming necessary to consider and perhaps include previously negligible effects like optical turbulence. At the sensitivities of the new sensors, the range for minimum detectability may be significantly affected by slight variations in the optical turbulence along the path from the target to the sensor, perhaps even as regards a vertical pathlength through the atmosphere. Optical turbulence causes blurring around the edges of images (Fante 1980) and makes it more difficult to resolve the image of the target well enough to identify it. According to the *IREO Handbook* Vol.3 (1993), the effects of pressure variations due to atmospheric turbulence are typically negligible compared to those



due to temperature and humidity fluctuations. In either very hot atmospheres such as those that may be operationally important in South Asia, or in very sensitive applications - such as detection of a very small target, the effect of atmospheric turbulence may become significant. Recent improvements in sensor responsivities have increased the number of operations in the sensitive applications category and therefore examining the potential impact of optical turbulence along the optical path through the atmosphere is crucial.

## C. PROJECT OVERVIEW

Two comparisons to test possible improvements to the MRTD calculation were accomplished.

First, a MatLab version of the operationally used FLIR92 was modified to include variations in optical turbulence along the pathlength. Then the original FLIR92 was compared to the modified FLIR92 to investigate the significance of improvements in the MRTD. Resultant MRTDs were inserted into TAWS and the maximum detection ranges were compared. The generic IR sensor in TAWS was used and marine and desert environments were tested.

Second, the MRTDs calculated by FLIR92 and by NVThermIP were compared. All input parameters were held constant for each model. The resultant MRTDs from FLIR92 and NVThermIP were entered into TAWS. The atmospheric conditions were varied to test the marine and desert environments. In TAWS, the generic IR sensor was used for all tests, modified to include the MRTD from either FLIR92 or NVThermIP.

### 1. Comparison Parameters

To compare FLIR92 and NVThermIP under the conditions described, parameters calculated by each were compared. Factors to compare and evaluate in order to determine the significance of any differences are the horizontal and vertical MRTDs and system MTFs at specified spatial frequencies. Again, the extrema of frequencies

are the regions of particular interest in this study. Because NVThermIP outputs the CTF, in order to compare, the resultant CTF was multiplied by 2 times the scene contrast temperature (SCT) to obtain the MRTD (Jon Hixson, personal communication).

The terms ‘horizontal’ and ‘vertical’ directions as used in this report refer to the along-bar and cross-bar directions of a four-bar target, as shown in Figure 1.

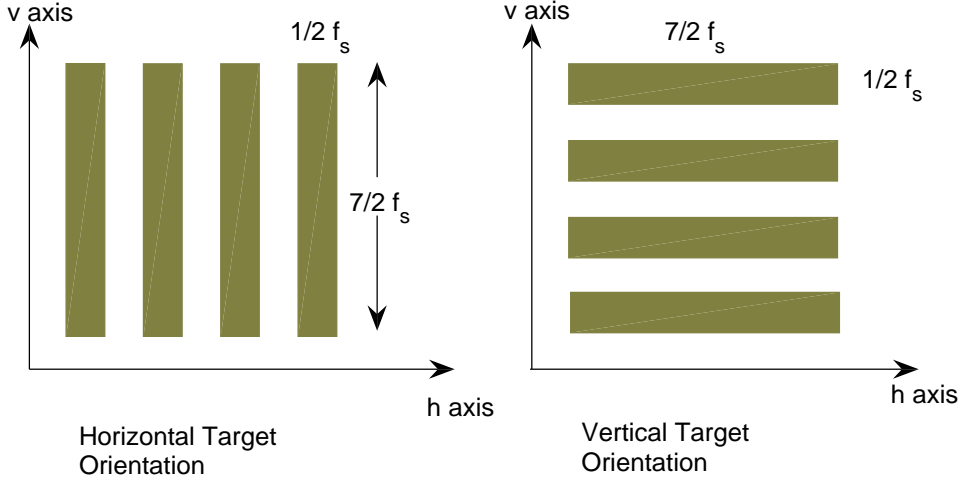


Figure 1. Horizontal and Vertical Directions with Respect to a 4-Bar Target.

## 2. Comparisons in TAWS

Once the MRTDs were determined from FLIR92 and NVThermIP, the results were entered into TAWS. Then, the range output from TAWS was compared for the various different iterations to determine how much and how significant the improvements to the maximum detection range in TAWS were.

## II. THERMAL IMAGING SYSTEMS PERFORMANCE MODELS

### A. FLIR92

#### 1. MTFs Included in FLIR92

FLIR92 uses a total system MTF to calculate the MRTD. The total system MTF is the product of the prefilter and postfilter MTFs, including the noise filter MTFs. For most component MTFs, FLIR92 can supply a model prediction, but allows for a user to directly input a measured or previously known MTF for the component. Generally, the measured MTFs improve performance estimates and are preferred over the MTFs predicted and calculated by FLIR92.

In FLIR92, the horizontal and vertical prefilter MTFs for a sensor are the products of the optical, detector spatial, focal plane array (FPA) integration, and image motion MTFs in the horizontal and vertical directions respectively. FLIR92 allows user-defined MTFs for all but the FPA integration MTF.

For scanned observing systems, filtering in the temporal domain must be translated into the spatial domain. The detector temporal MTF, electronics high and low frequency response MTFs, and boosting MTF are included in the temporal postfilter MTF that describes this translation. The temporal postfilter MTF in FLIR92 only applies for scanning systems and is only defined in the horizontal direction. FLIR92 allows a user-defined temporal postfilter MTF.

Both scanning and staring systems have spatial postfilters that model the system processing components. The spatial postfilter MTFs are the electro-optical multiplexer MTF, the digital filter MTF, the display MTF, the Charge-Coupled Device (CCD) charge transfer efficiency MTF, the display sample and hold MTF, and the eye MTF. All are defined in both the vertical and horizontal direction.

FLIR92 allows for an extra user-determined prefilter MTF and three extra postfilter MTFs to enable adequate description of the system. All the following

MTFs are standard in FLIR92 and are summarized from the *Analyst's Reference Guide* (1993) and compared against original sources or the *IREO Handbook* (1993) as specified. For scanning systems, the scan direction is assumed to be horizontal to the bars of the target.

**a. Optical MTF**

The optical MTF includes the diffraction-limited MTF and geometric blur MTF. When available, the optical MTF may be replaced by a user-defined version determined from direct measurements or ray tracing program predictions. The diffraction-limited MTF describes the resolution limitations due to diffraction in the optics of the sensor and is valid for a system with a circular, clear aperture (*IREO Handbook* Vol.4 1993). It is of the form

$$H_{dl}(f_s) = \frac{2}{\pi} \left( \arccos \left( \frac{\lambda f_s}{D_0} \right) - \frac{\lambda f_s}{D_0} \sqrt{1 - \left( \frac{\lambda f_s}{D_0} \right)^2} \right) \quad (2.1)$$

where  $\lambda$  is the wavelength for diffraction in  $\mu\text{m}$  and  $D_0$  is the optics aperture diameter in mm. Since  $\arccos(x)$  is only physical when  $-1 < x < 1$ , then the spatial frequency  $f_s$ , in cycles/mrad, must satisfy  $f_s \leq \frac{D_0}{\lambda}$ . The diffraction limited MTF in the horizontal direction is illustrated in Figure 2. For this report, the same inputs are used in the horizontal and vertical directions, so the MTF in the vertical direction is the same.

Apertures that are partially obscured or are not perfectly circular, or aberrations in the optics may cause blurring of the image (Goodman 1968). The optics MTF includes a geometric blur term to describe this phenomenon. If there is no user input for the geometric blur MTF, then FLIR92 assumes the blur is Gaussian and the MTF has the form

$$H_{gb}(f_s) = \exp(-2\pi^2 \sigma^2 f_s^2). \quad (2.2a)$$

$\sigma$ , in mrad, is the standard deviation for a circular Gaussian blur distribution. The *IREO Handbook* Vol.4 (1993) clarifies:  $\sigma^2$  is

$$\sigma^2 = \frac{w^2}{8} \quad (2.2b)$$

where  $w$  is the Gaussian blur spot diameter in mrad at the  $\frac{1}{e}$  point.

Figure 3 shows the geometric blur MTF in the horizontal direction. Again, with the inputs used in this report, the MTF is identical in the vertical direction.

***b. Detector Spatial MTF***

Also included in the prefilter MTF is the detector spatial MTF that compensates for the finite size of the detector. FLIR92 assumes a rectangular detector geometry. Like for the optical MTF, the *IREO Handbook* Vol.5 emphasizes the importance of a user-specified detector spatial MTF, particularly if the rectangular detector geometry approximation is grossly inaccurate.

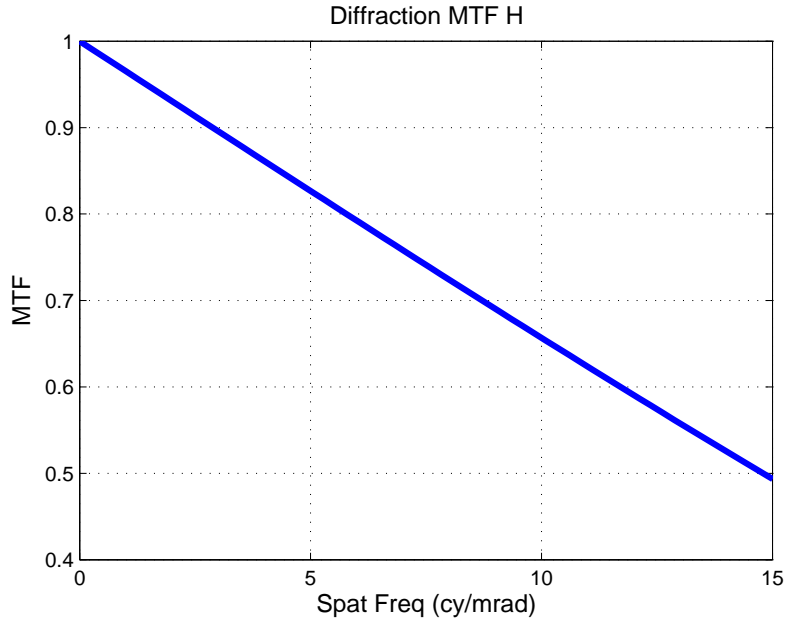


Figure 2. Diffraction Limited MTF in the Horizontal Direction.

A Signal Processing in the Element (SPRITE) system, incorporating the signal time delay and integration into one elongated detector element (*IREO Handbook* Vol.3 1993) has a horizontal detector spatial MTF of the form

$$H_{ds}(f_s) = \frac{\sin(\pi I_h f_s)}{\pi I_h f_s} \left( \frac{1}{1 + (2\pi Q f_s)^2} \right) \quad (2.3a)$$

where  $Q$  is the diffusion length and  $I_h$  is the instantaneous field of view (IFOV) of the readout length, both in mrad. The IFOV is the solid angle through which a detector is sensitive to radiation and in a scanning system. This is the subtended solid angle when all scanning motion stops. The vertical detector spatial MTF for SPRITE systems and both horizontal and vertical MTFs for non-SPRITE scanning and staring systems is

$$H_{ds}(f_s) = \frac{\sin(\pi \delta_z f_s)}{\pi \delta_z f_s} \quad (2.3b)$$

where  $\delta_z$  is the detector IFOV in mrad (Boreman 1990). The *IREO Handbook* Vol.4 (1993) also points out that this form is only valid when the point spread function of the detector is a rectangular function in direct space, but it is a reasonable approxi-

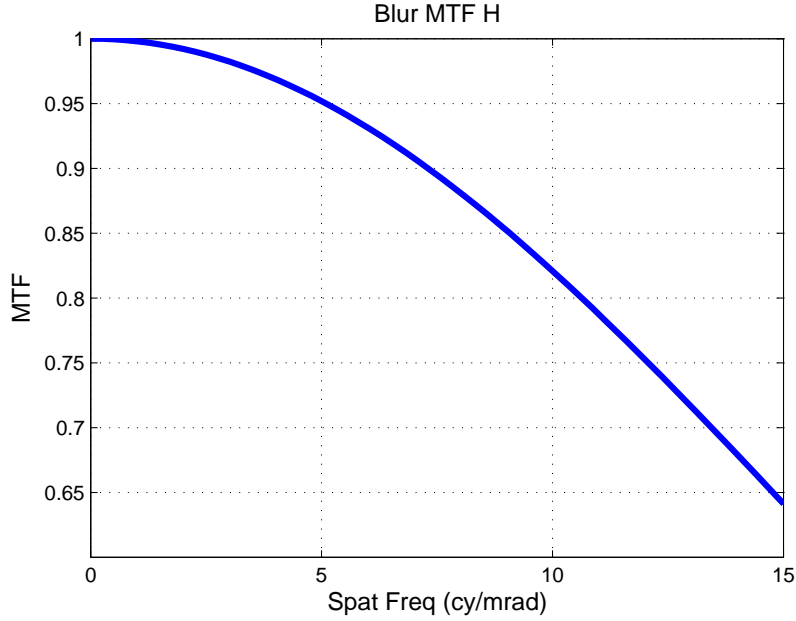


Figure 3. Geometric Blur MTF in the Horizontal Direction.

mation in most cases. The MatLab version of FLIR92 used in this analysis assumes a non-SPRITE system and uses Equation 2.3b. Figure 4 shows the form of the detector spatial MTF in the horizontal direction, and again it is identical in the vertical direction.

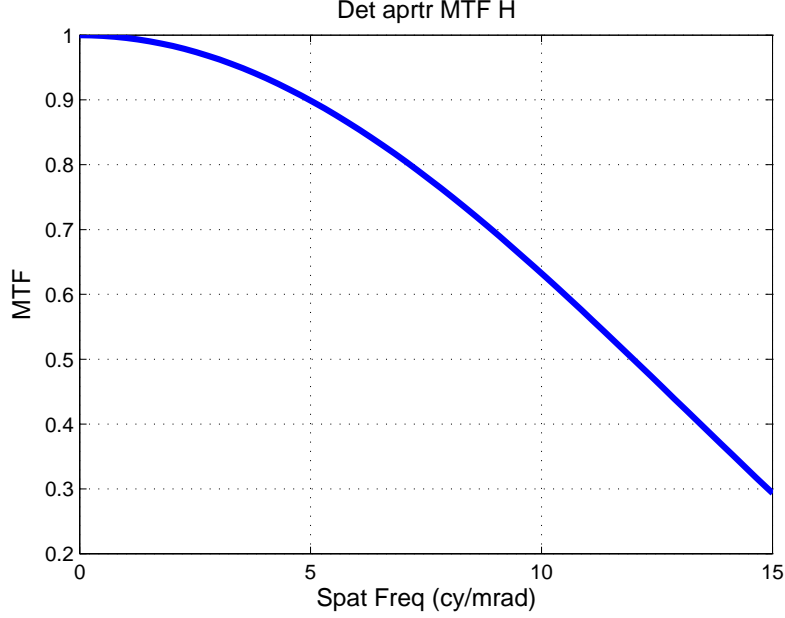


Figure 4. Detector Spatial MTF in the Horizontal Direction. This plot is assuming a non-SPRITE scanning or staring system.

### *c. Focal Plane Array Integration MTF*

For scanning systems, the prefilter MTF also includes a focal plane array integration MTF introduced in the horizontal direction by the finite integration time of the detector. If  $t_i$  is the detector integration time in s and  $v_s$  is the scan velocity in mrad/s, the MTF has the form of diffraction, or

$$H_{di}(f_s) = \frac{\sin(\pi f_s v_s t_i)}{\pi f_s v_s t_i}. \quad (2.4)$$

This MTF is only significant for scanning systems because staring systems do not require compensation for finite integration times since they do not move during detection.

**d. Sample-scene Phase MTF**

When considering sampled systems, the target location on the sampling grid can cause a phase effect, or aliasing effect. The aliasing of high frequency noise into the bandpass of the sampled signal can produce false signals or greatly increased noise or interference (*IREO Handbook* Vol.3 1993). The MTF representing this phase effect is

$$H_{ssp}(f_s) = \cos\left(\frac{f_s}{r_N}\Theta_z\right). \quad (2.5a)$$

Here,  $r_N$  is the Nyquist frequency in cycles/mrad and  $\Theta_z$  is the phase angle (rad) between the target under consideration and the detectors operating at  $r_N$ . The Nyquist frequency, or Nyquist limit, is the frequency at which no useful information is transmitted and is taken as half the scene sample frequency. It is given as

$$r_N = \frac{s_z}{2\delta_z} \quad (2.5b)$$

where  $s_z$  is the number of samples per detector IFOV. Input frequencies above the Nyquist limit are likely to appear as aliasing signals at the lower frequencies (*IREO Handbook*). At optimal operation,  $\Theta_z$  is set equal to 0, but for average conditions  $\Theta_z$  is set equal to 0.785 rad (45°). In the inputs used for the MatLab version of FLIR92,  $\Theta_z$  is set to 0, or for optimal operation. This results in an MTF in the horizontal and the vertical direction that is constant at unity for all frequencies since  $\cos(0)$  is unity.

**e. Image Motion MTF**

Image motion MTFs are included in FLIR92 to account for how the thermal system moves with respect to the scene being imaged. Two causes of these movements may be linear motion of the sensor system or vibration of the sensor platform. These movements are represented in the linear image motion MTF, random image motion MTF, and sinusoidal image motion MTF.

The linear motion MTF explains smearing of the scene across the detectors due to movement of the system platform. How significant the smear is depends on how fast the platform is moving and how long the detectors are exposed to the



scene during platform movement. Given  $v_r$  is the relative image velocity in mrad/s, the linear image motion MTF may be described by

$$H_{ml}(f_s) = \frac{\sin(\pi v_r t_i f_s)}{\pi v_r t_i f_s}. \quad (2.6)$$

When  $t_i$  is not specified, the integration time defaults to the field time. Typically, the linear image motion is only significant for staring systems because scanning systems expect the sensor to be moving, or scanning, during detection. The MatLab version of FLIR92 sets this MTF to unity for all frequencies.

For simplicity, the random image motion is assumed to be Gaussian. The *IREO Handbook* Vol.4 (1993) notes that this Gaussian term includes the random vibration of the sensor with respect to the scene, uncertainty in the sensor position, and other causes of image jitter. The associated MTF is

$$H_{mr}(f_s) = \exp(-2\pi^2 \sigma_{LOS}^2 f_s^2) \quad (2.7)$$

where  $\sigma_{LOS}^2$  is the standard deviation of the total random vibration from all sources, in mrad. Figure 5 illustrates the form of the random motion MTF in the horizontal direction. The vertical direction is identical with the given inputs.

Finally, the sinusoidal vibration of the platform may be described by a zero-order Bessel function, as shown in the *IREO Handbook* Vol.5 (1993),

$$H_{ms}(f_s) = J_0(2\pi A f_s). \quad (2.8)$$

$A$  is the amplitude of the assumed sinusoidal vibration in mrad. The zero-order Bessel function has the form shown in Fig 6, similar to a damped cosine function. Using the given inputs, though,  $A$  is set to zero and  $H_{ms}$  is thus held constant at unity for all frequencies since  $J_0(0) = 1$ .

### ***f. Detector Temporal MTF***

Because the detector has a finite response time, the system has a low-pass temporal filter given by

$$H_{dt}(f_t) = \left[ 1 + \left( \frac{f_t}{f_{dt}} \right)^2 \right]^{-\frac{1}{2}} \quad (2.9)$$

where  $f_t$  is the temporal frequency in Hz and is related to the spatial frequency by the scan velocity since  $f_t = f_s v_s$ .  $f_{dt}$  is the 3dB frequency in Hz of the detector temporal response. The *IREO Handbook* Vol.4 further elaborates on Equation 2.9 - the finite temporal response to radiation incident on the detectors causes blurring in the scanning direction, which is why  $H_{dt}$  is included in the horizontal for scanning systems.

***g. Electronics Frequency Responses***

The frequency responses for systems that are AC-coupled are given by multiple pole RC filters. The *IREO Handbook* (1993) gives the single-RC low-pass and high-pass filter MTFs, which are then raised to the  $n$ th power, where  $n$  is the number of filter poles, to arrive at Equations 2.10a and 2.10b.

For the low frequency response, the high pass filter MTF is

$$H_{ehp}(f_t) = \frac{\left(\frac{f_t}{f_{ehp}}\right)^n}{\sqrt{1 + \left(\frac{f_t}{f_{ehp}}\right)^{2n}}} \quad (2.10a)$$

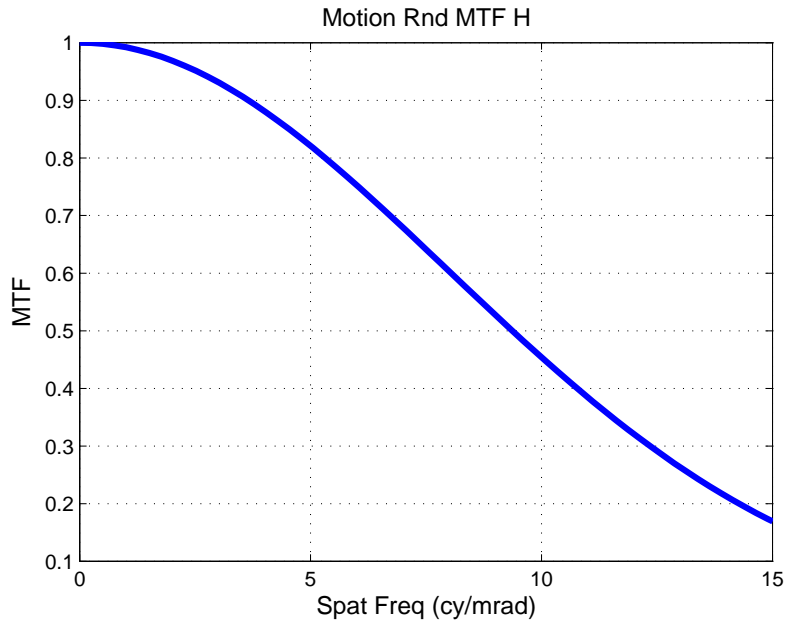


Figure 5. Random Motion MTF in the Horizontal Direction.

where  $f_{ehp}$  is the electronics 3dB frequency in Hz. The low frequency response is only significant at extremely low frequencies, so FLIR92 does not include it in the total MTF, but  $H_{ehp}$  is used to calculate noise bandwidths.

For the high frequency response, the low pass filter MTF is

$$H_{elp}(f_t) = \left(1 + \left[\frac{f_t}{f_{elp}}\right]^{2n}\right)^{-\frac{1}{2}} \quad (2.10b)$$

where like in the high pass filter case,  $f_{elp}$  is the 3dB frequency in Hz and  $n$  is the number of filter poles. This high frequency response MTF is included in the total MTF since the high frequency response is significant at a greater range of frequencies.

#### ***h. Boosting MTF***

For the scanning system, an aperture correction MTF, or electronic boosting MTF, is required. The boost emphasizes higher frequencies to compensate for the reduced depth of modulation that typically occurs at higher frequencies due to the less-than-ideal aperture response (*IREO Handbook* Vol.4 1993). It has the form

$$H_{eb}(f_t) = 1 + \frac{1}{2}(B_a - 1) \left[1 - \cos\left(\frac{\pi f_t}{f_b}\right)\right]. \quad (2.11)$$

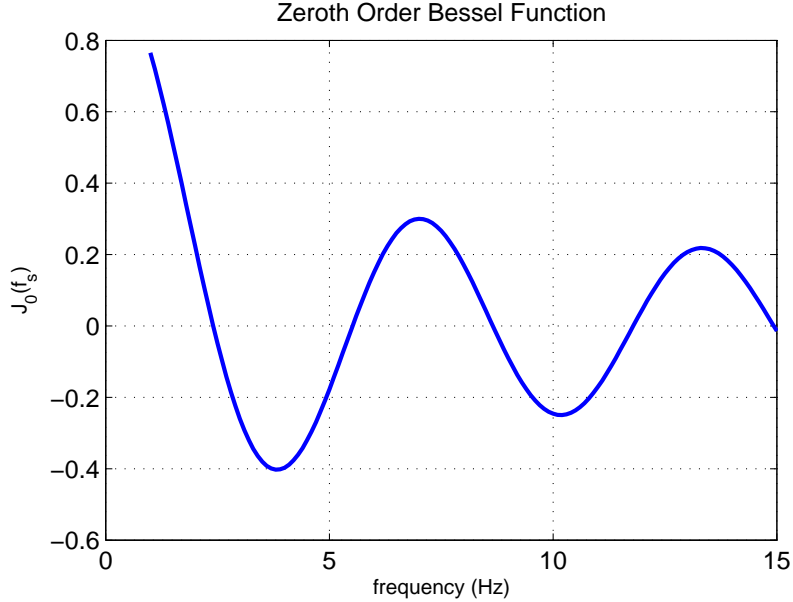


Figure 6. Zeroth Order Bessel Function

$f_b$  is the frequency in Hz of the maximum boost and  $B_a$  is the amplitude of the boost at a maximum frequency  $f_{max}$ . As the *IREO Handbook* Vol.4 observes, the boost MTF is applied along the scan direction.

***i. Electro-Optical Multiplexer MTF***

For the LED electro-optical multiplexer, the MTF is of the form of diffraction,

$$H_{eom}(f_s) = \frac{\sin(\pi f_s \delta_{LED})}{\pi f_s \delta_{LED}} \quad (2.12)$$

and  $\delta_{LED}$  is the angular subtense of the LED element in mrad.  $H_{eom}$  is not included in the MatLab version of FLIR92.

***j. Digital Filter MTF***

Digital filters have a linear phase symmetrical impulse response which varies depending on whether there is an even or an odd number of samples ( $N$ ). For  $N$  odd,

$$H_{df}(f_s)_{odd} = \sum_{i=0}^{(N-1)/2} a_i \cos \left[ \frac{2\pi i f_s}{f_{co}} \right]. \quad (2.13a)$$

For  $N$  even,

$$H_{df}(f_s)_{even} = \sum_{i=1}^{N/2} a_i \cos \left[ \frac{2\pi \left(i - \frac{1}{2}\right) f_s}{f_{co}} \right]. \quad (2.13b)$$

For these MTFs,  $a_i$  is the digital filter coefficient and  $f_{co}$  is the filter cut off frequency in cycles/mrad. In the MatLab FLIR92, this MTF is set to unity for all frequencies in both the horizontal and vertical directions.

***k. Display MTF***

Although many recent thermal imagers use a cathode ray tube (CRT) display to communicate collected information to the observer, if a non-CRT display is being used, FLIR92 requires a user-specified MTF. Otherwise, the model calculates the total MTF based on a CRT display. In FLIR92, the phosphor spot luminance intensity is assumed to have a Gaussian distribution with a  $\sigma$  value either specified by the user or calculated by the model from the relationship

$$\sigma = \sqrt{-\frac{\log(0.025)}{2\pi^2 f_{Nr}^2}} \quad (2.14)$$

with the raster frequency,  $f_{N_r}$  in lines/mrad,

$$f_{N_r} = \frac{N_r}{\beta}. \quad (2.15)$$

Here the model uses the TV limiting resolution criterion that the MTF equal 0.025 at the raster frequency.  $N_r$  is the number of lines on the CRT that are active.  $\beta$  is the vertical FOV in mrad. Using these quantities, the display MTF may be expressed as

$$H_{CRT}(f_s) = \exp\left(-2\pi^2\sigma^2 f_s^2\right). \quad (2.16)$$

Since this result is only valid for the specified resolution criteria, modifications for other resolution criteria may be made by multiplying a calculated  $\sigma$  by an appropriate conversion factor and then entering the result directly into the model. The *IREO Handbook* Vol.5 (1993) again points out that  $\sigma$  follows Equation 2.2b. In the FLIR92 MatLab version used in this report,  $\sigma$  was hard coded to 0.01 mrad, with the resultant MTF shown in Figure 7.

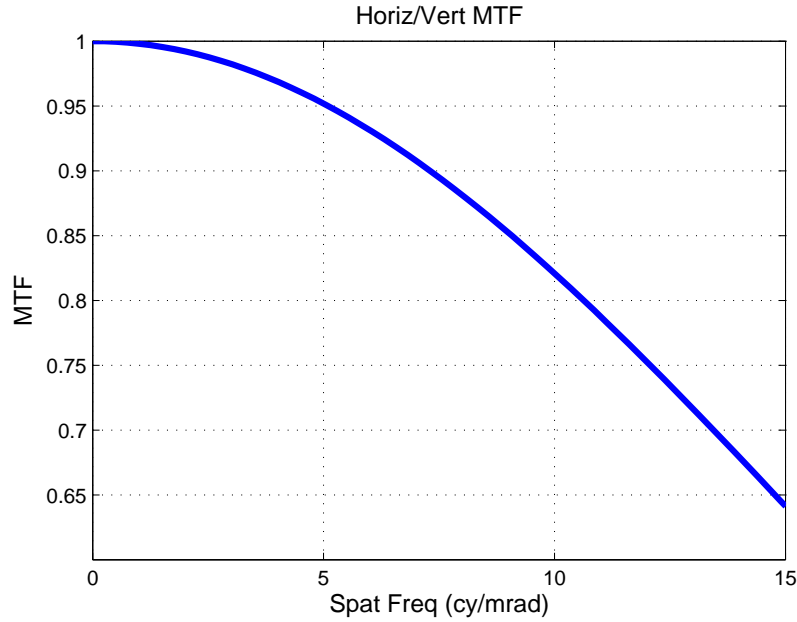


Figure 7. Display MTF.

The standard deviation of the Gaussian distribution is set to 0.01 mrad.

***l. CCD Charge Transfer Efficiency MTF***

For a CCD system, Sequin and Thompsett (1975) explained the charge transfer efficiency MTF as due to the non-unity charge transfer efficiency of the system. The CCD charge transfer efficiency MTF depends on the number of gates in the transfer from the detector to the output amplifier ( $N$ ) and the charge transfer efficiency at each gate ( $\epsilon$ ) along with the Nyquist frequency, or the sampling frequency of the structure. As indicated in the *IREO Handbook* Vol.4, it may be expressed as

$$H_{CCD}(f_s) = \exp\left(-N(1 - \epsilon) \left[1 - \cos\left(\frac{2\pi f_s}{r_N}\right)\right]\right) \quad (2.17)$$

where  $r_N$  is again the Nyquist frequency in cycles/mrad (see Section II.A.1.d).  $N$  may be calculated in the model by assuming that the system has a interline transfer scheme, but often is specified by the user. In the MatLab program being used, the CCD Charge Transfer Efficiency MTF was set to unity for all frequencies, in both the vertical and horizontal directions.

***m. Display Sample and Hold MTF***

Given that  $\delta_s$  is the sampling aperture in mrad, the display sample and hold MTF has the form

$$H_{dsh}(f_s) = \frac{\sin(\pi\delta_s f_s)}{\pi\delta_s f_s}. \quad (2.18)$$

Figure 8 shows the horizontal display sample and hold MTF, but the vertical is set in the MatLab code to be unity for all frequencies.

***n. Eye MTF***

The eye MTF encapsulates the influences of the observer. In FLIR92, the eye MTF is based on work by Kornfeld and Lawson (1971). The observer may be able to improve and optimize the system display by adjusting the gain and level, the viewing distance, and the like. In this case, the eye MTF is considered non-limiting and is considered a constant of unity since no degradation of the spatial frequency response would be expected. In other words,

$$H_{eye}(f_s) = 1.0. \quad (2.19a)$$

On the other hand, the observer may not be able to improve or adjust the display to peak performance. If this is the case, the eye limits the clarity of the image, so there is a degradation in the spatial frequency response. The MTF to describe this degradation, the limiting eye MTF, is of exponential form,

$$H_{eye}(f_s) = \exp\left(-\frac{\Gamma f_s}{2M}\right). \quad (2.19b)$$

Here,  $M$  is the system magnification and  $\Gamma$  is the spread function width of the eye in mrad.  $\Gamma$  depends on the ambient light level (Kornfeld and Lawson 1971). Since the observer is often preoccupied or unable to adjust the display, FLIR92 defaults to the limiting eye MTF. In the MatLab code,  $\Gamma$  is hard coded to 2.196 mrad. The resultant MTF is shown in Figure 9.

***o. System Noise Filter MTF***

The system noise filter MTF includes only the detector noise and is composed of all the noise filter MTFs. These MTFs -  $H_{dt}$ ,  $H_{ehp}$ , roll up of the temporal postfilter MTF ( $H_{TPF}$ ), and the spatial postfilter roll up ( $H_{SPF}$ ) are discussed above.

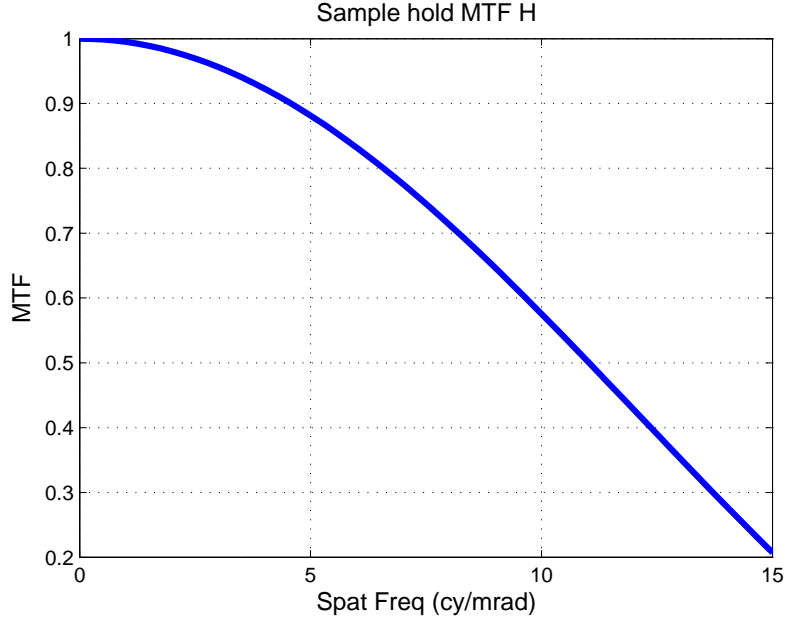


Figure 8. Display Sample and Hold MTF in the Horizontal Direction.

The system noise filter MTF is not included in the total system MTF ( $H_{SYS}$ ) since the component MTFs are already included in the total MTF, but will be referenced in future sections. It may be expressed as

$$H_{NF}(f_s) = H_{di}(f_s)H_{ehp}(f_s)H_{TPF}(f_s)H_{SPF}(f_s) \quad (2.20)$$

where for staring systems,  $H_{TPF}(f_s)$  is unity. The horizontal system noise MTF is shown in Figure 10.

***p. Total System MTF***

The total system MTF is the product of all the component MTFs described above. For the generic case described in this report, the total horizontal MTF is shown in Figure 11. The downward curve of the MTF illustrates how much the image is degraded, particularly at higher spatial frequencies, corresponding to small targets.

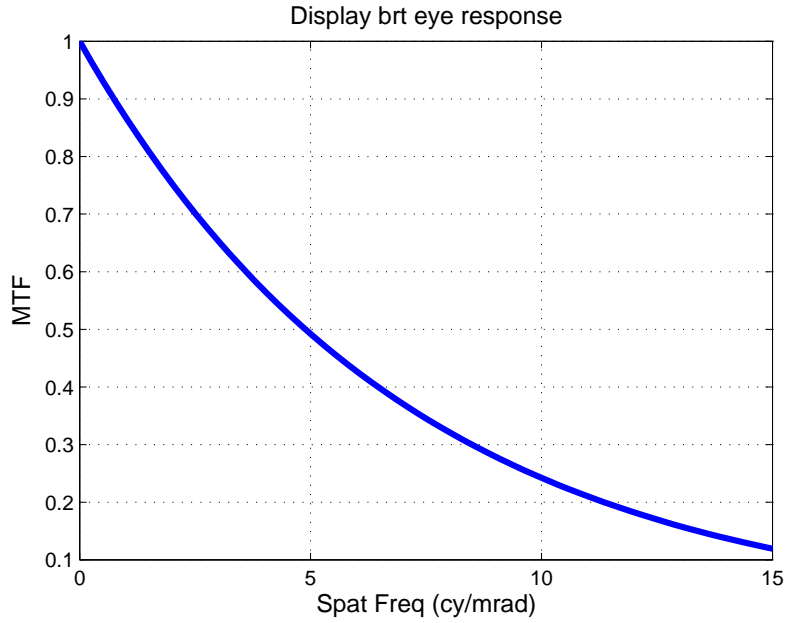


Figure 9. Eye/Brain Response MTF.



## 2. Sampling

### *a. Limits to Defined MRTD*

In FLIR92, the MRTD is only defined for a periodic target such as a 4-bar target. The target must have a 7:1 aspect ratio, as shown in Figure 1 and the four bars should be fully resolved by the observer in order to specify an MRTD. In thermal imagers, the cutoff frequency for the observer to be able to fully resolve the target is the system's Nyquist frequency. By definition, then, no MRTD can be given. This limits FLIR92 to MRTD prediction below the Nyquist limit.

Since many targets are aperiodic, this artificial method of limiting the MRTD prediction may be pessimistic. Information relating to the MRTD may be available above the Nyquist limit, but methods for obtaining and quantifying this information are not available for use in FLIR92.

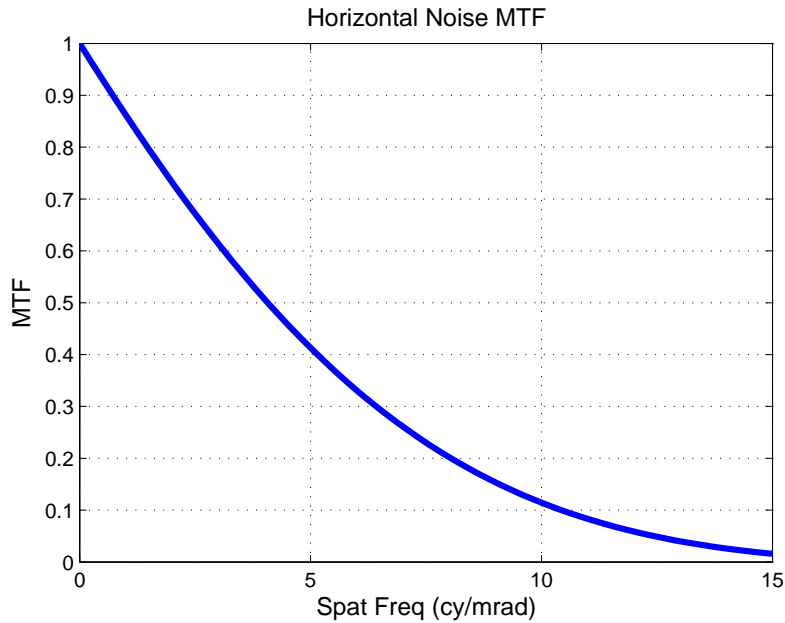


Figure 10. Horizontal System Noise MTF.

***b. Sampling Rate and Lattice Spacing***

The *IREO Handbook* Vol.4 (1993) explains that imagers sample spatially and temporally. Spatially, the thermal imagers sample at a rate of

$$R_z = \frac{s_z}{\delta_z}. \quad (2.21)$$

This is half the Nyquist frequency, as can be seen by comparing Equations 2.5b and 2.21. The sample lattice spacing is then the inverse of Equation 2.21,  $\frac{1}{R_z}$ . FLIR92 actually calculates the effective sampling rate and effective lattice spacing by multiplying together the horizontal and vertical components ( $z = h$  and  $z = v$ ) and then taking the square root.

***c. Optimizing Scene Phasing***

As discussed in Section II.A.1.d, the MRTD measurement may be degraded by phasing between the target and the detector grid. There is an MTF included to account for this phase difference, particularly when dealing with staring

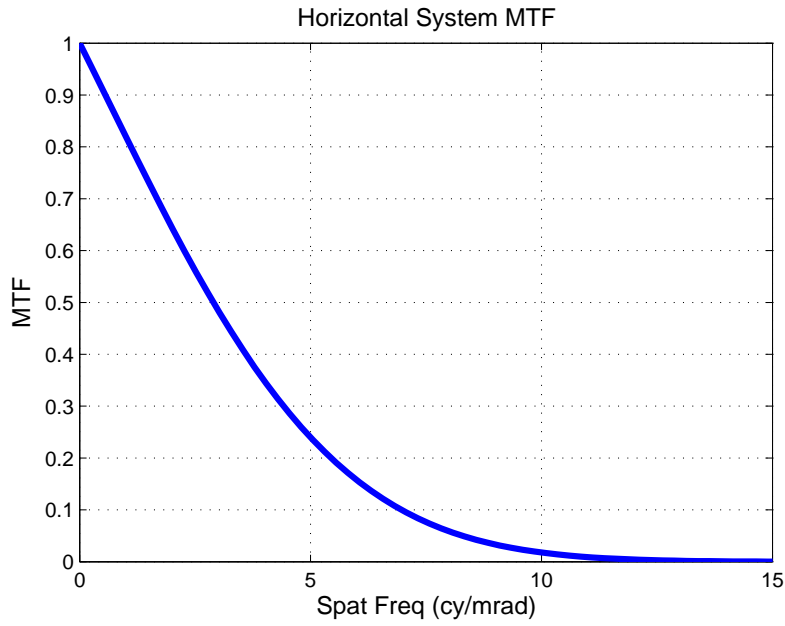


Figure 11. Horizontal System MTF.

systems where the MRTD degradation is pronounced when there is a misalignment between respective targets and detectors under consideration.

### 3. System Noise

FLIR92 characterizes second-generation thermal imaging systems and as such, the system noise in MRTD predictions is modeled using a scaling factor that multiplies the random spatio-temporal noise by the amount of excess system noise (Kennedy 1990). To simplify the model, the system noise is reduced to components that add in quadrature. Appropriate eye spatial and temporal integration effects are considered for each noise component included.

The Night Vision and Electronic Sensors Directorate (NVESD) of the US Army in 1990 established a theoretical framework and a standard laboratory measurement procedure to better characterize the noise in the system (Webb et.al. 1991). This method of noise analysis isolates the system noise into eight components. These components are listed in Table I along with possible sources of the noise.

Table I. 3-D Noise Component Descriptions in FLIR92

Subscripts of noise components shown in table indicate dimension:  $t$  temporal,  $v$  vertical spatial,  $h$  horizontal. Table derived from *Analyst's Reference Guide* (1993).

<i>Noise</i>	<i>Description</i>	<i>Potential Source</i>
$\sigma_{tvh}$	random spatio-temporal noise	basic detector temporal noise
$\sigma_{tv}$	temporal row noise	line processing, $\frac{1}{f}$ , read-out
$\sigma_{th}$	temporal column noise	scan effects
$\sigma_{vh}$	random spatial noise	pixel processing, detector-to-detector non-uniformity
$\sigma_v$	fixed row noise	detector-to-detector non-uniformity, $\frac{1}{f}$
$\sigma_h$	fixed column noise	scan effects, detector-to-detector non-uniformity
$\sigma_t$	frame-to-frame noise	frame processing
$S$	mean of all components	

Here,  $\sigma_{tvh}$  is the basic detector noise which is often characterized by the NETD (see Equation 2.22, next section). The NETD is a sensitivity parameter. It is defined as the temperature difference between the target and the background that will produce

a peak signal to rms noise ratio of unity at the output of a reference filter. This is how the NETD gives a rough estimate of how noisy a sensor is compared to the signals being detected. All other components besides  $\sigma_{tvh}$  must be added in quadrature in order to completely characterize the thermal imaging systems noise (Scott et. al. 1993). In the current operational FLIR92,  $\sigma_{tvh}$  is predicted but the remaining components are measured or estimated. FLIR92 includes estimates of 3-D noise for generic scanning and staring sensors so that when measurements are not available, a calculation may still be made. More detailed descriptions of the system noise are given in the sections following.

*a. Defaults for 3-D Noise Components*

In a given system where 3-D noise measurements have not yet been made or are not available, FLIR92 provides a set of default values. These default values are only given for what FLIR92 considers significant noise components and depend on the predicted random spatial-temporal noise,  $\sigma_{tvh}$ . As discussed in Section II.A.3, the system noise sources add in quadrature, so only the most significant noise components are defaulted to non-zero components since the others would scarcely affect the outcome of the noise calculation. These default values are from a database of system noise measurements that were carried out by NVESD starting in April 1990. The values for each system in the database are normalized to  $\sigma_{tvh}$  and averaged with other systems in the same class in order to determine which are the dominant noise sources in that class and which are so small they may be neglected.

In scanning systems, the significant noise components are the temporal row and the fixed row noises,  $\sigma_{tv}$  and  $\sigma_v$ . Scanning systems typically show a wide range of variation in noise levels, so three default values are provided for both  $\sigma_{tv}$  and  $\sigma_v$ . Table II shows the model's default values for scanning systems.

In staring systems, the significant noise component is the random spatial noise,  $\sigma_{vh}$ . NVESD found a single default value for  $\sigma_{vh}$  to be sufficiently representative. This default value is shown in Table III.

Table II. 3-D Noise Components For Scanning Systems

Subscripts of noise components shown in table indicate dimension:  $t$  temporal,  $v$  vertical spatial,  $h$  horizontal. Table derived from the *Analyst's Reference Guide* (1993).

Noise Term	Low Noise Default	Moderate Noise Default	High Noise Default
$\sigma_{tv}$	$0.25\sigma_{tvh}$	$0.75\sigma_{tvh}$	$1.0\sigma_{tvh}$
$\sigma_v$	$0.25\sigma_{tvh}$	$0.75\sigma_{tvh}$	$1.0\sigma_{tvh}$

Table III. 3-D Noise Component For Staring Systems

Subscripts of noise components shown in table indicate dimension:  $t$  temporal,  $v$  vertical spatial,  $h$  horizontal. Table derived from the *Analyst's Reference Guide* (1993).

Noise Term	Noise Default
$\sigma_{vh}$	$0.40\sigma_{tvh}$

**b. Random Spatio-temporal Noise,  $\sigma_{tvh}$**

Since  $\sigma_{tvh}$  is related to the actual bandwidth of the system, it may be measured directly at the output port prior to display. However, as outlined in the *IREE Handbook* Vol.4, it may otherwise be determined through the relationship to the NETD,

$$\sigma_{tvh} = NETD \times \sqrt{\frac{\Delta f_p}{\Delta f_N}} \quad (2.22)$$

where  $\Delta f_N$  is the equivalent noise bandwidth for the NETD. In this case,  $\Delta f_p$  is the actual noise bandwidth which is associated with the system electronics before display. In order to determine the equivalent noise bandwidth, given that  $S(\nu)$  is the normalized detector noise power spectrum and  $H_{ref}(\nu)$  is the standard NETD reference filter, the relationship used is

$$\Delta f_N = \int_0^{\infty} S(\nu)[H_{ref}(\nu)]^2 d\nu. \quad (2.23)$$

The actual noise bandwidth differs depending on whether a scanning or staring system is under consideration. When considering scanning systems, the noise bandwidth at the system output port is of similar form to the equivalent noise bandwidth,

$$\Delta f_p = \int_0^{\infty} S(\nu)[H_{TPF}(\nu)]^2 d\nu. \quad (2.24)$$

For staring systems, the actual noise bandwidth is given by

$$\Delta f_p = \int_0^\infty S(\nu) \left( \frac{\sin(\pi \nu t_i)}{\pi \nu t_i} \right)^2 d\nu \quad (2.25)$$

and  $t_i$  is the FPA integration time.

For all classes of systems, staring or scanning, the general form of the random spatio-temporal noise is given in Equation 2.26,

$$\sigma_{tvh} = \frac{4f_{no}^2 \sqrt{\Delta f_p}}{\pi \tau_0 \sqrt{A_d} \int_{\lambda_1}^{\lambda_2} D^*(\lambda, 300) \frac{\partial W}{\partial T_{300}}(\lambda) d\lambda}. \quad (2.26)$$

Here,  $f_{no}$  is the optical f-number,  $\Delta f_p$  is the system noise bandwidth as defined in Equation 2.24 or 2.25,  $\tau_0$  is the optical transmittance, and  $A_d$  is the detector area in  $\text{cm}^2$ . The partial derivative is the thermal derivative of Planck's Law in  $\text{W}/\text{cm}^2/\text{sr}/\mu\text{m}$ . The detector noise-limited spectral detectivity is  $D^*(\lambda, 300)$  in  $\text{cm-Hz}^{\frac{1}{2}}/\text{W}$  and includes only noise components from the temporal noise sources since the spatial noise source contributions are included in the system noise correction functions described in the following section, II.A.3.c. Also, FLIR92 does not make any adjustments for changes to detector responsivity due to cold shielding, so any tweaking there must be off-line.

### ***c. Noise Correction Functions***

Since each 3-D noise component listed in Table I is assumed to be statistically independent, the total system noise, filtered, may be written as the root sum square of the noise components:

$$\begin{aligned} \Omega(f_s) &= \sigma_{tvh}^2 E_t E_{v_z}(f_s) E_{h_z}(f_s) + \sigma_{vh}^2 E_{v_z}(f_s) E_{h_z}(f_s) \\ &+ \sigma_{th}^2 E_t E_{h_z}(f_s) + \sigma_{tv}^2 E_t E_{v_z}(f_s) + \sigma_v^2 E_{v_z}(f_s) \\ &+ \sigma_h^2 E_{h_z}(f_s). \end{aligned} \quad (2.27)$$

Here,  $E_t$ ,  $E_{h_z}(f_s)$  and  $E_{v_z}(f_s)$  represent the eye or brain temporal and spatial integration associated with the noise components. The frame-to-frame term  $\sigma_t^2 E_t$  has been

dropped because the frame-to-frame noise  $\sigma_t$  is almost always so small comparatively that it is negligible. The orientation of the MRTD target under consideration is indicated by the subscript  $z$ . In this case, the temporal integration may be expressed in terms of  $F_R$ , the system frame rate in Hz,  $\tau_E$ , the eye integration time in sec, and  $\alpha_t$ , the temporal sample correlation length.

$$E_t = \frac{\alpha_t}{F_R \tau_E}. \quad (2.28)$$

In FLIR92,  $\alpha_t$  is assumed to be unity in MRTD calculations. The spatial integrations are simplified in the FLIR92 model and may be expressed in terms of sample correlation factors  $\alpha_h$  and  $\alpha_v$ , horizontal and vertical sampling rates  $R_h$  and  $R_v$  in samples/mrad, and spatial integration limits  $L_{hz}(f_s)$  and  $L_{vz}(f_s)$  in mrad<sup>-1</sup>. These spatial integration limits are approximately the width and height of the MRTD bar target. For staring systems, the samples in each direction are assumed independent so that  $\alpha_h$  and  $\alpha_v$  are unity. For scanning systems, samples in the scan direction may not be assumed independent due to the motion of the scanner, so  $\alpha_h$  may be greater than unity. Similarly, samples taken perpendicular to the scan direction may be assumed independent since the motion of the scanner is cross-directional, so  $\alpha_v$  is unity. Although FLIR92 uses this simplified form, the exact expressions for the horizontal and vertical eye/brain spatial integration are given in Appendix B.

In order to determine the noise terms for the horizontal and vertical MRTD calculations, it is assumed that only noise components in the direction of the MRTD target degrade the MRTD. For the MDT, since target orientation does not affect the calculation, the noise correction function is independent of direction. Given the noise correction functions in the horizontal,

$$k_h(f_s) = \sqrt{1 + \frac{\sigma_{vh}^2}{\sigma_{tvh}^2} E_t^{-1} + \frac{\sigma_{th}^2}{\sigma_{tvh}^2} [E_{vh}(f_s)]^{-1} + \frac{\sigma_h^2}{\sigma_{tvh}^2} [E_t E_{vh}(f_s)]^{-1}} \quad (2.29)$$

and in the vertical,

$$k_v(f_s) = \sqrt{1 + \frac{\sigma_{vh}^2}{\sigma_{tvh}^2} E_t^{-1} + \frac{\sigma_{tv}^2}{\sigma_{tvh}^2} [E_{hv}(f_s)]^{-1} + \frac{\sigma_v^2}{\sigma_{tvh}^2} [E_t E_{hv}(f_s)]^{-1}} \quad (2.30)$$

the horizontal and vertical MRTD noise terms may be expressed. In the horizontal direction, the noise term is given as

$$\omega_h(f_s) = \sigma_{tvh} k_h(f_s) \sqrt{E_t E_{v_h}(f_s) E_{h_h}(f_s)} \quad (2.31)$$

and in the vertical,

$$\omega_v(f_s) = \sigma_{tvh} k_v(f_s) \sqrt{E_t E_{v_v}(f_s) E_{h_v}(f_s)}. \quad (2.32)$$

For the MDTD, the noise correction function has the form

$$\begin{aligned} k_{MDT}(f_s) = & \left( 1 + \frac{\sigma_{vh}^2}{\sigma_{tvh}^2} E_t^{-1} + \frac{\sigma_{th}^2}{\sigma_{tvh}^2} [E_v(f_s)]^{-1} + \frac{\sigma_h^2}{\sigma_{tvh}^2} [E_t E_v(f_s)]^{-1} \right. \\ & \left. + \frac{\sigma_{tv}^2}{\sigma_{tvh}^2} [E_h(f_s)]^{-1} + \frac{\sigma_v^2}{\sigma_{tvh}^2} [E_t E_h(f_s)]^{-1} \right)^{\frac{1}{2}}. \end{aligned} \quad (2.33)$$

#### 4. Calculating the Predicted MRTD

The basic form for the MRTD calculated in FLIR92 is of the form

$$MRTD_z(f_s) = \frac{\frac{\pi^2}{8} SNR_{TH} \sigma_{tvh} k_z(f_s)}{H_{SYS_z}(f_s)} \sqrt{E_t E_{h_z}(f_s) E_{v_z}(f_s)} \quad (2.34)$$

where  $z$  again indicates the orientation of the MRTD target in either the horizontal or the vertical direction. The denominator  $H_{SYS_z}(f_s)$  is the total system MTF, or the product of all component MTFs.  $k_z(f_s)$  is the 3-D noise correction function, as given in Equations 2.29 and 2.30. The threshold SNR required to resolve the MRTD target is  $SNR_{TH}$  and the eye/brain integrals are as described in Section II.A.c and Appendix B. The *IREO Handbook* Vol.5 further outlines this method of determining the predicted MRTD. More details about the included variables in this general form of the MRTD calculation are given below. The system MRTD for the given input parameters is shown in Figure 12.

##### ***a. Psychophysical Constants $SNR_{TH}$ and $\tau_E$***

In FLIR92, the threshold SNR to resolve the MRTD target and the eye integration time,  $SNR_{TH}$  and  $\tau_E$ , may be adjusted to tweak an MRTD prediction to better match a set of measurements. NVESD does have recommended settings, as



given in Table IV. Biberman (1973) showed using psychophysical data that  $SNR_{TH}$  is a function of the target spatial frequency, but the NVESD recommended value of 2.5 is a representative average for optimal observing conditions.

Table IV. NVESD Recommended Settings for Psychophysical Constants  
Settings in FLIR92 may be adjusted from NVESD recommendations.

<i>Psychophysical Constant</i>	<i>NVESD Recommended Setting</i>	<i>Units</i>
$SNR_{TH}$	2.5	—
$\tau_E$	0.1	s

$\tau_E$  depends on the background luminance. Luminances corresponding to a 0.1 s eye integration time show agreement with display luminances that NVESD measured in perception experiments in 1988. These experiments were conducted under conditions similar to those used in MRTD measurements such as a darkened room and optimal viewing. Observers set the display luminance to an average of 0.15 milli-Lamberts. Higher ambient light conditions typically correspond to greater

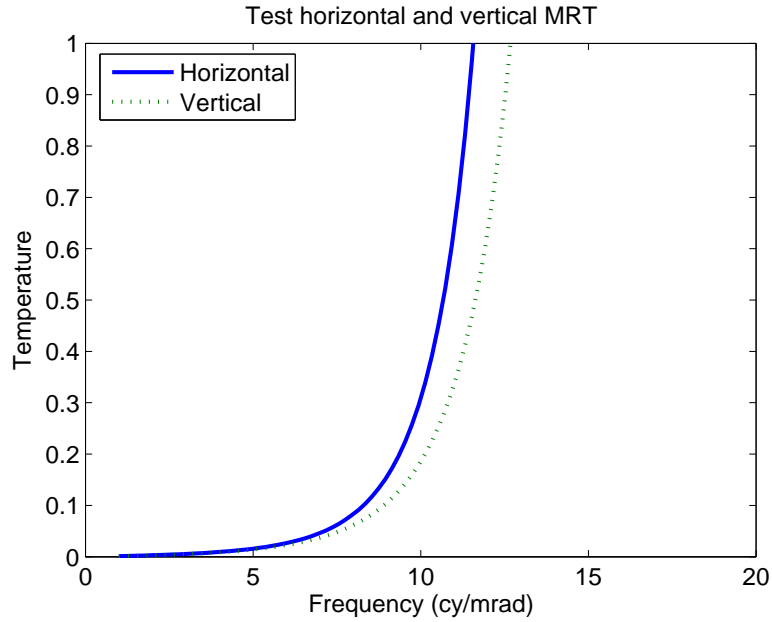


Figure 12. System MRTD showing the Horizontal and Vertical Results.  
The 2-D system MRTD is calculated by taking the geometric average of the horizontal and vertical results, so it would lie between the two.

display luminances and a faster integration time may be appropriate in these cases, such as in the systems used in the field.

### ***b. 2-D MRTD Calculation***

FLIR92 can calculate a 2-D MRTD by taking the geometric mean of the horizontal and vertical MRTDs. In taking the geometric mean, each component is weighted equally and the mean is with respect to the spatial frequency axis. This causes the 2-D MRTD to asymptote at the mean value of the vertical and horizontal cut-off spatial frequencies. These cut-off spatial frequencies are determined by either the Nyquist limits or MTF roll off.

## **5. Calculating the Predicted MDTD**

The basic form for the MDTD calculated in FLIR92 is

$$MDTD(f_s) = \frac{SNR_{TH}\sigma_{tvh}k_{MDT}(f_s)}{A_T Q_h(f_s) Q_v(f_s)} \sqrt{E_t E_h(f_s) E_v(f_s)} \quad (2.35)$$

where the MDTD is independent of target orientation, so  $k_{MDT}(f_s)$  is independent of orientation and is given by Equation 2.33.  $Q_h(f_s)$ ,  $Q_v(f_s)$ , and  $E_v(f_s)$  are defined below and are equivalent for both scanning and staring systems. Along the horizontal direction, the eye/brain spatial integration differs for staring and scanning systems, so each is stated below.  $A_T$  is the target area in  $\text{mrad}^2$  and is related to the spatial frequency,  $f_s$  by

$$A_T = \left( \frac{1}{f_s} \right)^2. \quad (2.36)$$

Equation 2.36 assumes an isometric target, but is a poor approximation for many operation targets that are not so uniform. All other variables are defined as for the MRTD calculation.

The  $Q_h(f_s)$  and  $Q_v(f_s)$  integrals both include the total system MTF,  $H_{SYS}$ . If  $z$  represents the orientation, either horizontal or vertical, then the  $Q_z(f_s)$  integral is

$$Q_z(f_s) = \int_{-\infty}^{\infty} [H_{SYS_z}(\nu)]^2 \left[ \frac{\sin\left(\frac{\pi\nu}{f_s}\right)}{\frac{\pi\nu}{f_s}} \right]^2 d\nu. \quad (2.37)$$

$E_v(f_s)$ , the vertical eye/brain spatial integration, is defined the same way in both the staring and the scanning systems and is of the form

$$E_v(f_s) = \frac{\delta_v}{s_v} \int_{-\infty}^{\infty} [H_{SY S_v}(\nu)]^2 [H_{NF_v}(\nu)]^2 \left[ \frac{\sin\left(\frac{\pi\nu}{f_s}\right)}{\frac{\pi\nu}{f_s}} \right]^2 d\nu. \quad (2.38)$$

$E_h(f_s)$  is defined differently for staring and scanning systems. The coefficient in front of the integral changes. For scanning systems it is of the form,

$$E_h(f_s) = \frac{v_s}{\Delta f_p} \int_{-\infty}^{\infty} S(\nu) [H_{SY S_h}(\nu)]^2 [H_{NF_h}(\nu)]^2 \left[ \frac{\sin\left(\frac{\pi\nu}{f_s}\right)}{\frac{\pi\nu}{f_s}} \right]^2 d\nu. \quad (2.39)$$

For staring systems, it is similar to the vertical direction given in Equation 2.38,

$$E_h(f_s) = \frac{\delta_h}{s_h} \int_{-\infty}^{\infty} [H_{SY S_h}(\nu)]^2 [H_{NF_h}(\nu)]^2 \left[ \frac{\sin\left(\frac{\pi\nu}{f_s}\right)}{\frac{\pi\nu}{f_s}} \right]^2 d\nu. \quad (2.40)$$

## 6. MRTD and MDTD Temperature Dependence

Since background temperature affects the random spatial-temporal noise factor,  $\sigma_{twh}$ , both the MRTD and MDTD calculations are influenced by the background temperature. In FLIR92, the default background temperature is 300 K, but the model can scale  $\sigma_{twh}$  to any background temperature between 240 K and 330 K. Generally, though, predictions made with a background temperature of 300 K are acceptable for most FLIR92 applications. In fact,  $\sigma_{twh}$  is the only 3-D noise component that FLIR92 allows to be scaled to variable background temperatures. Temperature scaling only takes into account the background temperature; there is no scaling to account for the temperature dependence of transmittance in optical materials or noise from photon emissions by variably temperatured sensor components. For details of the temperature scaling of  $\sigma_{twh}$ , see Appendix C.

## 7. Johnson Criteria and FLIR92

The Johnson criteria uses the resolving power of an imager under consideration to provide an estimate for how good the imager will be at target acquisition. The resolving power of the imager in cycles/mrad is multiplied by the target size in mrad to

get the number of cycles on target. This number of cycles on target is then compared to a table of the number of cycles on target needed to detect, recognize, identify, or otherwise perform target acquisition tasks.

## B. NVTHERMIP

Prior to the introduction of NVThermIP, NVTherm was developed to rectify known errors in FLIR92, particularly as regards staring arrays. The FLIR92 model did not take into account the contrast limitations of the observer’s eye. Also, FLIR92 limitations on detector size, spacing, and fill factor caused under-sampled imagery. The new model attempted to compensate for the sampling artifacts by imposing a cutoff at half the sample rate of the imager, but when this result was used with the Johnson metric, resultant predictions were pessimistic. Although the basic MRTD theory used in FLIR92 went into NVTherm and NVThermIP largely unchanged, NVThermIP reworked the eye MTF contribution to improve the pessimistic results from FLIR92. NVThermIP predicts the CTF of thermal imaging systems, but can also predict a laboratory measurement of the the MRTD. NVThermIP also has completely redone the eye MTF. In this report, the CTF is used for comparison to the MRTD so the new eye MTF theory will be included in the comparison.

### 1. MTFs Included in NVThermIP

The MTFs included in NVThermIP are predominantly the same as those included in FLIR92. As in FLIR92, in most cases a user-defined MTF may be entered and is encouraged whenever possible, for more realistic predictions. All the following MTFs are derived from the *NVThermIP User Manual* (NVESD 2005) unless otherwise stated.

#### a. *Optical MTF*

The optical MTF still includes the diffraction-limited MTF and geometric blur MTF, both of the same forms as Equations 2.1 and 2.2a. NVThermIP assumes the optical MTF is the same in the horizontal and vertical directions.

***b. Detector Spatial MTF***

NVThermIP calculates the detector spatial MTF using Equation 2.3b and does not distinguish between SPRITE and non-SPRITE systems. A user-specified MTF would be required to clarify.  $H_{ds}(f_s)$  is not assumed to be symmetric in the horizontal and vertical directions.

***c. Focal Plane Array Integration MTF***

The focal plane array integration MTF is not included in NVThermIP, but could be entered by the user as one of the custom MTFs if so desired.

***d. Sample-scene Phase MTF***

The sample-scene phase MTF is not included in NVThermIP, but could be entered by the user as one of the custom MTFs if so desired.

***e. Image Motion MTF***

In NVThermIP, the only image motion MTF included is the random motion MTF that describes the vibration of the sensor platform. As in FLIR92 Equation 2.7,  $H_{mr}(f_s)$  is assumed to be Gaussian. It is not assumed symmetrical in both directions. User-defined MTFs for linear and sinusoidal motion could be entered, or a total motion MTF defined.

***f. Detector Temporal MTF***

The detector temporal MTF is not included in NVThermIP, but could be entered by the user as one of the custom MTFs if so desired.

***g. Electronics Frequency Responses***

NVThermIP calculates a low pass filter MTF for scanning sensors, only in the horizontal direction. The MTF is the same as Equation 2.10b. No high pass filter MTF is outputted.

***h. Boosting MTF***

The boosting MTF is not included in NVThermIP, but could be entered by the user as one of the custom MTFs if so desired.

***i. Electro-Optical Multiplexer MTF***

In NVThermIP, the electro-optical multiplexer MTF is calculated by Equation 2.12 unless the user specifies an MTF. It varies in the horizontal and vertical directions due to the possible differences in the LED size.

***j. Digital Filter MTF***

The digital filter MTFs in NVThermIP are similar to those in FLIR92, Equations 2.13a and 2.13b, but have a factor to allow for dither. The dither factor,  $D$ , is set to 1 when the user chooses not to include dither. The modified equations are given below. For  $N$  odd the MTF is

$$H_{df}(f_s)_{odd} = \sum_{i=0}^{(N-1)/2} a_i \cos \left[ \frac{2\pi i f_s}{D f_{co}} \right] \quad (2.41a)$$

and for  $N$  even,

$$H_{df}(f_s)_{even} = \sum_{i=1}^{N/2} a_i \cos \left[ \frac{2\pi \left(i - \frac{1}{2}\right) f_s}{D f_{co}} \right]. \quad (2.41b)$$

***k. Display MTF***

Though the display MTF in NVThermIP assumes a CRT display for presenting information to the observer, it includes a factor Ezoom that is not in FLIR92, Equation 2.16. Ezoom,  $E_{zoom}$ , is related to the magnification in the system parameters and this magnification is

$$M = \frac{\theta_{eye}}{FOV_v} = 2 \frac{\arctan \left( \frac{D_H}{2D_{VD}} \right)}{FOV_v} \quad (2.42)$$

where  $D_H$  is the display height in cm,  $D_{VD}$  is the display viewing distance in cm, and  $FOV_v$  is the vertical sensor FOV in mrad. When Ezoom is used, it is assumed that only part of the full FOV will be seen on the display screen. Ezoom examples are given in Table V. Values for  $M$  may vary from  $1/6^{th}$  to 200, but typically are between 0.5 and 20.

Equation 2.16 is modified to include the Ezoom factor by modifying  $\sigma$ :

$$\sigma = \frac{S_w FOV_z}{E_{zoom} D_H} \quad (2.43)$$

Table V. Ezzoom Examples

Portions of total FOV area shown on display screen when different Ezzoom values are used. Values obtained from the *NVThermIP User's Manual* (2005).

<i>Ezoom</i>	<i>M Factor</i>	<i>Vert FOV Seen</i>	<i>Horiz FOV Seen</i>	<i>Tot FOV Area Seen</i>
<i>none</i>	1	1	1	1
<i>single</i>	2	1/2	1/2	1/4
<i>double</i>	4	1/4	1/4	1/16

where  $S_w$  is the physical width of the Gaussian display spot in cm and  $FOV_z$  is the FOV in either the horizontal ( $z = h$ ) or the vertical ( $z = v$ ) direction.

Also, unlike FLIR92, NVThermIP includes MTFs for other possible display types besides CRT, but these are not discussed here since this report focuses on comparing the two models using the same inputs.

***l. CCD Charge Transfer Efficiency MTF***

The CCD Charge Transfer Efficiency MTF is not included in NVThermIP, but could be entered by the user as one of the custom MTFs if so desired.

***m. Display Sample and Hold MTF***

The display sample and hold MTF of Equation 2.18 is again the same in NVThermIP, but is only calculated for scanning systems. Also, it is only applied when calculating the horizontal MTF.

***n. Eye MTF***

NVThermIP handles the eye MTF very differently from FLIR92. NVThermIP considers the human eye point spread function as a combination of three factors: the optics, the retina and the tremor. This leads to an MTF that may be expressed as the product of the component MTFs from the eye optics  $H_{eo}$ , the retina  $H_{ret}$ , and the tremor  $H_{trem}$ :

$$H_{eye}(f_s) = H_{eo}(f_s)H_{ret}(f_s)H_{trem}(f_s). \quad (2.44)$$

Overington (1976) outlines the theory of the human eye MTF and identifies the three component MTFs above. Based on Overington's work, the general forms for the eye

MTF are found, but in NVThermIP, these forms for the eye optical, retinal, and tremor MTF are all empirical (NVESD 2001). The eye optics MTF is

$$H_{eo}(f_s) = \exp \left( - \left[ 43.69 \frac{\left( \frac{f_s}{M_{sys}} \right)}{f_o} \right]^{i_o} \right) \quad (2.45)$$

where  $M_{sys}$  is the imaging system magnification, and  $f_o$  and  $i_o$  are defined below,

$$f_o = \exp \left( 3.663 - 0.0216 D_p^2 \log_{10}(D_p) \right) \quad (2.46a)$$

$$i_o = \left( 0.7155 + \frac{0.277}{\sqrt{D_p}} \right)^2. \quad (2.46b)$$

The variable  $D_p$  is the pupil diameter in mm and is valid if one eye is used. If two eyes are used, then NVThermIP reduces the pupil diameter by 0.5mm.  $D_p$  is defined as

$$D_p = -9.011 + 13.23 \exp \left( - \frac{\log_{10}(f_L)}{21.082} \right) \quad (2.46c)$$

where  $f_L$  is the number of foot-Lamberts at the eye from the display and is  $f_L = \frac{L_d}{0.929}$ .  $L_d$  is the display luminance in milli-Lamberts. The retina MTF is defined as

$$H_{ret}(f_s) = \exp \left( -0.375 \left[ \frac{f_s}{M_{sys}} \right]^{1.21} \right). \quad (2.47)$$

The tremor MTF, or the MTF of the eye due to tremor, is

$$H_{trem}(f_s) = \exp \left( -0.4441 \left[ \frac{f_s}{M_{sys}} \right]^2 \right). \quad (2.48)$$

Clearly, then, the MTFs depend on the pupil diameter, which in turn depends on the light level.

Figure 13 compares the eye MTFs in FLIR92 and NVThermIP. Clearly, NVThermIP has a more optimistic estimate of the image degradation due to the observer's eye, which reduces the known error in the FLIR92 modeling of the human eye.



***o. System Noise Filter MTF***

The system noise filter MTF is merely the roll-up of all the system noise. In NVThermIP, there is a further factor for system noise that is requested as a user-input. NVThermIP considers that each system has a different fixed pattern noise associated with variations in detector gain and level offset. There are three options in the NVThermIP input: *None*, *Noise Factor*, and *3-D Noise*. If *None* is selected, then the system is considered ideal with no variations in gain and level offset among the detectors. For *Noise Factor*, experimentally-determined independent horizontal and vertical factors are multiplied by the horizontal and vertical noise CTFs. The *3-D Noise* is discussed in a later section about system noise.

***p. Interpolation MTF***

NVThermIP includes an MTF for interpolation, or the process of increasing the image size by inserting ‘filler’ pixels between the original pixels. Interpolation may be done either vertically or horizontally, and if interpolation is selected for

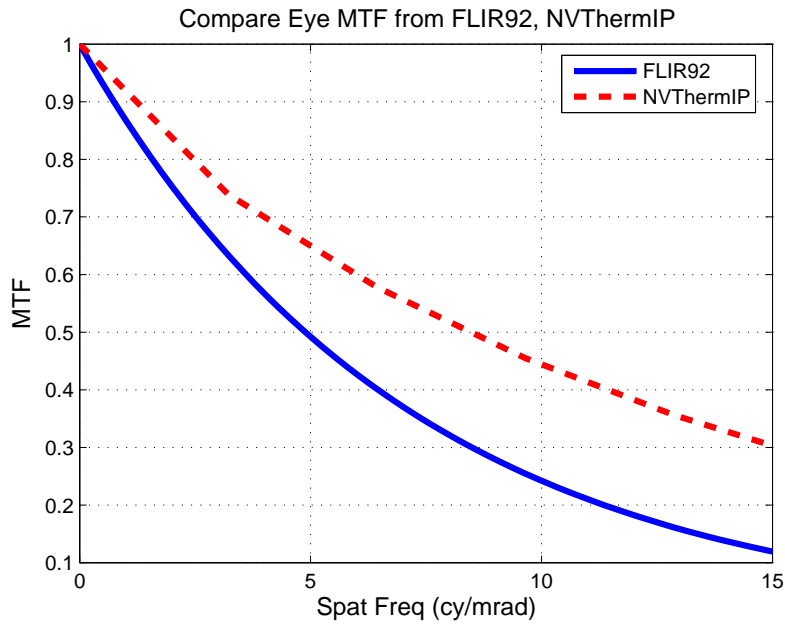


Figure 13. Comparing the Eye MTF in FLIR92 and NVThermIP in the Horizontal Direction.

both directions, only one is applied at a time. The results are then combined. NV-ThermIP offers three different methods for interpolation, *Pixel Replication*, *Bilinear Interpolation*, and *Bicubic Interpolation*. In this report, since FLIR92 does not offer interpolation, no interpolation is selected.

#### **q. Optical Turbulence MTF**

Unlike FLIR92, operational NVThermIP already includes an MTF for optical turbulence. This turbulence MTF assumes that  $C_n^2$  is constant along the pathlength and so is an average MTF.  $C_n^2$  is a parameter that describes the optical turbulence in the atmosphere and more thoroughly defined in Chapter III. The formulation is very similar to the Goodman results for constant  $C_n^2$  given in Equation A.98 in Appendix A. The equation is given below,

$$H_{at}(f_s) = \exp \left( -57.4 a f_s^{\frac{5}{3}} C_n^2 \lambda^{-\frac{1}{3}} z \left( 1 - \frac{1}{2} \left[ \frac{\lambda f_s}{D} \right]^{\frac{1}{3}} \right) \right) \quad (2.49)$$

where  $a$  is a constant defined as  $\frac{3}{8}$ ,  $f_s$  is here defined in cycles/rad,  $C_n^2$  is still in  $\text{m}^{-\frac{2}{3}}$ , and  $\lambda$ ,  $z$ , and  $D$  are all in m.

## **2. Sampling**

### **a. Sample Spacing**

For an imaging system, the sample spacing quantifies the limits due to sampling. For staring systems, the sample spacing can be calculated in the horizontal and vertical directions by

$$\alpha_{SS_z} = \frac{FOV_z}{N_z} \quad (2.50a)$$

where  $z$  indicates the target orientation, either horizontal or vertical.  $N_z$  is the number of detectors in the  $z$  direction.  $\alpha_{SS_z}$  is in mrad. For a scanning system, the vertical sample spacing is calculated as per Equation 2.50a, but in the horizontal direction the sample spacing is different. There is no sample spacing in a continuously scanning system, so  $\alpha_{SS_h} = 0$ . A scanning system that samples has a sample spacing requires a user-input of  $N_{HIFOV}$ , or samples per HIFOV. Then the sample spacing is

$$\alpha_{SS_h} = \frac{DAS_h}{N_{HIFOV}}. \quad (2.50b)$$

$DAS_h$  is the detector angular subtense (DAS) in the horizontal direction, in other words, the detector width divided by the focal length of the collecting optics.

### ***b. Sample Frequency***

As explained in Section II.A.2.b, the sampling frequency is just the inverse of the sample spacing, Equations 2.50a or 2.50b. Thus, the sampling frequency is

$$f_{samp} = \frac{1}{\alpha_{SS_z}}. \quad (2.51)$$

Since the horizontal and vertical sample spacing may differ, the horizontal and vertical  $f_{samp}$  may also differ. Again the half sample frequency is the Nyquist frequency.

## **3. System Noise**

As mentioned in Section II.B.1.o, the 3-D system noise is handled in a similar manner to FLIR92. The 3-D system noise components are defined in Table VI, essentially the same as Table I.

Table VI. 3-D Noise Component Descriptions in NVThermIP  
Subscripts of noise components shown in table indicate dimension:  $t$  temporal,  $v$  vertical spatial,  $h$  horizontal. Table derived from *NVThermIP User's Manual* (NVESD 2005).

<i>Noise</i>	<i>Description</i>	<i>Potential Source</i>
$\sigma_{tvh}$	random spatio-temporal noise	Basic Detector Temporal Noise
$\sigma_{tv}$	temporal row noise, line bounce	Line Processing, $\frac{1}{f}$ , read-out
$\sigma_{th}$	temporal column noise, column bounce	Scan Effects
$\sigma_{vh}$	random spatial noise, bi-directional fixed pattern noise	Pixel Processing, Detector-to-Detector Non-Uniformity $\frac{1}{f}$
$\sigma_v$	fixed row noise, line-to-line non-uniformity	Detector-to-Detector Non-Uniformity
$\sigma_h$	fixed column noise, column-to-column non-uniformity	Scan Effects, Detector-to-Detector Non-Uniformity
$\sigma_t$	frame-to-frame noise, frame bounce	frame processing
$S$	mean of all noise components	

As in FLIR92, these eight noise parameters are derived using directional averages.  $\sigma_{tvh}$  is predicted and all other components are estimated based on historical databases of measurements. In Table VI, the subscript that is missing indicates which directions were averaged so, for example,  $\sigma_{tv}$  was averaged in the horizontal and  $\sigma_v$  in both the temporal and horizontal. Again similar to FLIR92, only certain noise parameters are considered important in scanning and staring systems. Table VII shows the key parameters for scanning systems, where the noise term is normalized using the random spatio-temporal noise  $\sigma_{tvh}$ .

Table VII. Noise Values for Scanning Systems in NVThermIP  
Subscripts of noise components shown in table indicate dimension:  $t$  temporal,  $v$  vertical spatial,  $h$  horizontal. Table derived from *NVThermIP User's Manual* (NVESD 2005).

<i>Noise Term</i>	<i>Low</i>	<i>Moderate</i>	<i>High</i>
$\sigma_{vh}/\sigma_{tvh}$	0	0	0
$\sigma_v/\sigma_{tvh}$	0.25	0.75	1
$\sigma_h/\sigma_{tvh}$	0	0	0

Table VIII shows the key parameters for staring systems, where the noise term is again normalized with  $\sigma_{tvh}$ . Table VIII compares to Table III.

Table VIII. Noise Values for Staring Systems in NVThermIP  
Subscripts of noise components shown in table indicate dimension:  $t$  temporal,  $v$  vertical spatial,  $h$  horizontal. Table derived from *NVThermIP User's Manual* (NVESD 2005).

<i>Noise Term</i>	<i>Low</i>	<i>Moderate</i>	<i>High</i>
$\sigma_{vh}/\sigma_{tvh}$	0.2	0.5	1 - 2
$\sigma_v/\sigma_{tvh}$	0.2	0.5	1 - 2
$\sigma_h/\sigma_{tvh}$	0.2	0.5	1 - 2

**a. Random Spatio-temporal Noise,  $\sigma_{tvh}$**

The random spatio-temporal noise is calculated similarly in NVThermIP as in FLIR92, but includes a factor to account for the number of detectors. Again,  $\sigma_{tvh}$  is calculated assuming a background temperature of 300K and the relationship,

$$\sigma_{tvh} = \frac{4f_{no}^2 \sqrt{\Delta f_p}}{\tau_0 \sqrt{A_d N} \int_{\lambda_1}^{\lambda_2} D^*(\lambda, 300) \frac{\partial W}{\partial T_{300}}(\lambda) d\lambda} \quad (2.52)$$

where N is the number of detectors and all other variables are defined as for Equation 2.26. Note that Equation 2.52 differs from Equation 2.26 by a factor of  $\pi$  in the denominator.

#### 4. Calculating the Predicted MRTD

NVThermIP outputs three laboratory measurements of the MRTD: *high gain*, *low gain*, and *user input*. The basic equation used in all cases is

$$MRTD_z(f_s) = \frac{2SCN_{TMP}CTF_{eye}(f_s)}{(A_{bar}(f_s) - A_{spc}(f_s))S_L} \sqrt{1 + \frac{\alpha^2 \Gamma_{det}^2 QH_z(f_s) QV_z(f_s)}{SCN_{tmp}^2}}. \quad (2.53)$$

Here,  $SCN_{TMP}$  is the scene contrast temperature that generates the average display luminance in K,  $CTF_{eye}(f_s)$  is the naked eye CTF,  $A_{bar}$  is the area of the bar in the target in  $\text{cm}^2$ ,  $A_{spc}$  is the area of the space between bars in the target in  $\text{cm}^2$ ,  $S_L$  is the unitless normalized laboratory detector responsivity,  $\Gamma_{det}$  is the noise variance in  $\text{K-mrad-s}^{\frac{1}{2}}$ , and  $QH_z$  and  $QV_z$  are the horizontal and vertical noise bandwidth for the horizontal system CTF and the vertical system CTF. The laboratory conditions can be strictly controlled, which is important because in this calculation when  $A_{bar}(f_s) = A_{spc}(f_s)$ , the MRTD will be undefined.

The laboratory MRTD in NVThermIP is difficult to compare directly to the MRTD in FLIR92 for many reasons. Two of particular concern in this study were the high, low, and user gain of NVThermIP - there is no equivalent in FLIR92 - and the fact that NVThermIP calculates the MRTD for laboratory conditions which are highly controlled and not equivalent to the conditions assumed in FLIR92. Since

the laboratory MRTD outputted by NVThermIP is not directly comparable to the MRTD from FLIR92, a work-around was proposed in conversations with Jon Hixson (Army Research Labs, Fort Belvoir, VA). The CTF outputted from NVThermIP can be manipulated to obtain an MRTD comparable to FLIR92 by multiplying  $2 \times$  the SCT. NVThermIP produces a system CTF in the horizontal and vertical directions following Equations 2.54a and 2.54b:

$$CTF_{H_{sys}}(f_{s_h}) = \sqrt{[CTF_{H_{eye}}(f_{s_h})]^2 + \left[ \frac{CTF_{H_{noise}}(f_{s_h})}{SCN_{tmp}} \right]^2} \quad (2.54a)$$

$$CTF_{V_{sys}}(f_{s_v}) = \sqrt{[CTF_{V_{eye}}(f_{s_v})]^2 + \left[ \frac{CTF_{V_{noise}}(f_{s_v})}{SCN_{tmp}} \right]^2} \quad (2.54b)$$

where the eye CTFs and the noise CTFs in the horizontal and vertical directions are defined as

$$CTF_{H_{noise}}(f_{s_h}) = \sqrt{\alpha^2 \Gamma_{det}^2 QH_{hor}(f_{s_h}) QV_{hor}} \left( \frac{CTF_{eye}\left(\frac{f_{s_h}}{S_{MAG}}\right)}{M_{disp} MTF_{H_{sys}}(f_{s_h})} \right) \quad (2.56a)$$

$$CTF_{V_{noise}}(f_{s_v}) = \sqrt{\alpha^2 \Gamma_{det}^2 QH_{ver}(f_{s_v}) QV_{ver}} \left( \frac{CTF_{eye}\left(\frac{f_{s_v}}{S_{MAG}}\right)}{M_{disp} MTF_{V_{sys}}(f_{s_v})} \right) \quad (2.56b)$$

$$CTF_{H_{eye}}(f_{s_h}) = \frac{CTF_{eye}\left(\frac{f_{s_h}}{S_{MAG}}\right)}{M_{disp} MTF_{H_{sys}}(f_{s_h})} \quad (2.56c)$$

$$CTF_{V_{eye}}(f_{s_v}) = \frac{CTF_{eye}\left(\frac{f_{s_v}}{S_{MAG}}\right)}{M_{disp} MTF_{V_{sys}}(f_{s_v})}. \quad (2.56d)$$

The  $M_{disp}$  is the display glare and  $\alpha$  is a proportionality constant of  $169.6 \text{ Hz}^{\frac{1}{2}}$ .  $SCN_{tmp}$  is solicited from the user and considered a constant throughout calculations.

## 5. Detector Cooling in NVThermIP

NVThermIP allows for the selection of an uncooled detector. Selecting this option requires a user input of a performance measurement for the uncooled array in terms of the measured detector noise, detector frame rate, f-number, and optics transmission. Then, NVThermIP will calculate a peak  $D^*$  and integration time for the uncooled sensor.

## **6. Targeting Task Performance (TTP) Metric and NV-ThermIP**

Unlike FLIR92 and previous version of of NVTherm, NVThermIP uses the Targeting Task Performance (TTP) metric to predict the probability of successful task performance. Since this study does not utilize the range performance predictions from NVThermIP, no further details are provided here, but for more information, see the *NVThermIP User's Manual* (NVESD 2005).

THIS PAGE INTENTIONALLY LEFT BLANK



### III. OPTICAL TURBULENCE MODEL CHOICE

Optical systems operating in a turbulent atmosphere experience broadening of the point spread function, which is best described using a specific atmospheric MTF. For a collimated beam passing through the atmosphere, turbulence distorts the shape of the wavefront and causes variations of intensity along the wavefront so that when the beam is brought back into focus by some optical system, the image formed has been altered by the atmospheric affects. Driggers (1999) notes that the atmospheric MTF may be expressed as two separate MTFs created by two different effects in the atmosphere: scattering due to aerosols and blurring due to turbulence. In this study, the MTF describing scattering due to aerosols is neglected.

This study uses the mathematical model of the atmospheric turbulence MTF developed by Goodman (1985). Various mathematical determinations of the atmospheric parameter  $C_n^2$  are considered for use in the atmospheric turbulence MTF calculation, in order to most appropriately represent  $C_n^2$  through the whole atmosphere.

#### A. OPTICAL TURBULENCE AND ATMOSPHERIC $C_N^2$

According to the *IREO Handbook* Vol.2 (1993), turbulence in the atmosphere creates random variations in the atmosphere's index of refraction. These irregularities distort the wavefronts that pass through them and thereby cause image distortion or blur in imaging systems. Although there are different geometries for describing turbulent systems, the applicable one in dealing with airborne and ground-based sensors is spherical wave propagation. In this case, the propagating light comes from sources that are in or near the turbulence, as in the imaging of objects in the turbulent atmosphere. The sensors receiving the light are also in the turbulent atmosphere. Although this study focuses on the airborne sensor situation where a target on the

surface is imaged by an over-flying aircraft, it is important to note that it is the turbulence at the sensor that most strongly affects the image quality.

Operationally, the best estimate of atmospheric turbulence would be determined from an analysis or forecast, but when a local estimate is not available, the atmospheric turbulence may be predicted using models that estimate the atmospheric structure parameter  $C_n^2$ , as described below. The atmospheric structure parameter  $C_n^2$  describes atmospheric variations in the index of refraction. Essentially, fluctuations in the index of refraction along the path between the target and the sensor causes some IR radiation to be randomly bent from the path, resulting in a blurred image at the sensor. The more turbulent the atmosphere, the greater the blurring.  $C_n^2$  is best defined by Equation 3.57,

$$C_n^2(x) = \overline{[n(x) - n(x+r)]^2} r^{-\frac{2}{3}} \quad (3.57)$$

where  $n(x)$  is the index of refraction at a point  $x$  in the atmosphere and  $n(x+r)$  is the index of refraction some distance  $r$  away from  $x$ . The over-bar indicates an average over the representative part of the atmosphere by either averaging  $n$  over time at one location or space at a very short time (Goroch 1980).

Atmospheric variations in the index of refraction are described by  $C_n^2$ . The generic form of how  $C_n^2$  varies in the atmosphere is given by Friehe (1977) as

$$C_n^2 = \left(79 \times 10^{-6} \frac{P}{T^2}\right)^2 \left(C_T^2 + 0.113C_{TQ} + 3.2 \times 10^{-3}C_Q^2\right) \quad (3.58)$$

where  $P$  is the pressure in mb,  $T$  is the temperature in K,  $C_T^2$  is the temperature structure function parameter,  $C_{TQ}$  the temperature-water vapor parameter and  $C_Q$  the water vapor parameter, all in  $\text{K}^2/\text{m}^{-\frac{2}{3}}$ . The *IREO Handbook* Vol.2 (1993) states that the dry-air, or  $C_T^2$ , term dominates in most applications since generally the  $C_{TQ}^2$  and  $C_Q^2$  terms comprise no more than 2% of the total  $C_n^2$ . Since  $C_T^2$  is typically the dominant term in  $C_n^2$ , in this study it will be considered the only contributor. All three structure parameters vary depending on location in the boundary layer (Fairall 1982). Although it will not be addressed in this study, it should be noted that in the

microwave part of the spectrum,  $C_n^2$  depends much more strongly on the humidity and  $C_{TQ}$  and  $C_Q$  are large contributors to the overall  $C_n^2$  (Fante 1980). Also, in rare situations in the IR part of the spectrum,  $C_{TQ}$  may be more significant (*IREO Handbook* Vol.2 1993).

## 1. Turbulence Near the Ground

There are two primary ways that the ground impacts the movement of air and causes turbulence. First, the free air stream flowing along the ground experiences friction due to surface roughnesses, which causes wind shear. Second, the ground may serve as a source or a sink for thermal energy of the air. Given sunny conditions during the day, the ground will be a source of heat because the sun warms the ground to a temperature higher than the air above it. This leads to thermal convection and instability. At night, the ground will act as a heat sink by radiative cooling, resulting in a ground temperature colder than the air above it. These conditions are considered stable. When the air and the ground are at the same temperature, atmospheric conditions are considered neutral. These extreme fluctuations in ground temperature are observed over land, but over the ocean the temperature difference between night and day is much less. The variation in temperature differences was the primary motivation for comparing FLIR92 and NVThermIP over desert and marine locations.

Fairall et. al. (1982) propose that in the surface layer of the atmosphere, the structure function parameters have the forms of

$$C_T^2 = T_*^2 Z^{-\frac{2}{3}} f(\xi) \quad (3.59a)$$

$$C_Q^2 = Q_*^2 Z^{-\frac{2}{3}} A f(\xi) \quad (3.59b)$$

$$C_{TQ} = r_{TQ} T_* Q_* Z^{-\frac{2}{3}} \sqrt{A} f(\xi) \quad (3.59c)$$

where  $T_*$  and  $Q_*$  are temperature and humidity scaling parameters in K and g/m<sup>3</sup> respectively,  $f(\xi)$  is a dimensionless function, and  $r_{TQ}$  is the temperature-humidity correction parameter. Fairall et. al. (1982) gives an estimate value of 0.8 for  $r_{TQ}$  in

unstable conditions such as those being studied here.  $A$  is a constant, taken to be 0.6.  $Z$  is the height above the surface in m.

The dimensionless function  $f(\xi)$  is connected to the Richardson number, so it accounts for varying conditions depending on the stability. Wyngaard et. al. (1971) determined the empirical form,

$$f(\xi) = 4.9(1 - 7.0\xi)^{-\frac{2}{3}} \quad \xi < 0 \quad (3.60a)$$

$$f(\xi) = 4.9 \quad \xi = 0 \quad (3.60b)$$

$$f(\xi) = 4.9(1 + 2.75\xi) \quad \xi > 0 \quad (3.60c)$$

where  $\xi < 0$  corresponds to unstable conditions (as under consideration here),  $\xi = 0$  is neutral and  $\xi > 0$  is stable. Wyngaard originally split  $f(\xi)$  into two segments of  $\xi \leq 0$  and  $\xi \geq 0$ , but the neutral case has been added here to show when  $f(\xi)$  is a constant.  $\xi$  itself is defined as the height scaled by the Monin-Obukhov length scale,

$$\xi = \frac{Z}{L} = \frac{\kappa g Z \left( T_* + 0.61 T_a \frac{Q_*}{\rho} \right)}{T_a u_*^2}. \quad (3.61)$$

$L$  is the Monin-Obukhov length scale and is defined as the height over the ground where the mechanically produced turbulence from vertical shear balances the dissipative effect of negative buoyancy. In other words, the Richardson number equals unity.  $L$  may be expressed as

$$L = \frac{T_a u_*^2}{\kappa g \left( T_* + 0.61 T_a \frac{Q_*}{\rho} \right)} \quad (3.62)$$

where  $\kappa$  is the unitless von Karman constant that Fairall et. al. approximate to 0.35,  $g$  is the gravitational acceleration on earth taken as 9.8 m/s<sup>2</sup>,  $Q_*$  is the humidity scaling parameter in g/m<sup>3</sup>,  $\rho$  is the density of air in kg/m<sup>3</sup>, and  $u_*$  is the frictional velocity in m/s. In this case, the density of air is taken as 1.3 kg/m<sup>3</sup>.  $T_a$  is the temperature of the ambient air in the region of interest, in K.

If  $C_n^2$  is taken to primarily depend on  $C_T^2$  as was assumed above, then Equations 3.59b and 3.59c may be neglected and their terms in Equation 3.58 dropped. Davidson

et. al. (1978) indicate that above the ocean and within 10m of the ocean surface,  $C_T^2$  varies as  $Z^{-\frac{4}{3}}$ , but above that 10m,  $C_T^2$  varies as  $Z^{-\frac{2}{3}}$ . This is better seen by solving Equation 3.59a for the conditions given in Equations 3.60, as shown below where again  $\xi = \frac{Z}{L}$ ,

$$C_T^2 = 4.9T_*^2 Z^{-\frac{2}{3}} [1 - 7\xi]^{-\frac{2}{3}} \quad \xi < 0 \quad (3.63a)$$

$$C_T^2 = 4.9T_*^2 Z^{-\frac{2}{3}} \quad \xi = 0 \quad (3.63b)$$

$$C_T^2 = 4.9T_*^2 Z^{-\frac{2}{3}} (1 + 2.75\xi) \quad \xi > 0 \quad (3.63c)$$

Substituting Equation 3.61 into 3.63 for the three cases of unstable, neutral, and stable  $C_T^2$  respectively, yields

$$C_T^2 \simeq \frac{4}{3} T_*^2 Z^{-\frac{4}{3}} L^{\frac{2}{3}} \quad (3.64a)$$

$$C_T^2 = 4.9T_*^2 Z^{-\frac{2}{3}} \quad (3.64b)$$

$$C_T^2 \simeq 13.5T_*^2 Z^{\frac{1}{3}} L^{-1}. \quad (3.64c)$$

In unstable conditions,  $|\xi| \gg 1$  (Equation 3.64a), so  $(1 - 7\xi)^{-\frac{2}{3}}$  can be approximated as  $(-7\xi)^{-\frac{2}{3}}$ . In the stable case,  $|\xi| \ll 1$  (Equation 3.64c), so  $(1 + 2.75\xi)$  is approximately  $2.75\xi$ . Other authors indicate that for  $|\xi| \ll 1$ ,  $C_T^2$  may even be taken as independent of  $Z$ .

The above discussion applies over the ocean, but Hall (1977) observed that in unstable conditions near land surface,  $C_n^2$  still decreases with height by  $Z^{-\frac{4}{3}}$ . The  $Z^{-\frac{4}{3}}$  height dependence frequently continues beyond 10m over land, but is still only valid in the surface layer.

## 2. Turbulence Above the Surface Layer

In the so-called mixed layer above the surface layer, Fairall et. al. (1982) offer definitions for  $C_T^2$ ,  $C_Q^2$ , and  $C_{TQ}$  where in all cases  $C_n^2$  falls off as a function of  $Z^{-\frac{4}{3}}$ . They are very similar to Equation 3.60, so in this study, Equation 3.60 is used beyond the lowest surface layers.

Above the mixed layer, one possible model of  $C_n^2$  behavior is the Hufnagel model. Goodman (1985) offers a possible analytic approximation to how  $C_n^2$  varies in the vertical and references the work by Hufnagel and Stanley (1964). This approximation is

$$C_n^2(Z) = 2.7 \times 10^{-16} \left[ 3 \langle u^2 \rangle \left( \frac{Z}{10} \right)^{10} e^{-Z} + e^{-\frac{Z}{1.5}} \right] \quad (3.65)$$

where  $Z$  is the location along the flight path in km and  $\langle u^2 \rangle$  is the mean value of the squared wind speed.  $C_n^2$  is again in  $\text{m}^{-\frac{2}{3}}$ . This approximation reasonably represents the average variation of  $C_n^2$  in the middle to upper atmosphere but poorly represents the boundary layer. Variations of  $C_n^2$  in the boundary layer differ extensively depending on the stability of the boundary layer, as described above. Fante (1980) and other sources indicate that the Hufnagel approximation agrees fairly well with observation starting around 5 km above the surface.

### 3. Turbulence Through Whole Atmosphere

In this study, the atmospheric structure parameter  $C_n^2$  is taken to follow the bulk method below 200 m and the Hufnagel formulation above the 5 km point. It is worth noting that the Hufnagel formulation is an early numerical model of the upper atmospheric structure parameter and is generally only considered valid for above 5 km in the atmosphere. For simplicity in MatLab programming, between 200 m along the pathlength and 5 km, an average value of  $1 \times 10^{-16} \text{ m}^{-\frac{2}{3}}$  was chosen. It is near the surface that  $C_n^2$  varies the most and is the largest, so the actual choice for  $C_n^2$  above the surface layer was of less concern than that in the surface layer. The  $C_n^2$  calculation is summarized in Equation 3.66,

$$C_n^2 = \text{BulkMethod} \quad Z < 200m \quad (3.66a)$$

$$C_n^2 = 1 \times 10^{-16} \text{m}^{-\frac{2}{3}} \quad 200m < Z < 5000m \quad (3.66b)$$

$$C_n^2 = \text{HufnagelMethod} \quad Z > 5000m. \quad (3.66c)$$

In order to test the validity of these assumptions, the bulk method and the Hufnagel formulation were plotted for several temperature differences. In Figure 14, the surface

temperature is taken to be 28°C and the ambient air temperature 25°C. Other parameters are given in Table IX, where for this test case, generic parameters are chosen. The two methods intersect below 200 m, but at 200 m the  $C_n^2$  values are on the order of  $1 \times 10^{-16} \text{ m}^{-\frac{2}{3}}$ , which agrees fairly well with results from Fairall et. al. (1982) and other sources. Values differed by less than an order of magnitude using the Hufnagel model at 5 km. The choice of a constant  $C_n^2$  in the middle atmosphere simplified the MatLab programming, but the small scale of  $C_n^2$  and the relatively small difference between the two models around the 500 m to 5000 m layer suggested that choosing a constant  $C_n^2$  was reasonably representative of the atmospheric conditions. Note that for simplicity in the MatLab programming, the bulk method, which describes  $C_n^2$  in the surface layer, is taken to be valid up to 200 m. This does not mean that the surface layer itself extends up to 200 m. Rather, the bulk method is assumed valid up to 200 m, so the bulk method may be assumed valid beyond the surface layer.

Table IX. Parameters for  $C_n^2$  Test Cases.  
Generic parameters chosen to test the Bulk and Hufnagel formulations of  $C_n^2$ .

<i>Parameter</i>	<i>Value</i>	<i>Units</i>
Rel Humidity Ambient Air	0.8	fraction
Rel Humidity Sfc Air	1.0	fraction
Wind Speed	7	m/s
Sfc Pressure	1012	hPa
Thermal Sfc Roughness	0.02	m
Momentum Sfc Roughness	0.02	m
Total Pathlength	10,000	m

After comparing the bulk method and the Hufnagel method for a sample test case, the two methods were compared for conditions at White Sands and Point Conception (data give in Chapter IV). As indicated in Figures 15 and 16, the assumed constant value of  $1 \times 10^{-16} \text{ m}^{-\frac{2}{3}}$  appears fairly representative between the two models. Also, the exponential behavior of the bulk method near the surface, in both cases, indicates how much stronger turbulence is near the ground.

Note that while the surface bulk model and Hufnagel model were used in this study, there are numerous other models of the atmospheric structure parameter. It is also important to note that this study does not consider possible surface inversions and neglects the stable case.

## B. MTF FOR OPTICAL TURBULENCE

The Goodman (1985) formulation for atmospheric optical turbulence was chosen for this study. It can be expressed for the long-exposure and short-exposure case, although the focus here is on the long-exposure case.

The long-exposure and short-exposure atmospheric turbulence MTFs differ

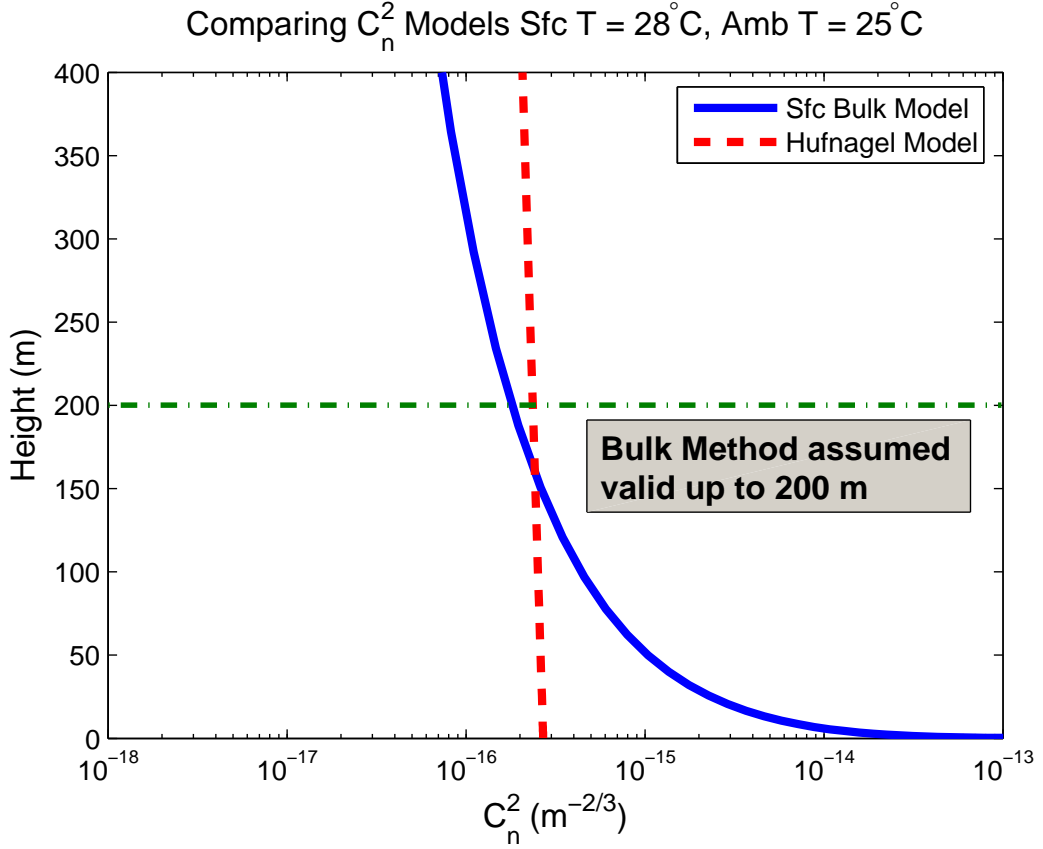


Figure 14. Comparison of the Bulk and Hufnagel Methods with Sfc Temp 28°C. At 28°C, the two methods intersect at 158 m. At 200 m, the bulk method has a  $C_n^2$  value of approximately  $1 \times 10^{-16} \text{ m}^{-2/3}$ . The bulk method is used below 200 m.



substantially. In the long-exposure case, the exposure time is such that the phase and log-amplitude vary over the course of the exposure. Thus during a long exposure, the image recorded will be spread due to random variations in the tilt of the wavefront. To consider the short-exposure case, a random factor associated with the wavefront tilt is extracted from the MTF before the average is taken. This is not done for the long-exposure case. For the extremely short exposures, there will be no impact from the wavefront tilt and it is ignored in determining the MTF (Fried 1966).

The derivation for the Goodman atmospheric MTF is summarized in Appendix A. Using the generic atmospheric input parameters given in Table IX, the Goodman long exposure atmospheric turbulence MTF is orders of magnitude smaller than the other MTFs included in FLIR92. In Figure 17, Goodman MTF is subtracted

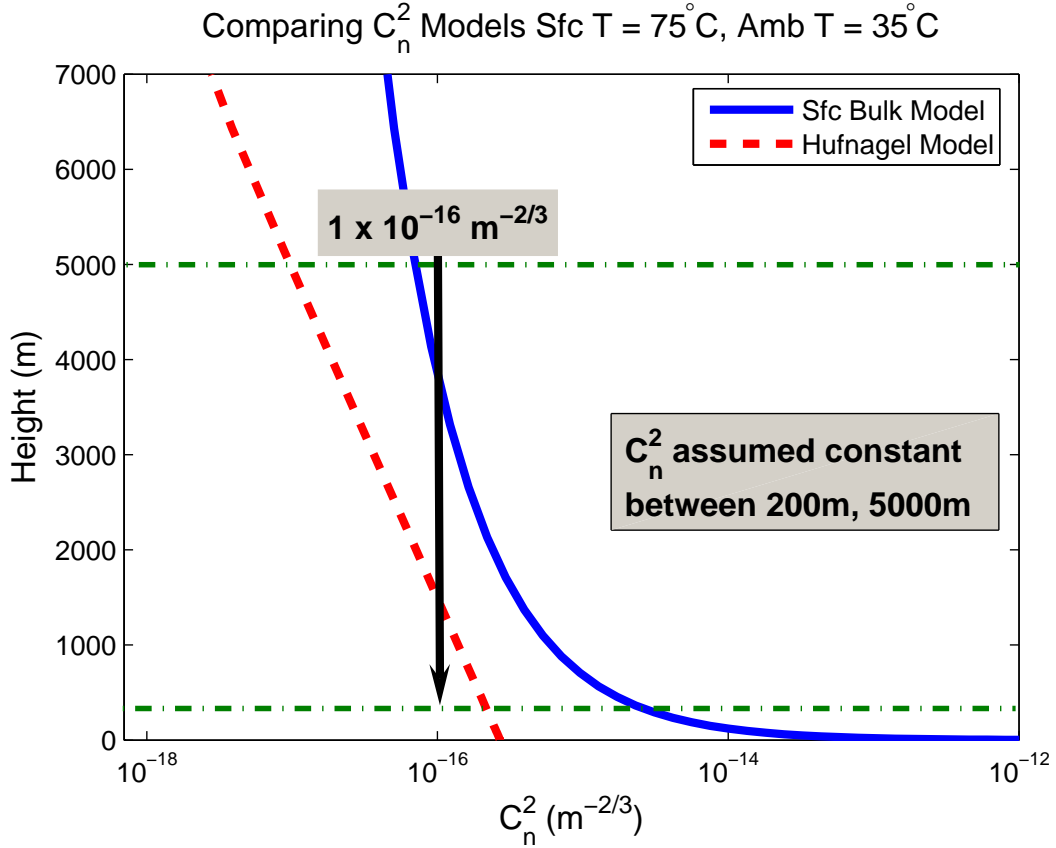


Figure 15. Comparison of the Bulk and Hufnagel Methods at White Sands.

from unity to better illustrate the form of the MTF. The  $C_n^2$  used in the Goodman calculations may be calculated using Equation 3.66.

From the above discussions, it appears that  $C_n^2$  is most significant near the surface. In one illustration of this, the Goodman atmospheric MTF is examined for a variety of slant angles starting with a path perpendicular to the surface, and ending with a virtually horizontal path through the surface layer, parallel to the surface. Figure 18 illustrates the Goodman MTF at various slant angles, for a constant pathlength of 100 m. Plotted is unity minus the Goodman MTF, as in Figure 17, to best observe this small scale MTF. Although Figure 18 makes it clear that even close to parallel to the surface, the Goodman MTF is small scale, still the resultant MTF is more significant at smaller slant angles.

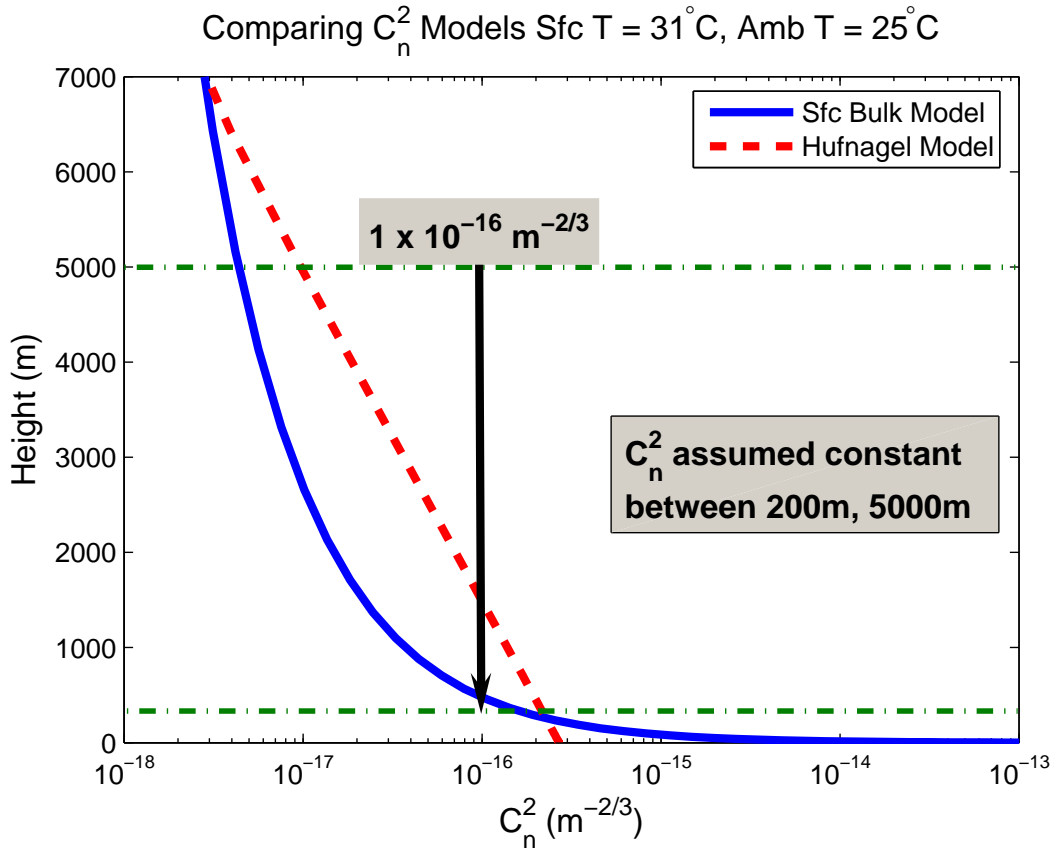


Figure 16. Comparison of the Bulk and Hufnagel Methods at Pt Conception.

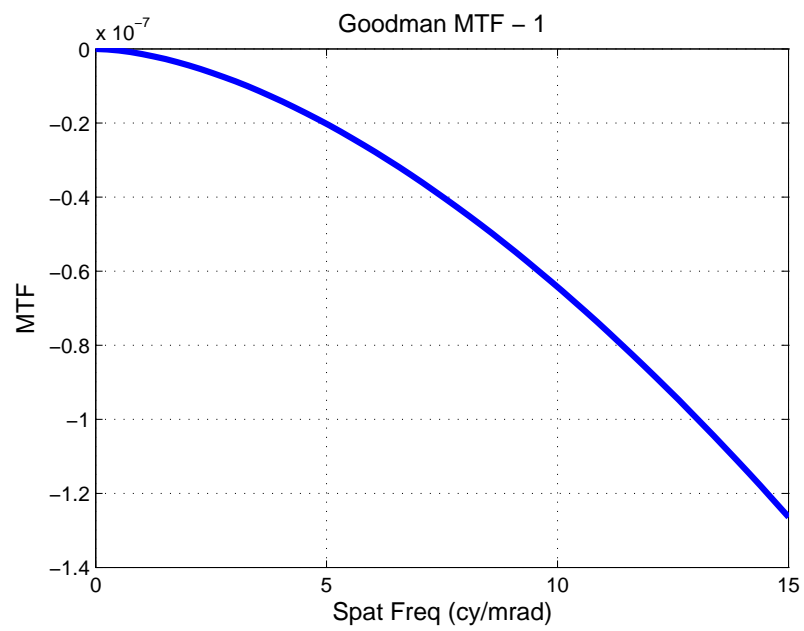


Figure 17. Goodman Long Exposure Atmospheric Turbulence MTF.  
 Note the small scale of the atmospheric turbulence MTF. Plot is of (1 - Goodman MTF).

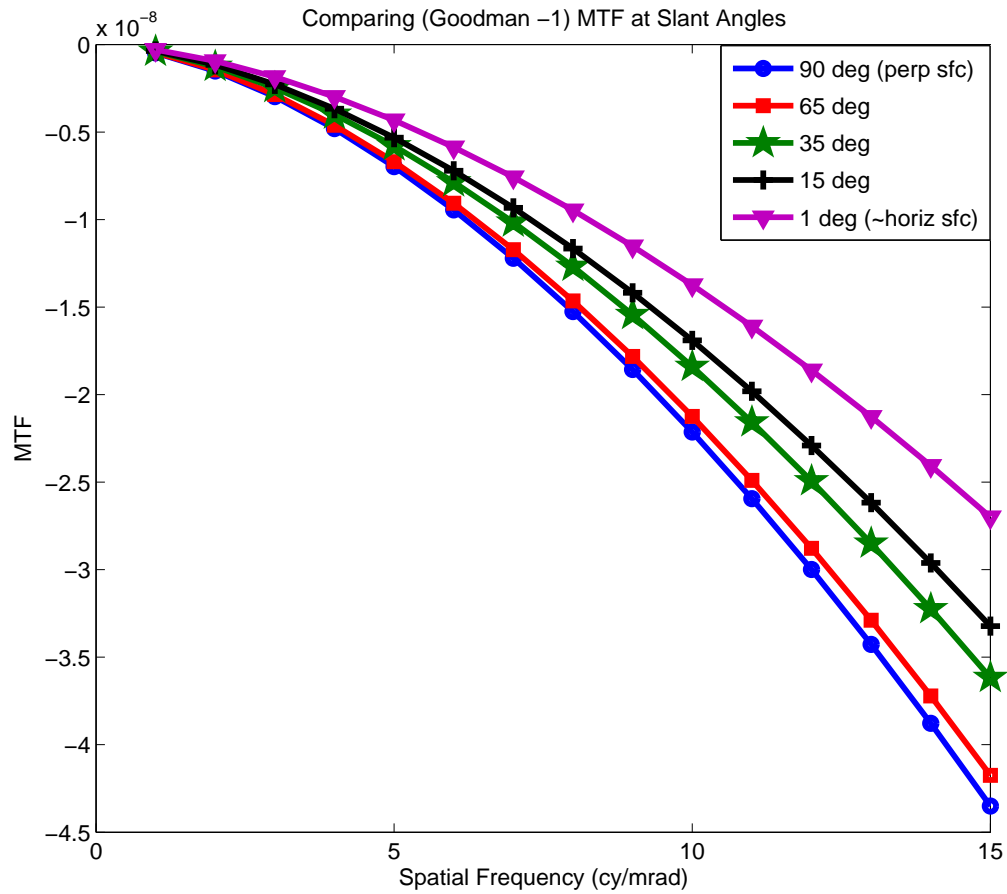


Figure 18. Comparison of the Goodman MTF at Different Slant Angles. Perpendicular to the surface, the Goodman MTF is least significant and parallel to the surface, most significant. In all cases, the Goodman MTF is small scale.

## IV. METHODS AND DATA SETS

### A. SELECTION OF DATA LOCATIONS

This study compares MRTDs for marine and desert environments, with and without an included MTF for atmospheric turbulence. Since this study is only an initial comparison, only two sites were selected for analysis. Because of access to accurate data, the White Sands Missile Range in New Mexico was selected for the desert environment and Buoy 46063, just off Point Conception near Santa Barbara, CA was selected for the marine environment. Although the two locations differ in nearly all atmospheric conditions, the critical difference is between the surface temperature and the ambient air temperature. As explained in Section III.A, the temperature structure parameter is the largest contributor to variations in the atmospheric structure parameter.

### B. SELECTION OF ATMOSPHERIC DATA

Atmospheric data for inclusion in TAWS and for calculation of parameters in FLIR92 and NVThermIP were obtained from several sources. For the land locations, atmospheric data was obtained from the *Weather Underground* website, [www.wunderground.com](http://www.wunderground.com). The website provided all the needed TAWS inputs. An extreme example of the surface temperature and ambient air temperature at White Sands was provided by Rick Sharkey and cohorts at the White Sands facility. These input parameters are given in Table X.

For the atmospheric data over marine locations, observations from ships and buoys were used. The team at AFWA provided ship data and upper air analysis for the Point Conception region. The input parameters are given in Table XI

In both cases, data was obtained for 27 Aug 07, at 2030 GMT.

Table X. Atmospheric Parameters around White Sands.

<i>Atmospheric Parameter</i>	<i>Value</i>	<i>Units</i>
Ambient Air Temperature	35	°C
Surface Air Temperature	75	°C
Ambient Relative Humidity	.33	fraction
Surface Relative Humidity	1.0	fraction
Ground Type	sand	–
Wind Speed	3.1	m/s
Wind Direction	27°	NNE
Surface Pressure	1003	hPa
Visibility	16	km
Lower Level Clouds	2000	m
Lower Level Cloud Type	Scat	–
Mid Level Clouds	none	–
Upper Level Clouds	3700	m
Upper Level Cloud Type	Scat	–

## C. SELECTION OF TARGET LOCATIONS

In each case studied, the target location entered into TAWS corresponded to a coordinates of a nearby region. These coordinates are summarized in Table XII.

## D. PROCEDURES

In this study, the MRTD was calculated for chosen atmospheric conditions using both FLIR92 and NVThermIP.

### 1. Parameters Used in Calculations

The parameters used for the FLIR92 and NVThermIP calculations are listed in tables in Appendix D. Whenever possible, the same inputs were used in FLIR92 and NVThermIP.

### 2. FLIR92 Calculations

The FLIR92 calculations were two-fold. First, a MatLab version of the current operational FLIR92, supplied by Dr. Andy Goroch, was used. Then the MatLab version of FLIR92 was modified to include atmospheric turbulence. In order to deter-

Table XI. Atmospheric Parameters around Point Conception.

<i>Atmospheric Parameter</i>	<i>Value</i>	<i>Units</i>
Ambient Air Temperature	25	°C
Surface Air Temperature	31	°C
Ambient Relative Humidity	.55	fraction
Surface Relative Humidity	1.0	fraction
Ground Type	water	–
Wind Speed	3.7	m/s
Wind Direction	290°	WNW
Surface Pressure	1016	hPa
Visibility	16	km
Lower Level Clouds	none	–
Mid Level Clouds	none	–
Upper Level Clouds	none	–

Table XII. Target Locations.

The target coordinates are entered into TAWS.

<i>Location</i>	<i>Coordinates</i>
N White Sands Range	33°47'10"N;106°27'47" W
Buoy 46063, Pt Conception	34°16'21"N;120°41'55" W

mine the Monin-Obukhov length and  $T_*$ ,  $q_*$ , and  $u_*$ , certain atmospheric conditions were entered into the MatLab FLIR92 program, as outlined in Table XIII below. Most actual values depended on the atmospheric conditions and are listed later for the specific cases.

Table XIII. Atmospheric Condition Variables for Input into Modified FLIR92.

<i>Variable</i>	<i>Units</i>
Air Temp	°C
Sfc Temp	°C
Rel Humidity Air	fraction
Rel Humidity Sfc	fraction
Wind Speed	m/s
Sfc Pressure	hPa
Thermal Sfc Roughness	0.2 m
Momentum Sfc Roughness	0.2 m

### **3. NVThermIP Calculations**

No modifications to NVThermIP were made, but the output was modified as discussed in Section I.1.C.

### **4. TAWS Calculations**

The resultant MRTD curves were entered into TAWS version 5.2 and the maximum range detection results from TAWS were compared. The target used in TAWS was the 155 mm M795, a projectile in a black plastic bag. The sensor used in TAWS was the generic 1000 IR sensor, modified with the MRTD outputs from either FLIR92 or NVThermIP. Weather inputs are given in Tables X and XI. The test cases were run at a height of 100 m.

For the MRTD input, a table of spatial frequency and corresponding MRTD result was inserted into TAWS. The FLIR92 output had a larger frequency interval than NVThermIP. To account for this, the NVThermIP MRTD results were interpolated onto the FLIR92 results. Thus, the same number of frequency-MRTD pairs were entered for both the NVThermIP and FLIR92 cases.



## V. RESULTS

### A. ATMOSPHERIC TURBULENCE IN FLIR92

The modified FLIR92 including an MTF for atmospheric turbulence with a varying dependence on  $C_n^2$ , was compared to the original FLIR92. The inputs are given in Appendix D with the atmospheric inputs for the modified FLIR92 given in Section IV.B for White Sands, NM. The resultant MRTDs and system MTFs were compared in the horizontal and vertical directions, as shown in Tables XIV and XV.  $M$  indicates the modified FLIR92 with atmospheric turbulence,  $O$  the original.  $f_s$  is in  $\text{mrad}^{-1}$ .

Table XIV. MRTD for Modified, Original FLIR92 in the horizontal direction. The  $M$  indicates the modified FLIR92 while the  $O$  indicates the original FLIR92.  $f_s$  is in  $\text{mrad}^{-1}$  and the MRTD is in  $K$ .

$f_s$	$MRTD_M$	$MTF_{sys_M}$	$MRTD_O$	$MTF_{sys_O}$
0.9935	0.0013	0.8214	0.0013	0.8214
2.9804	0.0054	0.4874	0.0054	0.4875
4.9674	0.0155	0.2429	0.0155	0.2429
6.9543	0.0453	0.1008	0.0453	0.1008
8.9413	0.1511	0.0343	0.151	0.0343
10.9283	0.6072	0.0094	0.6069	0.0094
12.9152	3.13	0.0019	3.1284	0.002
14.9022	23.2345	0.0003	23.2193	0.0003

Figure 19 illustrates how the difference between the modified and original FLIR92 is only apparent at higher frequencies. Even so, the scale indicates how small is the impact of including atmospheric turbulence in the MRTD calculation.

There is a difference in resultant MRTD when including the atmospheric turbulence MTF, as seen at the higher frequencies, so starting at 10.9283 cycles/mrad in the horizontal case. The difference is minimal, though, less than 0.2% of the horizontal MRTD and vertical MRTD. The difference is too small to impact the range calculation in TAWS since the input for MRTD in TAWS is only of accuracy  $10^{-3}$  K.

Table XV. MRTD for Modified, Original FLIR92 in the vertical direction. The  $M$  indicates the modified FLIR92 while the  $O$  indicates the original FLIR92.  $f_s$  is in  $\text{mrad}^{-1}$  and the MRTD is in  $K$ .

$f_s$	$MRTD_M$	$MTF_{sys_M}$	$MRTD_O$	$MTF_{sys_O}$
0.9935	0.0013	0.8254	0.0013	0.8254
2.9804	0.0053	0.5094	0.0053	0.5095
4.9674	0.014	0.2751	0.014	0.2751
6.9543	0.0365	0.1295	0.0364	0.1295
8.9413	0.1023	0.0528	0.1023	0.0528
10.9283	0.3224	0.0185	0.3222	0.0185
12.9152	1.1786	0.0054	1.178	0.0054
14.9022	5.2264	0.0013	5.223	0.0013
16.8891	30.9544	0.0002	30.9296	0.0002

Again, Figure 20 indicates the differences at higher frequencies and the small scale of the differences.

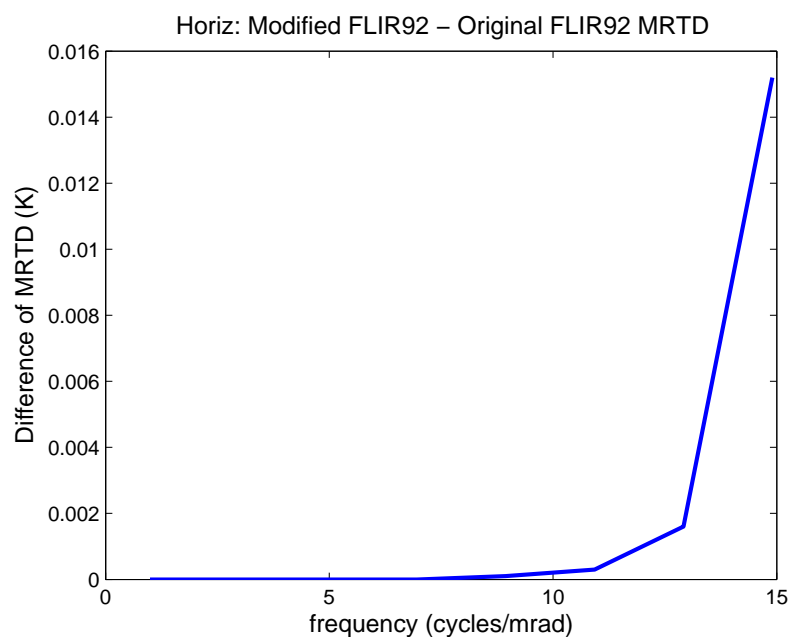


Figure 19. Horiz Difference Between MRTD Curves for Modified, Original FLIR92. Differences are not observed until higher frequencies.

## B. COMPARING FLIR92 AND NVTHERMIP

### 1. Comparing Resultant MRTDs

The modified FLIR92 MRTD, including an MTF for atmospheric turbulence with a varying dependence on  $C_n^2$ , was compared to NVThermIP. As explained in Section I.1.C, the CTF results from NVThermIP were used to find a comparable MRTD. From both FLIR92 and NVThermIP, the MRTD results were split into horizontal and vertical MRTDs. Comparisons of the horizontal MRTD show fairly similar results, as seen in Figure 21. The downturn on the FLIR92 MRTD curve is due to insufficient eye filtering. NVThermIP attempts to compensate for this weakness, and the difference is apparent in the upturning curve at low frequencies. Overall, the NVThermIP MRTD is greater because NVThermIP includes an improved and less pessimistic calculation to incorporate the human visual response to the display (see Section B.1.n).

Comparing the vertical MRTD, as in Figure 22, shows that once again at low

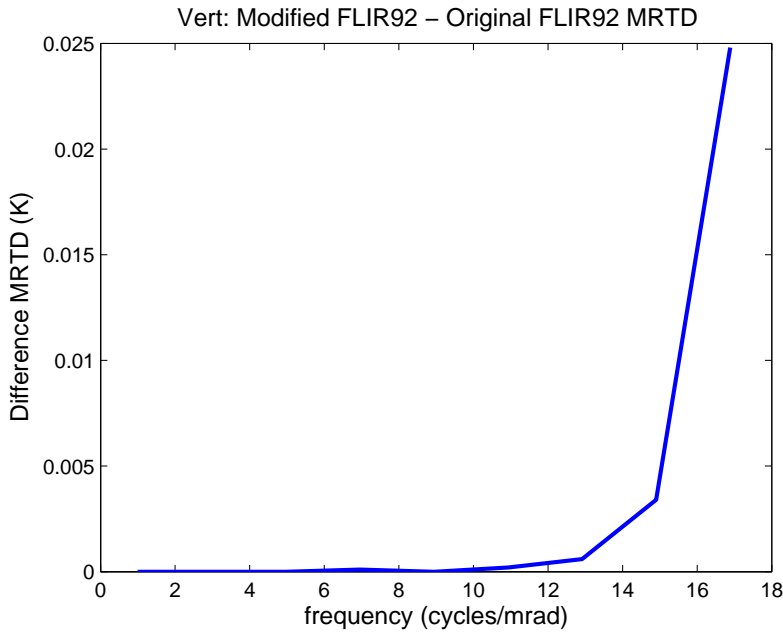


Figure 20. Vert Difference Between MRTD Curves for Modified, Original FLIR92. Differences are not observed until higher frequencies.

spatial frequencies, FLIR92 turns down while NVThermIP turns up. At high spatial frequencies, though, the two curves appear to agree closely in terms of slope and value. Because this study focuses on differences between the two MRTD models and the horizontal MRTD exhibits a greater difference, the horizontal MRTD is used as the input into TAWS.

## 2. Comparing Detection Range

The MRTDs were calculated with FLIR92 and NVThermIP for both White Sands and Point Conception.

The resultant maximum range detection from TAWS at 35%, 65%, and 95% probabilities, are compared for both the White Sands site and the Point Conception site. NVThermIP uses a constant atmospheric structure parameter.  $C_n^2$  was set

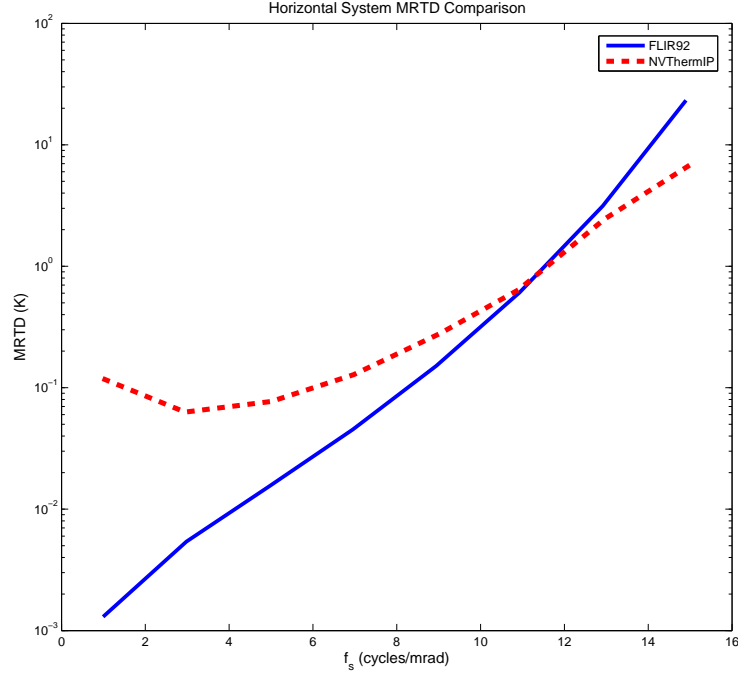


Figure 21. Horizontal MRTD Curves for FLIR92, NVThermIP. The horizontal MRTD curves have different behaviors at the low frequencies and high frequencies.

to  $10^{-14} \text{ m}^{-\frac{2}{3}}$  for both cases. Other inputs to TAWS are listed in Section IV.B. The White Sands case shows NVThermIP maximum detection range going from 0% to 1.5% greater than the FLIR92 maximum detection range, for all probabilities. In Figure 23, the maximum detection ranges at all probabilities for MRTD from NVThermIP (top) and FLIR92 (bottom) are shown.

Figure 24 better illustrates the differences between the maximum detection ranges calculated using the MRTDs from NVThermIP and FLIR92. The largest percent difference is at 35% probability of detection.

The Point Conception case shows NVThermIP maximum detection range going from 0% to 2% greater than the FLIR92 maximum detection range, for all probabilities. Figure 25 illustrates the maximum detection ranges for 35%, 65%, and 95% probabilities of detection based on the MRTDs from both NVThermIP (top) and FLIR92 (bottom).

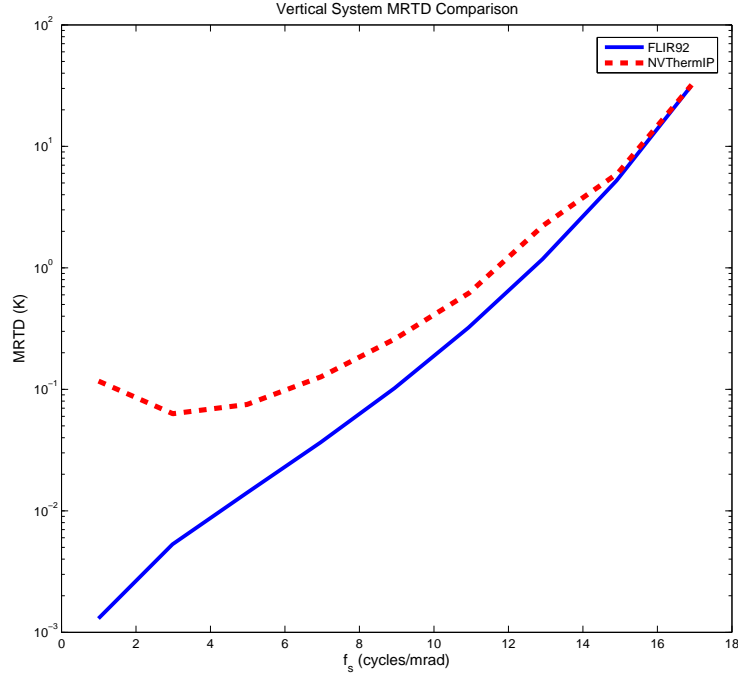


Figure 22. Vertical MRTD Curves for FLIR92, NVThermIP.

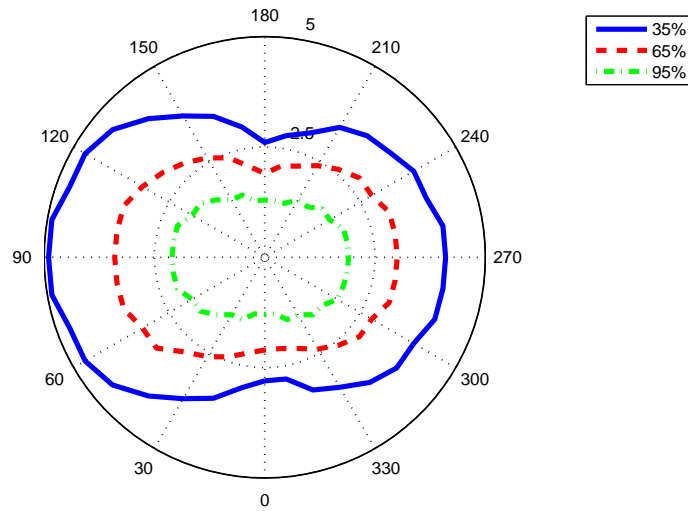
To better examine how the maximum detection ranges based on MRTDs from FLIR92 and NVThermIP compare, Figure 26 shows FLIR29 and NVThermIP maximum detection range results for each probability. The largest percent difference is again at 35% probability of detection.

### **3. Comparing Marine/Desert Conditions**

After comparing maximum detection ranges based on MRTD calculations from FLIR92 and NVThermIP, differences between maximum detection ranges at White Sands and Point Conception were compared. As shown in Figure 27, at 35% probability of detection, there is a greater difference between maximum detection range from the FLIR92 MRTD and the NVThermIP MRTD for Pt Conception. At 95% probability of detection, as shown in Figure 27, there is much less difference between maximum detection ranges using FLIR92 and NVThermIP MRTDs, but there is still an observable difference.

The difference between NVThermIP and FLIR92 at each location is better seen in the bar plots in Figures 28 and 29 showing the viewing angle versus the maximum detection range at 35% and 95% probabilities of detection respectively. The 35% case most clearly demonstrates that at White Sands, over the hot desert, there is the greatest difference in the maximum detection range between FLIR92 and NVThermIP, with NVThermIP having a greater range. At 95% probability of detection, the difference between the desert and the marine locations is much smaller.

NVThermIP Max Det Rng 35%, 65%, 95% Prob, White Sands NM



FLIR92 Max Det Rng 35%, 65%, 95% Prob, White Sands NM

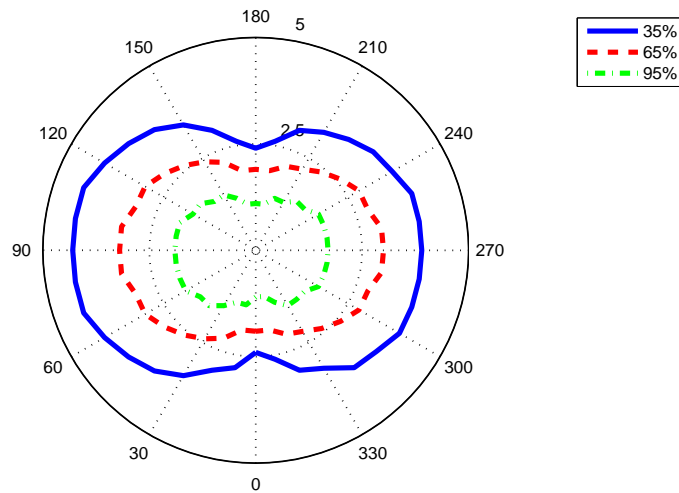


Figure 23. Comparing Maximum Detection Range at White Sands using FLIR92, NVThermIP.

Polar Plot of viewing angle (deg) versus maximum detection range (km) for 35%, 65%, and 95% probabilities of detection, using the MRTD from NVThermIP (top) and FLIR92 (bottom).

Max Det Rng 35%, 65%, 95% Prob White Sands

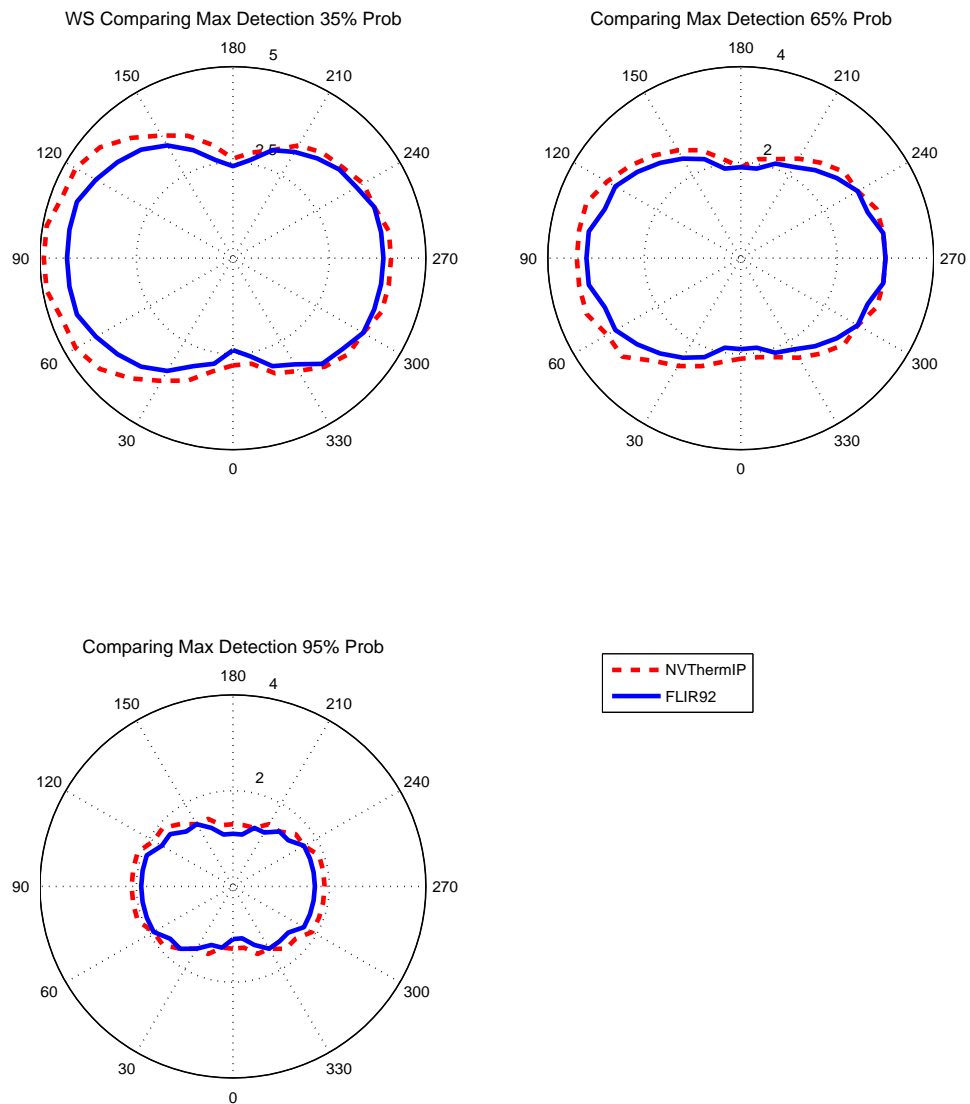


Figure 24. Maximum Detection Range for White Sands at Different Probabilities.  
Polar Plot of viewing angle (deg) and maximum detection range (km) for both  
FLIR92 and NVThermIP.



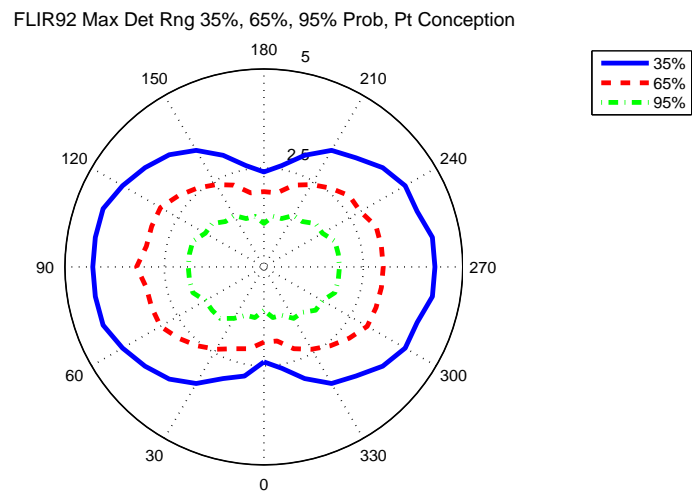
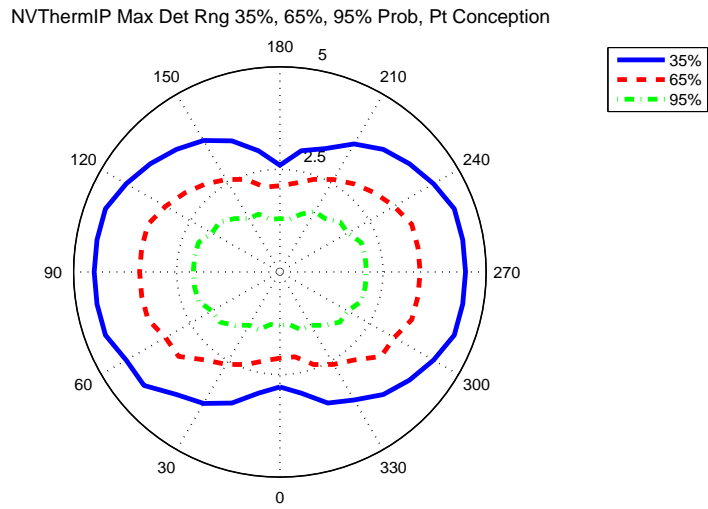


Figure 25. Comparing Maximum Detection Range at Pt Conception using FLIR92, NVThermIP.

Polar Plot showing view angle (deg) versus the maximum detection range (km) for 35%, 65%, and 95% probabilities of detection using MRTD from NVThermIP (top) and FLIR92 (bottom).

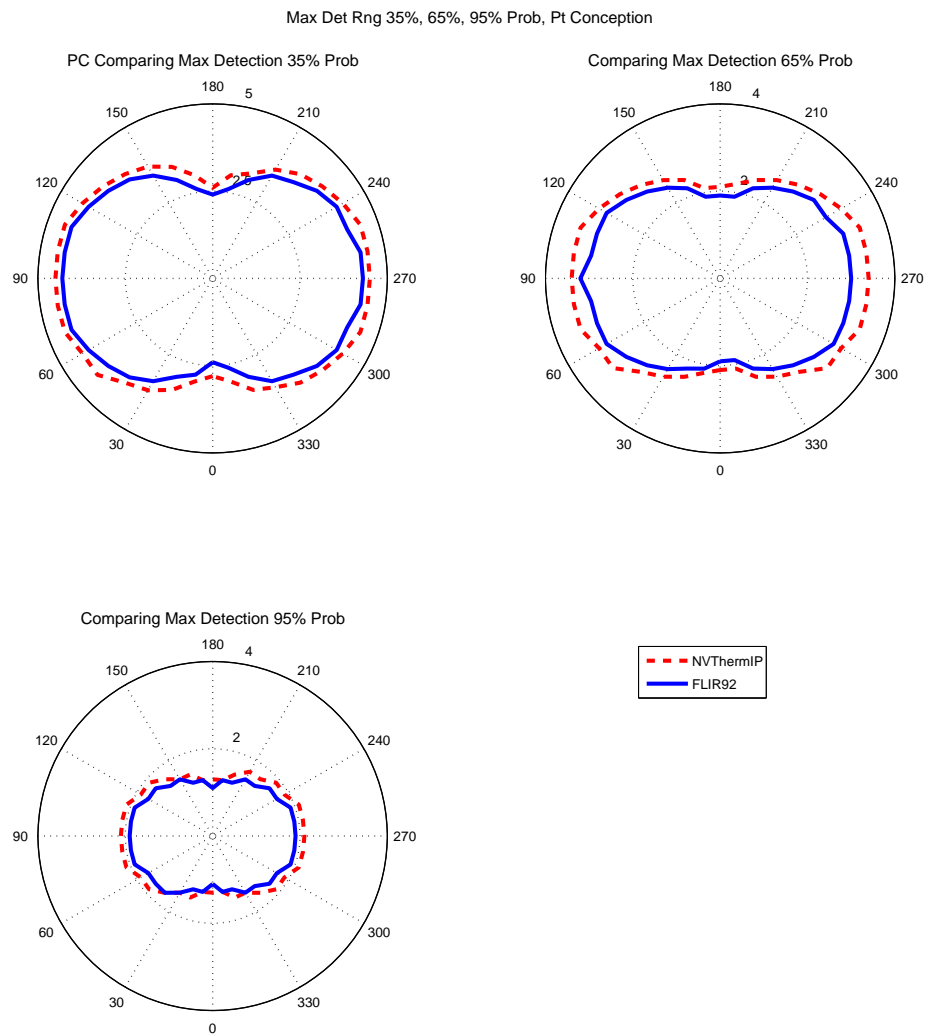


Figure 26. Maximum Detection Range for Pt Conception at Different Probabilities. Polar Plot showing view angle (deg) versus the maximum detection range (km) for both FLIR92 and NVThermIP.

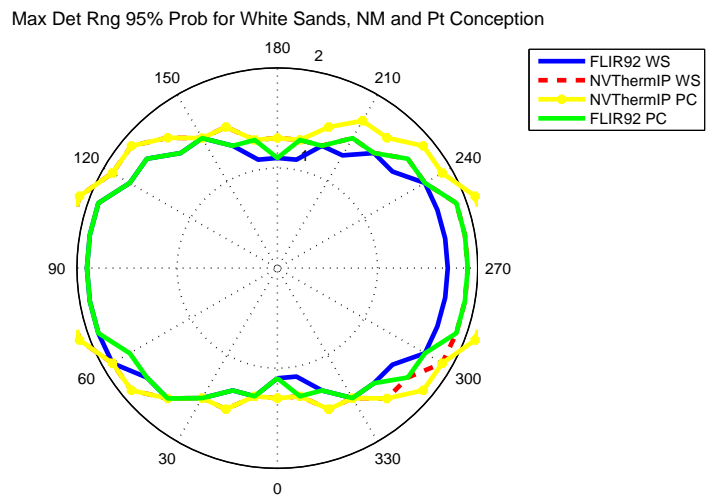
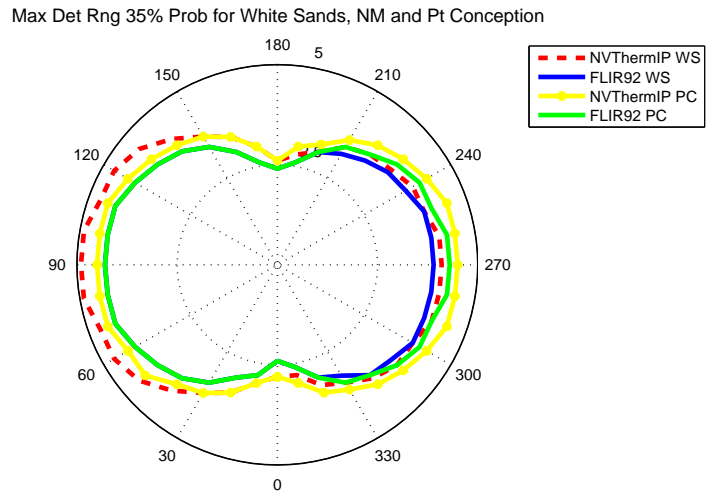


Figure 27. Comparing Maximum Detection Ranges at White Sands and Pt Conception at 35% Prob and 95% Prob.

Polar Plot showing view angle (deg) versus the maximum detection range (km) for both FLIR92 and NVThermIP at both White Sands (WS) and Pt Conception (PC) at 35% and 95% probabilities of detection.

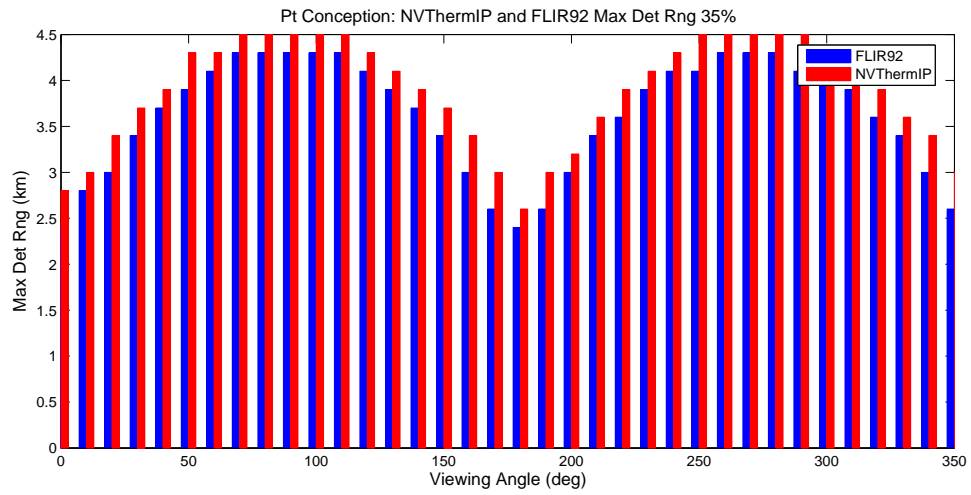
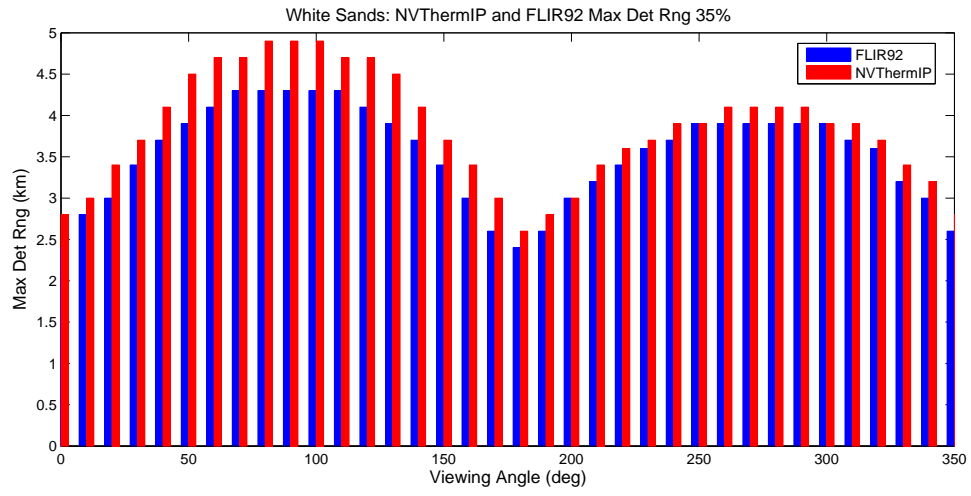


Figure 28. Comparing Maximum Detection Ranges at White Sands and Pt Conception at 35% Prob.

Bar plot showing view angle (deg) versus the maximum detection range (km) for both FLIR92 and NVThermIP at White Sands and Pt Conception at 35% probability of detection.

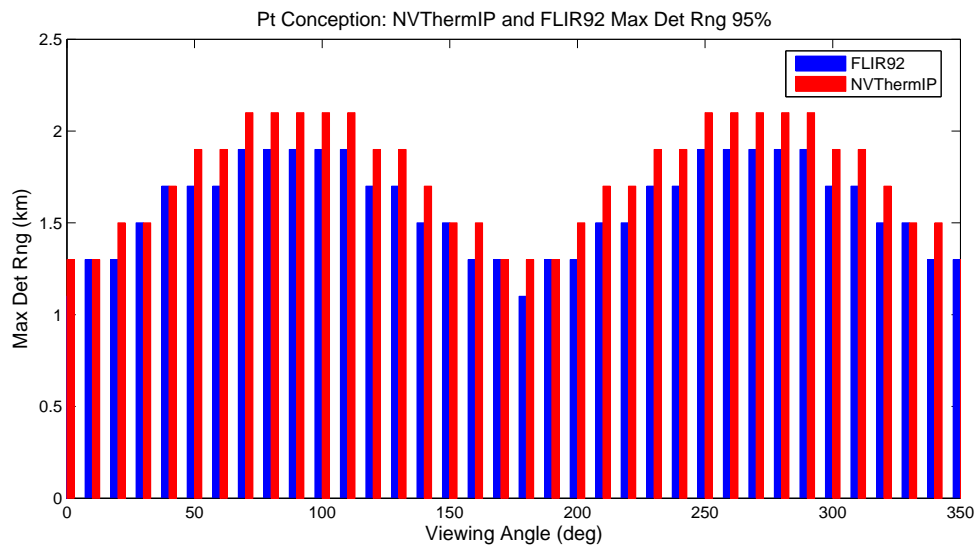
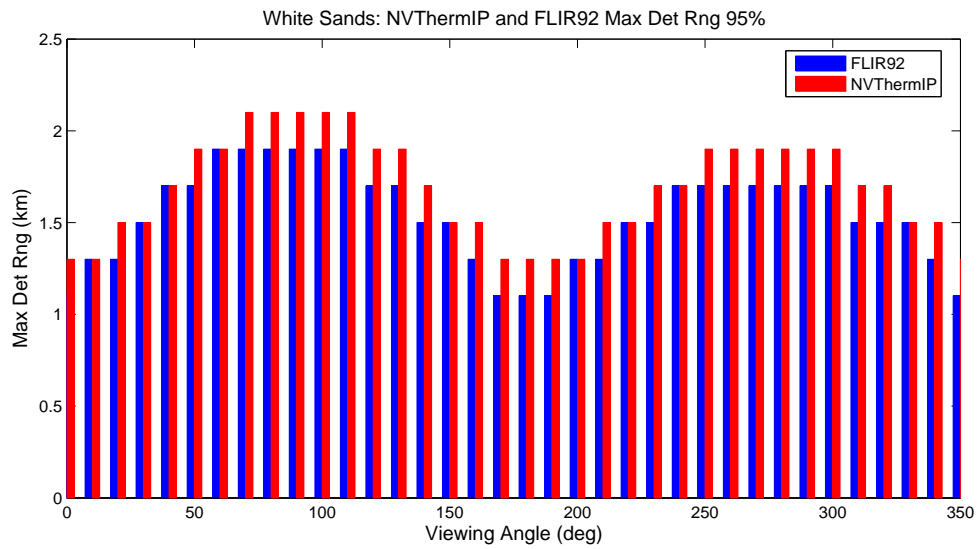


Figure 29. Comparing Maximum Detection Ranges at White Sands and Point Conception at 95% Prob.

Bar plot showing view angle (deg) versus the maximum detection range (km) for both FLIR92 and NVThermIP at White Sands and Pt Conception at 95% probability of detection.

THIS PAGE INTENTIONALLY LEFT BLANK

## VI. CONCLUSIONS AND RECOMMENDATIONS

This study considered two cases to test possible improvements to the MRTD input into TAWS. First, FLIR92 was modified to include atmospheric turbulence and the resultant MRTDs from the original and modified FLIR92 were compared. Initial results indicate that while there is a difference in including atmospheric turbulence in the MRTD calculation, the difference in most cases is too small to be significant. Second, FLIR92 and NVThermIP MRTD results were entered into TAWS and the resultant maximum detection ranges were compared. Again, the differences in the representative test cases were minimal. In comparing the FLIR92 and NVThermIP results in TAWS, the percentage improvement in using NVThermIP was slightly greater for the marine test case than for the desert test case.

### A. CONCLUSIONS FLIR92 WITH/WITHOUT ATMOSPHERIC TURBULENCE

The results using a test case as described in Chapter IV indicates very little difference in the MRTD when an atmospheric turbulence MTF is included in the total system MTF. The atmospheric turbulence MTF is very close to unity, on the order of  $1 - 10^{-7}$ , so the total system MTF is simply being multiplied by a factor of unity. In the Goodman long exposure MTF given in Equation A.103, the general form is an exponential that depends on  $f_s$ ,  $\lambda$ , and  $C_n^2(z)$  where  $z$  is the height in the atmosphere. Three possible cases exist where the atmospheric MTF may become significant. First, if the spatial frequency is very large, corresponding to imaging very small targets, the MTF may be significant. Second, if the diffraction wavelength is very small, well below the bounds of an IR study, the MTF may be significant. Finally, if  $C_n^2$  is large, at a minimum on the order of  $10^{-10} \text{ m}^{-\frac{2}{3}}$ , then the atmospheric MTF may become more important.

Near the surface where the bulk model is applicable,  $C_n^2$  depends on the ambient air and surface temperatures, wind speed, surface pressure, relative humidity, thermal surface roughness and momentum surface roughness as well as  $z^{-\frac{4}{3}}$ . Figure 30 shows that for the White Sands case near the surface,  $C_n^2$  is slightly greater than  $10^{-10} \text{ m}^{-\frac{2}{3}}$ , indicating that only very close to the surface may the atmospheric MTF be important. Too close to the surface, though, at less than 0.2 m, the bulk model for  $C_n^2$  including approximations for  $T_*$ ,  $u_*$ , and  $q_*$  may no longer be valid due to the extreme heat fluxes and bumps along the surface itself that are likely greater than the sensing height and will affect the scaling parameters.

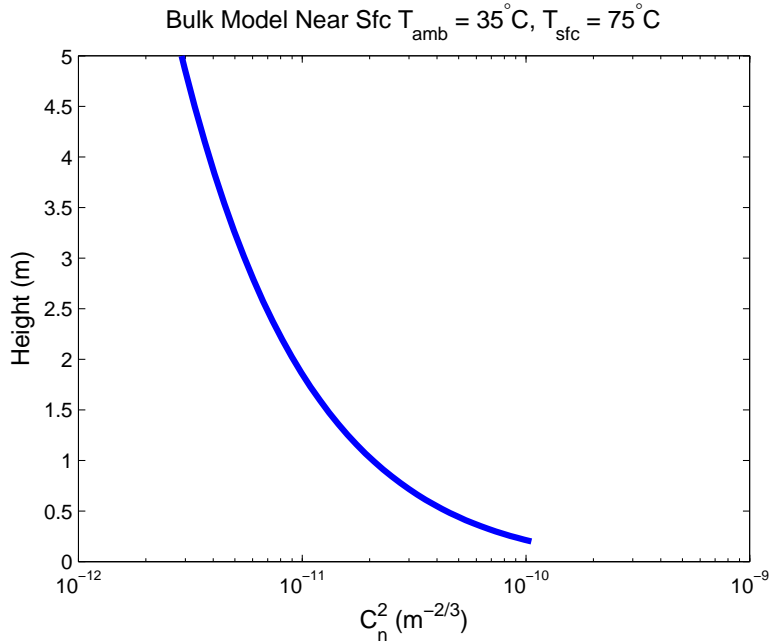


Figure 30. Near Surface Behavior of the Bulk Model. The height above the surface shown here is 0 to 1  $\mu\text{m}$ .

## B. CONCLUSIONS FLIR92 VERSUS NVTHERMIP

Comparing the maximum detection range using the horizontal MRTD from FLIR92 and NVThermIP, there is not a significant difference between the results in the marine environment and the results in a desert environment. In both cases,



the MRTD from NVThermIP yielded a greater maximum detection range by up to 2%, but the results did not even consistently improve by 2%. Figures 21 and 22 show substantial difference between FLIR92 and NVThermIP MRTD results, but apparently these differences do not significantly impact TAWS calculations.

### C. RECOMMENDATIONS

Since neither the modification of FLIR92 nor the use of NVThermIP instead of FLIR92 resulted in significant differences in TAWS, it seems best at the moment to continue using FLIR92 to calculate the MRTD for TAWS. However, should TAWS increase its sensitivity to the MRTD, the differences described in this study may become significant.

Including an atmospheric turbulence MTF in FLIR92 simply involves multiplying the total system MTF by the atmospheric MTF. Such a simple adjustment may prove useful for cases where  $C_n^2$  is large. The same adjustment could be made in NVThermIP, where the current atmospheric MTF assumes a constant  $C_n^2$ . In NVThermIP, the maximum  $C_n^2$  is  $10^{-10} \text{ m}^{-\frac{2}{3}}$  but using such a large  $C_n^2$  up through the atmosphere is highly unrealistic.

If the use of FLIR92 for MRTD calculations for TAWS continues, other modifications will need to be made. FLIR92 assumes a CRT display, but in many applications now the images are displayed on a flat panel. It is possible to enter a user-defined display MTF describing the flat panel, but updating the program would be a better solution.

THIS PAGE INTENTIONALLY LEFT BLANK

# APPENDIX A. GOODMAN DERIVATION FOR LONG EXPOSURE

The following derivation is primarily summarized from Goodman (1985), with substantiations from other sources.

A generally accepted form of the refractive index of air at optical frequencies is given by Goodman as

$$n = 1 + 77.6(1 + 7.52 \times 10^{-3} \lambda^{-2}) \frac{P}{T} \times 10^{-6} \quad (\text{A.67})$$

where  $\lambda$  is the wavelength of light in  $\mu\text{m}$ ,  $P$  is the atmospheric pressure in mb, and  $T$  is the atmospheric temperature in K. To simplify, consider that pressure variations are small compared to the temperature fluctuations at optical frequencies and so may be neglected. Then, choosing a representative  $\lambda = 0.5\mu\text{m}$ , it is apparent that for an incremental change  $dT$  of temperature,

$$dn = \frac{79P}{T^2} \times 10^{-6} dT. \quad (\text{A.68})$$

Inhomogeneities in the refractive index, otherwise described as turbulent eddies, can be considered individual packets of air with individual characteristic refractive indices. Then, the power spectral density of homogeneous turbulence,  $\Phi_n(\vec{\kappa})$ , where  $\vec{\kappa}$  is the vector wavenumber  $\vec{\kappa} = (\kappa_X, \kappa_Y, \kappa_Z)$ , yields a measure of the relative number of eddies of size  $L_X = \frac{2\pi}{\kappa_X}$  and  $L_Y = \frac{2\pi}{\kappa_Y}$  and  $L_Z = \frac{2\pi}{\kappa_Z}$ . For isotropic turbulence,  $\Phi_n(\kappa)$  is only a function of the non-vector wavenumber  $\kappa$  that corresponds to an eddy of size  $L$  where  $L = \frac{2\pi}{\kappa}$ .

In the classic theory of turbulence outlined by Kolmogorov (1961) and expanded by Goodman, the power spectral density consists of three different regions depending on the size of  $\kappa$ . Kolmogorov hypothesizes that the kinetic energy associated with the larger eddies will be redistributed to successively smaller and smaller eddies without loss of energy. For the smallest  $\kappa$ , corresponding to large scales since

$\kappa = 1/\lambda$ , turbulence depends on large-scale topographic and meteorological conditions. This makes it unlikely that the turbulence would be isotropic or homogeneous, so no mathematical form of turbulence is predicted in this region. Once  $\kappa$  grows beyond some critical wave number  $\kappa_0$ ,  $\Phi_n(\kappa)$  can be determined by physical laws governing how the large turbulent eddies break up into smaller ones. In this region beyond  $\kappa_0$ , the so-called inertial subrange of the spectrum, the power density spectrum may be written as

$$\Phi_n(\kappa) = \frac{1}{30} C_n^2 \kappa^{-\frac{11}{3}} \quad (\text{A.69})$$

where again  $C_n^2$  is the atmospheric structure constant. Goodman further defines  $C_n^2$  as the structure constant of the refractive index fluctuations and a measure of the strength of the fluctuations. In the third region, beyond another critical wave number  $\kappa_m$ , turbulent eddies are very small scale and viscous forces may cause them to dissipate their energy. This inner scale of the turbulence results in rapid decay of  $\Phi_n$  where  $\kappa > \kappa_m$ . The decay can be modeled as

$$\Phi_n(\kappa) = \frac{1}{30} C_n^2 \kappa^{-\frac{11}{3}} \exp\left(-\frac{\kappa^2}{\kappa_m^2}\right). \quad (\text{A.70})$$

Tatarski (1961) points out that this model is only valid when for the inner scale of the turbulence,  $l_0 \cong \frac{2\pi}{\kappa_m}$ ,  $\kappa_m$  is chosen equal to  $\frac{5.92}{l_0}$  and  $\kappa > \kappa_0$ . The above expression approaches infinity at the origin, so Goodman uses the von Kármán spectrum instead. This form also accounts for the finite amount of air in the atmosphere and does not become arbitrarily large as  $\kappa$  goes to 0. Approximated, the von Kármán spectrum yields a power spectrum density of

$$\Phi_n(\kappa) \cong \frac{C_n^2}{30(\kappa^2 + \kappa_0^2)} \exp\left(-\frac{\kappa^2}{\kappa_m^2}\right) \quad (\text{A.71})$$

and Goodman emphasizes that this mathematical form is only an artificial means of avoiding the poles. The von Kármán spectrum depends on the critical wave numbers in both the medium and small size turbulent eddies. Figure 31 illustrates the form of the von Kármán spectrum compared to the Kolmogorov spectrum.

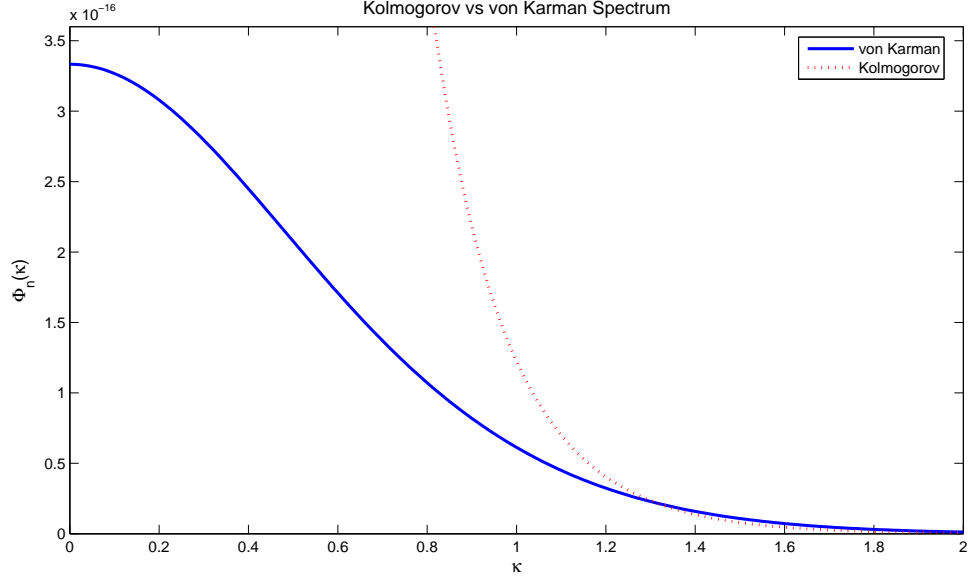


Figure 31. The Kolmogorov and von Kármán Spectra.

The Kolmogorov spectrum approaches infinity as  $\kappa$  goes to zero, but the von Kármán spectrum avoids the division by zero and has a finite value at  $\kappa = 0$ .

The structure function of the refractive index fluctuations in the case of atmospheric turbulence in imaging systems is defined as

$$D_n(\vec{r}_1, \vec{r}_2) = \langle [n_1(\vec{r}_1) - n_1(\vec{r}_2)]^2 \rangle \quad (\text{A.72})$$

where  $n_1$  is the random refractive index and  $\vec{r} = \vec{r}_1 - \vec{r}_2 = (\Delta x, \Delta y, \Delta z)$ . Assuming homogeneous turbulence,

$$D_n(\vec{r}) = 2[\Gamma_n(0) - \Gamma_n(\vec{r})] \quad (\text{A.73})$$

where the autocorrelation function  $\Gamma_n$  may be expressed as

$$\Gamma_n(\vec{r}) = \iiint_{-\infty}^{\infty} \Phi_n(\vec{\kappa}) \exp(-j\vec{\kappa} \cdot \vec{r}) d^3\vec{\kappa} \quad (\text{A.74})$$

and it follows that

$$\Gamma_n(0) = \iiint_{-\infty}^{\infty} \Phi_n(\vec{\kappa}) d^3\vec{\kappa}. \quad (\text{A.75})$$

Combining, then,

$$D_n(\vec{r}) = 2 \iiint_{-\infty}^{\infty} [1 - \exp(-j\vec{\kappa} \cdot \vec{r})] \Phi_n(\vec{\kappa}) d^3\vec{\kappa}. \quad (\text{A.76})$$

Assuming a real solution so the exponential simplifies to  $\cos(\vec{\kappa} \cdot \vec{r})$ , and when  $\Gamma_n(\vec{r})$  is spherically symmetric and  $n_1$  is statistically isotropic, the Fourier transforms of the power density function and the autocorrelation function may be expressed as single integrals. In this case, for  $\kappa = \sqrt{\kappa_x^2 + \kappa_y^2 + \kappa_z^2}$  and  $r = \sqrt{(\delta x)^2 + (\delta y)^2 + (\delta z)^2}$ ,

$$\Gamma_n(\vec{r}) = \frac{4\pi}{r} \int_0^{\infty} \Phi_n(\kappa) \kappa \sin(\kappa r) d\kappa. \quad (\text{A.77})$$

Then the structure function  $D_n$  simplifies:

$$D_n(r) = 2\Gamma_n(0) - 8\pi \int_0^{\infty} \Phi_n(\kappa) \frac{\kappa}{r} \sin(\kappa r) d\kappa. \quad (\text{A.78})$$

To determining  $\Gamma_n(0)$ , the limit as  $r \rightarrow 0$  is taken,

$$\lim_{r \rightarrow 0} \Gamma_n(r) = \lim_{r \rightarrow 0} 4\pi \int_0^{\infty} \Phi_n(\kappa) \kappa^2 \frac{\sin(\kappa r)}{\kappa r} d\kappa. \quad (\text{A.79})$$

Then, since the integral does not depend on  $r$ , the limit may be moved inside the integral to find

$$\lim_{r \rightarrow 0} \Gamma_n(r) = 4\pi \int_0^{\infty} \Phi_n(\kappa) \kappa^2 \lim_{r \rightarrow 0} \frac{\sin(\kappa r)}{\kappa r} d\kappa. \quad (\text{A.80})$$

Taking the limit,  $\Phi_n(r)$  as  $r$  approaches 0 is found to be

$$\lim_{r \rightarrow 0} \Gamma_n(r) = 4\pi \int_0^{\infty} \Phi_n(\kappa) \kappa^2 d\kappa \quad (\text{A.81})$$

which yields a  $D_n(r)$  of

$$D_n(r) = 8\pi \int_0^{\infty} \Phi_n(\kappa) \kappa^2 \left[ 1 - \frac{\sin(\kappa r)}{\kappa r} \right] d\kappa. \quad (\text{A.82})$$

Assuming that the power density has the form of Equation A.69, the structure function may be simplified to

$$D_n(r) = \frac{8\pi}{30} C_n^2 \int_0^{\infty} \kappa^{-\frac{5}{3}} \left[ 1 - \frac{\sin(\kappa r)}{\kappa r} \right] d\kappa. \quad (\text{A.83})$$

Equation A.83 is integrated using the integral identity

$$\int_0^\infty x^\nu \left(1 - \frac{\sin(ax)}{ax}\right) dx = \frac{-\Gamma(\nu) \sin(\frac{\pi\nu}{2})}{a^{1+\nu}} \quad (\text{A.84})$$

where  $-3 < \nu < -1$ . It is valid to use Equation A.84 because in this case  $\nu = -\frac{5}{3}$ , so

$$D_n(r) = \frac{8\pi}{30} \left[ -\Gamma\left(-\frac{5}{3}\right) \sin\left(-\frac{5\pi}{6}\right) \right] C_n^2 r^{\frac{2}{3}} \quad (\text{A.85a})$$

$$D_n(r) = 1 \times C_n^2 r^{\frac{2}{3}} = C_n^2 r^{\frac{2}{3}} \quad (\text{A.85b})$$

where the coefficient of unity in Equation A.85b is due to the chosen definition of  $C_n^2$ .

Goodman's derivation continues as follows by determining the optical transfer function (OTF). The derivation will be summarized here, but the specific details are available in Goodman's text (1985). The MTF for atmospheric turbulence is simply the modulus of the OTF, and can easily be calculated. In this case, the OTF is a real value, so the modulus of the OTF is the same as the OTF, so the MTF equals the OTF. This derivation focuses on long-exposure systems where the exposure time is much greater than one one-hundredth of a second. The short-exposure case can also be significant in applications but is neglected in this study. Also, the long-exposure OTF is assumed to be identical to the ensemble-averaged OTF. Using this assumption, Goodman derives a total average OTF of the form

$$\overline{OTF}(\nu) = \overline{OTF}_0(\nu) \overline{OTF}_L(\nu) \quad (\text{A.86})$$

where  $\nu = \sqrt{\nu_U^2 + \nu_V^2}$  and  $\nu_U$  and  $\nu_V$  are spatial frequency variables. To simplify the derivation, a circularly symmetric OTF is assumed, and the long-exposure OTF of the atmosphere,  $\overline{OTF}_L$ , has the form,

$$\overline{OTF}_L = \exp \left[ -\frac{1}{2} D(\bar{\lambda} f \nu) \right] \quad (\text{A.87})$$

where again  $D(\bar{\lambda} f \nu)$  is the wave structure function,  $\bar{\lambda} = \frac{c}{\bar{\nu}}$  where  $c$  is the speed of light, and  $\bar{\nu}$  is the center frequency of the waveband under consideration.

In the near-field calculation of the wave structure function, a detailed expression for the wave structure function is necessary to specifically define the form of the long-exposure atmospheric OTF. Three assumptions are made.

First, the target is assumed to be very far away from the detector lens. In this way, the angular extent of the target is small enough that over the long time average, the entire target is affected uniformly by the atmosphere. This assumption is considered the 'isoplanatic' assumption, in other words assuming that the point spread function is uniform over the entire FOV. In the long-time-average, this assumption is probably a close approximation to truth and thus is not very restrictive.

Second, the atmospheric turbulence is assumed to be homogeneous and isotropic over a finite distance  $z$  in front of the detector imaging lens. This assumption is invalid when considering vertical viewing, which is a problem for situations such as an aircraft imaging a ground-based target. This assumption will be removed later though, as  $C_n^2$  varies over the pathlength.

Third, the imaging system is assumed to be so far within the near field of the relevant turbulent eddies that each ray incident on the inhomogeneous medium may be approximated to merely be delayed by that medium with no bending of the rays. In other words, the turbulence is considered weak enough that no significant amplitude scintillation effects occur. This assumption is only valid when  $z \ll \frac{l_0^2}{\lambda}$ . Clearly, in actual practice this assumption is also unrealistic, but will be removed later.

Without going into the details of the derivation, these assumptions are used to find that the wave structure function equals the phase structure function and the atmospheric OTF may be equivalently expressed in Equation A.87 and below in Equation A.88,

$$\overline{OTF}_L = \exp \left[ -\frac{1}{2} D_S(\bar{\lambda} f \nu) \right] \quad (\text{A.88})$$



where of course  $D_S(\bar{\lambda}f\nu)$  is the phase structure function. Using the covariance functions  $C_n$ , not to be confused with the atmospheric structure constant  $C_n^2$ ,

$$D_S(r) = \bar{k}^2 \int_0^z dz' \int_0^\infty \left[ 2C_{co}(z' - z'') - 2C_n \sqrt{(z' - z'')^2 + r^2} \right] dz'' \quad (\text{A.89})$$

where  $z$  again is the distance from the target to the imaging lens. The difference of the covariance functions may further be expressed as a difference of structure functions,  $D_n$ ,

$$D_S(r) = \bar{k}^2 \int_0^z dz' \int_0^z \left[ D_n \sqrt{(z' - z'')^2 + r^2} - D_n(z' - z'') \right] dz'' \quad (\text{A.90})$$

Using the simplification that the integrand is an even function of  $z' - z''$ , the double integral may be reduced to a single integral such that with  $\Delta z = z' - z''$ ,

$$D_S(r) = 2\bar{k}^2 \int_0^z (z - \Delta z) \left[ D_n \sqrt{(\Delta z)^2 + r^2} - D_n(\Delta z) \right] d(\Delta z). \quad (\text{A.91})$$

Next, the specific form of the structure function that was found above, Equation A.85b, is substituted into Equation A.91 to yield an expression for the phase structure function,

$$D_S(r) = 2\bar{k}^2 C_n^2 \int_0^z (z - \Delta z) \left[ ([\Delta z]^2 + r^2)^{\frac{1}{3}} - [\Delta z]^{\frac{2}{3}} \right] d(\Delta z). \quad (\text{A.92})$$

Because Equation A.85b is only valid for  $l_0 < r < L_0$ , Equation A.92 is only valid for  $\Delta z < L_0$ . This makes it appear that Equation A.92 is only valid when the pathlength  $z$  is less than the outer scale  $L_0$ , but in the typical cases where the path separation  $r$  is less than  $L_0$ , the integrand vanishes for large  $\Delta z$  and it does not matter what was the exact form of the structure function for  $r > L_0$ . For  $\Delta z > L_0$  and  $r \ll L_0$ , the integrand approaches zero. Thus,  $D_S(r)$  can be used for all pathlengths without violating any already stated assumptions.

Since  $\Delta z$  is much less than  $z$ , Equation A.92 may be rewritten, neglecting the term of  $\Delta z$  multiplied by the rest of the integrand,

$$D_S(r) \cong 2\bar{k}^2 C_n^2 z \int_0^\infty \left[ ([\Delta z]^2 + r^2)^{\frac{1}{3}} - [\Delta z]^{\frac{2}{3}} \right] d(\Delta z) \quad (\text{A.93})$$

where the upper integration bound has been extended to  $\infty$  since from  $z$  to  $\infty$  barely contributes to the integrand. This integral may be evaluated numerically using a program such as Mathematica. First, a change of variables makes the integral expression clearer:  $\Delta z = ru$  and  $d\Delta z = rdu$ ,

$$D_S(r) = D_S(r) = \bar{k}^2 C_n^2 z \int_{-\infty}^{\infty} \left[ (u^2 + 1)^{\frac{1}{3}} - u^{\frac{2}{3}} \right] du. \quad (\text{A.94})$$

Mathematica gives the result that

$$D_S(r) = 2.9143 \bar{k}^2 C_n^2 z r^{\frac{5}{3}}. \quad (\text{A.95})$$

Substituting Equation A.95 into the expression for the long-exposure atmospheric OTF, Equation A.88, the final expression for the long exposure atmospheric OTF is,

$$\overline{OTF}_L(\nu) = \exp \left[ -\frac{1}{2} \times 2.91 \bar{k}^2 C_n^2 z \left( \bar{\lambda} f \nu \right)^{\frac{5}{3}} \right]. \quad (\text{A.96})$$

To obtain a form of  $\overline{OTF}_L$  that is independent of the optical system, the OTF is expressed in terms of the frequency  $f_s$  measured in cycles/rad rather than  $\nu$  in cycles/m. In that case,  $f_s = f\nu$  and

$$\overline{OTF}_L(f_s) = \exp \left[ -\frac{1}{2} \times 2.91 \bar{k}^2 C_n^2 z \left( \bar{\lambda} f_s \right)^{\frac{5}{3}} \right]. \quad (\text{A.97})$$

To further simplify,  $\bar{k} = \frac{2\pi}{\lambda}$ , so Equation A.97 becomes

$$\overline{OTF}_L(f_s) = \exp \left[ -5.82 \frac{\pi^2 C_n^2 z f_s^{\frac{5}{3}}}{\lambda^{\frac{1}{3}}} \right]. \quad (\text{A.98})$$

The long exposure OTF is identical to the long exposure MTF since the MTF is merely the modulus of the OTF and in this case the modulus is equal to the OTF itself. Also, though the above result is limited to the three assumptions stated above, it may be generalized.

First, the assumption that refractive index perturbations only delayed rays rather than bending or diffracting them may be eliminated without any change to the long exposure OTF theory. Goodman proceeds through an analysis considering

the case of refractive index perturbations occurring within a finite region along the propagation path and then integrates along the entire propagation path. This generalization leads to exactly the same results as for the previous analysis, indicating that it is possible to consider cases where the rays diffract and bend as they pass through varying refractive indices.

Second, since variations in  $C_n^2$  occur frequently in practice, the assumption that the turbulence is uniform is removed. The analysis in Goodman examines smooth and slow variations to the atmospheric structure constant  $C_n^2$  over the path length in both the vertical and horizontal directions. Goodman points out that his analysis is an approximation, but has been verified with more rigorous methods. Since Goodman assumes a slow and smooth change in  $C_n^2$ , his method of determining the OTF considers a "quasihomogeneous" model for the structure function of the refractive index fluctuations,

$$D_n(\vec{r}_1, \vec{r}_2) = C_n^2 \left( \frac{\vec{r}_1 + \vec{r}_2}{2} \right) |\vec{r}_1 - \vec{r}_2|^{\frac{2}{3}} \quad (\text{A.99})$$

where  $l_0 < |\vec{r}_1 - \vec{r}_2| < L_0$  and  $\vec{r}_1$  and  $\vec{r}_2$  are vectors indicating the location of the changes in  $C_n^2$ . Clearly, in this assumed structure function of the refractive index fluctuations, significant changes in  $C_n^2$  only occur over distances greater than or equal to  $L_0$ . Assuming that the atmosphere can be divided into stacking layers of thickness  $\Delta z$  along the propagation path such that the fluctuations in log amplitude and phase in the different layers are uncorrelated, the wave structure function after passing through  $N$  layers may be expressed as,

$$D(r) = \sum_{i=1}^N D_i(r) \quad (\text{A.100})$$

where  $D_i$  is associated with the  $i$ th layer. Taking  $z_i$  to represent the  $z$  coordinate in the middle of the  $i$ th layer and using Equation A.97 for each individual layer wave structure function, the total wave structure function may be expressed as

$$D(r) = 2.91 \bar{k}^2 \sum_{i=1}^N C_n^2(z_i) \Delta z r^{\frac{2}{3}}. \quad (\text{A.101})$$

Generalizing because variations of  $C_n^2$  are assumed to be slow compared to the length  $\Delta z$ , replace the finite sum with the integral along the propagation path,

$$D(r) = 2.91 \bar{k}^2 r^{\frac{5}{3}} \int_0^z C_n^2(z') dz' \quad (\text{A.102})$$

where  $z'$  is the variable along the propagation path from 0 to  $z$ . Using Equation A.102 in the expression for the long exposure OTF, Equation A.88, the long-exposure OTF with a varying  $C_n^2$  is

$$\overline{OTF}_L(f_s) = \exp \left[ -5.82 \pi^2 f_s^{\frac{5}{3}} \frac{\int_0^z C_n^2(z') dz'}{\lambda^{\frac{1}{3}}} \right]. \quad (\text{A.103})$$

See Section III.A for details on the approximations for how  $C_n^2$  varies in the vertical.

## APPENDIX B. EXACT FORM EYE/BRAIN SPATIAL INTEGRATION

The complete expressions for the eye/brain system spatial integrations are given below, assuming the eye/brain spatially integrates over all frequencies within the yet undegraded image of the target. The first subscript in these equations is the direction of spatial integration. The second is the orientation of the MRTD target.

In scanning systems, for horizontal MRTD target patterns, the system spatial integrals are given in the horizontal and vertical spatial integration directions. In the horizontal,

$$E_{hh}(f_s) = \frac{v_s}{\Delta f_p} \int_0^\infty S(\nu) [H_{NF_h}(\nu)]^2 \left[ \frac{\sin\left(\frac{\pi\nu}{2f_s}\right)}{\frac{\pi\nu}{2f_s}} \right]^2 d\nu \quad (\text{B.1})$$

and in the vertical,

$$E_{vh}(f_s) = \frac{\delta_v}{s_v} \int_{-\infty}^\infty [H_{NF_v}(\nu)]^2 \left[ \frac{\sin\left(\frac{7\pi\nu}{2f_s}\right)}{\frac{7\pi\nu}{2f_s}} \right]^2 d\nu \quad (\text{B.2})$$

where  $H_{NF_h}(\nu)$  and  $H_{NF_v}(\nu)$  are the horizontal and vertical system noise filter MTF components as given in Equation 2.20,  $\Delta f_p$  is defined by Equation 2.24,  $s_v$  is the samples per detector vertical IFOV and  $\delta_v$  is the detector vertical IFOV in mrad.

For vertical MRTD target patterns in scanning systems, the system spatial integrals are given in the horizontal and vertical spatial integration directions. In the horizontal,

$$E_{hv}(f_s) = \frac{v_s}{\Delta f_p} \int_0^\infty S(\nu) [H_{NF_h}(\nu)]^2 \left[ \frac{\sin\left(\frac{7\pi\nu}{2f_s}\right)}{\frac{7\pi\nu}{2f_s}} \right]^2 d\nu \quad (\text{B.3})$$

and in the vertical,

$$E_{vv}(f_s) = \frac{\delta_v}{s_v} \int_{-\infty}^\infty [H_{NF_v}(\nu)]^2 \left[ \frac{\sin\left(\frac{\pi\nu}{2f_s}\right)}{\frac{\pi\nu}{2f_s}} \right]^2 d\nu. \quad (\text{B.4})$$

For horizontal MRTD target patterns in staring systems, the system spatial integrals are given in the horizontal and vertical spatial integration directions. In the horizontal,

$$E_{h_h}(f_s) = \frac{\delta_h}{s_h} \int_{-\infty}^{\infty} [H_{NF_h}(\nu)]^2 \left[ \frac{\sin\left(\frac{\pi\nu}{2f_s}\right)}{\frac{\pi\nu}{2f_s}} \right]^2 d\nu \quad (\text{B.5})$$

and in the vertical,

$$E_{v_h}(f_s) = \frac{\delta_v}{s_v} \int_{-\infty}^{\infty} [H_{NF_v}(\nu)]^2 \left[ \frac{\sin\left(\frac{7\pi\nu}{2f_s}\right)}{\frac{7\pi\nu}{2f_s}} \right]^2 d\nu \quad (\text{B.6})$$

where  $\delta_h$  is the detector horizontal IFOV in mrad and  $s_h$  is the samples per detector horizontal IFOV.

For vertical MRTD target patterns in staring systems, the system spatial integrals are given in the horizontal and vertical spatial integration directions. In the horizontal,

$$E_{h_v}(f_s) = \frac{\delta_h}{s_h} \int_{-\infty}^{\infty} [H_{NF_h}(\nu)]^2 \left[ \frac{\sin\left(\frac{7\pi\nu}{2f_s}\right)}{\frac{7\pi\nu}{2f_s}} \right]^2 d\nu \quad (\text{B.7})$$

and in the vertical,

$$E_{v_v}(f_s) = \frac{\delta_v}{s_v} \int_{-\infty}^{\infty} [H_{NF_v}(\nu)]^2 \left[ \frac{\sin\left(\frac{\pi\nu}{2f_s}\right)}{\frac{\pi\nu}{2f_s}} \right]^2 d\nu. \quad (\text{B.8})$$

## APPENDIX C. TEMPERATURE SCALING OF

$$\sigma_{TVH}$$

In order to scale  $\sigma_{tvh}$ , the model scales the detector spectral detectivity from 300 K to  $T_1$  where  $T_1$  is the new temperature. This scaling can only occur if the detector noise is limited by the incident background photon flux, in other words, the background limited in performance (BLIP) condition. The BLIP condition happens when the background photon flux is much greater than the signal flux, causing photon noise to be the dominant noise factor (Driggers 1999). The scaling of the detector spectral detectivity is given in Equation C.1,

$$D^*(\lambda, T_1) = D^*(\lambda, 300) \sqrt{\frac{\int_0^\infty Q_\lambda(\lambda, 300) d\lambda}{\int_0^\infty Q_\lambda(\lambda, T_1) d\lambda}} \quad (C.1)$$

where  $Q_v(\lambda, T)$  the spectral photon flux density where  $T = 300, T_1$ .  $Q_v(\lambda, T)$  is defined in photons/s/cm<sup>3</sup>.

For BLIP detectors, using this scaled  $D^*(\lambda, T_1)$ , and for non-BLIP detectors using the unscaled  $D^*$ , the appropriately temperature-scaled  $\sigma_{tv}$  is given as

$$(\sigma_{tvh})_{T_1} = (\sigma_{tvh})_{300} \frac{\int_{\lambda_1}^{\lambda_2} D^*(\lambda, 300) \frac{\partial W}{\partial T_{300}}(\lambda) d\lambda}{\int_{\lambda_1}^{\lambda_2} D^*(\lambda, T_1) \frac{\partial W}{\partial T_{T_1}}(\lambda) d\lambda}. \quad (C.2)$$

THIS PAGE INTENTIONALLY LEFT BLANK



## APPENDIX D. TABLES OF INPUTS TO FLIR92, NVTHERMIP

The salient inputs to NVThermIP are listed in Tables XVI, XVII, and XVIII. Inputs to NVThermIP are made in the form of a text file, so in the text file each entry is of the form ‘variable,value’ as in ‘SensorName,SensorTest1’ if SensorName is the variable and SensorTest1 is the value, or the name of the sensor being tested. Inputs to FLIR92 are listed in Tables XIX and XX. These inputs are made in a MatLab file. The values given are generic and correspond to no special case. The  $H$  stands for the horizontal direction and the  $V$  for the vertical direction. Atmospheric data changed for each case and is listed in a separate Tables X and XI given in Chapter IV. Note that calculations were carried out for a staring sensor.

Table XVI. Input Parameters NVThermIP Part I.

<i>Variable</i>	<i>Value</i>	<i>Units</i>	<i>Comments</i>
SensorName	SensorTest1	–	Any name okay
TypeOfImager	0	–	0 for Staring
SingleFrame	1	–	–
CutOnWavelength	3.3	$\mu\text{m}$	–
CutOffWavelength	5	$\mu\text{m}$	–
MagnificationIn	0	–	0, Calculated in NVThermIP
HorizontalFOV	0.48	deg	Same as FOV calc. in FLIR92
VerticalFOV	0.48	deg	Same as FOV calc. in FLIR92
FrameRate	30	Hz	–
VerticalInterlace	2	–	–
ElectronicInterlace	1	–	–
DiffWavelength	4.15	$\mu\text{m}$	–
AveOpticTrans	1	frac	–
FocalLengthIn	45.7	cm	–
FNumberIn	0	–	0, Calculated in NVThermIP
ApertureDiameterIn	15.2	cm	–
OpticsBlur	0.01	mrad	–
OpticsBlurUnits	0	–	0 for object space
OpticsBlurType	0	–	0 for RMS
VibBlurX	0.02	mrad	–

Table XVII. Input Parameters NVThermIP Part II.

<i>Variable</i>	<i>Value</i>	<i>Units</i>	<i>Comments</i>
VibBlurY	0.02	mrad	–
VibBlurType	0	–	0 for RMS
DetHorrDim	23	$\mu\text{m}$	–
DetVertDim	23	$\mu\text{m}$	–
PeakDstarIn	1E+12	$\text{cm}\sqrt{\text{Hz}}/\text{W}$	–
IntegrationTimeIn	7000	$\mu\text{s}$	–
NumTDI	1	–	–
ScanEfficiency	1	frac	–
NumHorrDet	512	–	–
NumVertDet	512	–	–
SamplesPerHIFOV	1.4	–	–
NoiseFactorX	0	–	0, Calculated in NVThermIP
NoiseFactorY	0	–	0, Calculated in NVThermIP
Sigmavh	0	–	0, Calculated in NVThermIP
Sigmav	0	–	0, Calculated in NVThermIP
Sigmah	0	–	0, Calculated in NVThermIP
FPN	0	–	0, none
PtSi	1	–	1, no
EmissionCoef	0	–	0, Calculated in NVThermIP
BarrierHeight	0	–	0, Calculated in NVThermIP
Uncooled	1	–	1, no
Dither	0	–	0, no
LowPass3dBCutoff	22000	Hz	–
LowPassFilterOrder	1	–	Number filter poles
NoiseGain	0	–	–
FrameIntegration	1	–	–
Interph	0	–	0, no H interpolation
Interpv	0	–	0, no V interpolation
InterpTypeh	0	–	0, no H interpolation
InterpTypev	0	–	0, no V interpolation
EZoom	0	–	0, no EZoom
EZoomType	0	–	0, no EZoom
Boosth	0	–	no H boost
Boostv	0	–	no V boost
DispType	0	–	0, CRT
EoMUX	1	–	1, no
HorLEDSIZE	0	cm	–
VertLEDSIZE	0	cm	–

Table XVIII. Input Parameters NVThermIP Part III.

<i>Variable</i>	<i>Value</i>	<i>Units</i>	<i>Comments</i>
CRTType	0	–	0, RMS
LEDHeight	0	cm	–
LEDWidth	0	cm	–
DispSpotHeight	0.02	cm	–
DispSpotWidth	0.02	cm	–
AveDispLum	10	ft-Lamberts	–
MinDispLum	0	ft-Lamberts	–
SceneContTemp	10	K	–
DispHeight	15.24	cm	–
DispViewDist	70	cm	–
NumEyes	2	–	–
AtmTransType	0	–	0, Beer's Law
AerosolModel	0	–	Not applicable, Beer's Law
ModelEnvironment	6	–	Not applicable, Beer's Law
TransPerKM	0.9	frac	–
TurbulenceIndex	1E-14	$\text{m}^{-\frac{2}{3}}$	–
AtmSmoke	1	–	1, no
AtmSensorAltitudeIn	1	km	–
AtmAlpha	1	$\text{m}^2/\text{g}$	not applicable, no smoke
AtmConcLen	1	$\text{m}^2/\text{g}$	not applicable, no smoke
NumSpectDetPtsIn	9	–	–
SpectDetWavelengthIn1	3.3	$\mu\text{m}$	Same as FLIR92
SpectDetWavelengthIn2	3.5	$\mu\text{m}$	Same as FLIR92
SpectDetWavelengthIn3	3.7	$\mu\text{m}$	Same as FLIR92
SpectDetWavelengthIn4	4.1	$\mu\text{m}$	Same as FLIR92
SpectDetWavelengthIn5	4.2	$\mu\text{m}$	Same as FLIR92
SpectDetWavelengthIn6	4.5	$\mu\text{m}$	Same as FLIR92
SpectDetWavelengthIn7	4.6	$\mu\text{m}$	Same as FLIR92
SpectDetWavelengthIn8	4.8	$\mu\text{m}$	Same as FLIR92
SpectDetWavelengthIn9	5	$\mu\text{m}$	Same as FLIR92
NormDStarIn1	0.66	$\mu\text{m}$	Same as FLIR92
NormDStarIn2	0.7	$\mu\text{m}$	Same as FLIR92
NormDStarIn3	0.74	$\mu\text{m}$	Same as FLIR92
NormDStarIn4	0.82	$\mu\text{m}$	Same as FLIR92
NormDStarIn5	0.84	$\mu\text{m}$	Same as FLIR92
NormDStarIn6	0.9	$\mu\text{m}$	Same as FLIR92
NormDStarIn7	0.92	$\mu\text{m}$	Same as FLIR92
NormDStarIn8	0.96	$\mu\text{m}$	Same as FLIR92
NormDStarIn9	1	$\mu\text{m}$	Same as FLIR92

Table XIX. Input Parameters for FLIR92 Part I.

<i>Variable</i>	<i>Value</i>	<i>Units</i>
Std Dev Optics Blur H Diam	0.01	mrad
Std Dev Optics Blur V Diam	0.01	mrad
H Cell Dimension	25	$\mu\text{m}$
V Cell Dimension	25	$\mu\text{m}$
Fields Per Frame	2	–
Detectors Disp H Dir	512	–
Detectors Disp V Dir	512	–
Sample and Hold Filter Dir	H	–
H Scene Sample Phase Ang	0	rad
V Scene Sample Phase Ang	0	rad
H Filter Cutoff Freq	0	cycles/mrad
V Filter Cutoff Freq	0	cycles/mrad
CCD H Charge Transfer Eff	1	–
CCD V Charge Transfer Eff	1	–
Active TV Lines Across Disp Ht	512	–
Display Frame Rate	30	Hz
Std Dev H Rand Image Motion Amp	0.02	mrad
Std Dev V Rand Image Motion Amp	0.02	mrad
Std Dev H Sinsdl Image Motion Amp	0	mrad
Std Dev V Sinsdl Image Motion Amp	0	mrad
Eye Limiting MTF	1	–
Thrshld SNR to Resolve 4-bar Tgt	2.5	–
Enviro Background Temp	290	K
Det 1/f knee freq	3	f
Band Avg Optics Transmission	1	–
Detect H Active Dim	23	$\mu\text{m}$
Detect V Active Dim	23	$\mu\text{m}$
Detector Integration Time	0.007	s
Tot Detectors H Direction	512	–
Tot Detectors V Direction	512	–
H FIR Digital Filter Type	none	–
V FIR Digital Filter Type	none	–
Display Height	0.1524	m
Display Luminance	10	ft-lamberts
Display Viewing Distance	0.7	m
Peak Det Detectivity 300K	$1 \times 10^{12}$	$\text{cmHz}^{\frac{1}{2}}/\text{W}$
Spectral Band Cuton $\lambda$	3.3	$\mu\text{m}$
Spectral Band Cutoff $\lambda$	5	$\mu\text{m}$

Table XX. Input Parameters for FLIR92 Part II.

<i>Variable</i>	<i>Value</i>	<i>Units</i>
Diffraction $\lambda$	4.15	$\mu\text{m}$
H Focal Length	457	mm
V Focal Length	457	mm
Optical Aperture H Diam	152	mm
Optical Aperture V Diam	152	mm
FPA Readout Frame Rate	30	Hz
Pathlength (sensor alt)	1000	m

THIS PAGE INTENTIONALLY LEFT BLANK

## APPENDIX E. ACRONYMS USED

Table XXI. Acronyms Used in this Study

<i>Acronym</i>	<i>Name</i>
CCD	Charge Coupled Device
CTF	Contrast Threshold Function
FLIR92	Forward Looking Infrared 92
FOV	Field of View
FPA	Focal Plane Array
IFOV	Instantaneous Field of View
IR	Infrared
MDTD	Minimum Detectable Temperature Difference
MRTD	Minimum Resolveable Temperature Difference
MTF	Modulation Transfer Function
NETD	Noise Equivalent Temperature Difference
NVThermIP	Night Vision Thermal and Image Processing
OTF	Optical Transfer Function
PSF	Point Spread Function
SPRITE	Signal Processing in the Element
TAWS	Target Acquisition Weapons Software
TTP	Targeting Task Performance

THIS PAGE INTENTIONALLY LEFT BLANK



## LIST OF REFERENCES

- [1] J. S. Accetta and D. L. Shumaker: editors. *Infrared and Electro-Optical Systems Handbook*. ERIM/SPIE Optical Engineering Press, Ann Arbor/Bellingham, 1993.
- [2] L. M. Biberman. *Perception of Displayed Information*. Plenum Press, New York, 1973.
- [3] G. D. Boreman and A. E. Plogstedt. Spatial Frequency Performance of SPRITE Detectors. *Proc. SPIE*, 1309:158–166, 1990.
- [4] K. L. Davidson, T. M. Houlihan, C. W. Fairall, and G. E. Schacher. Observation of the Temperature Structure Function Parameter,  $C_T^2$ , over the Ocean. *Boundary-Layer Meteorol.*, 15:507–523, 1978.
- [5] K. L. Davidson, G. E. Schacher, C. W. Fairall, and A. K. Goroch. Verification of the Bulk Method for Calculating Overwater Optical Turbulence. *Appl. Optics*, 20:2919–2924, 1981.
- [6] R. G. Driggers, P. Cox, and T. Edwards. *Introduction to Infrared and Electro-Optical Systems*. Artech House, Boston, 1999.
- [7] C. W. Fairall, K. L. Davidson, and G. E. Schacher. Meteorological Models for Optical Properties in the Marine Atmospheric Boundary Layer. *Opt. Eng.*, 21:847–857, 1982.
- [8] R. L. Fante. Electromagnetic Beam Propagation in Turbulent Media: And Update. *Proc. IEEE*, 65:1424–1443, 1980.
- [9] D. L. Fried. Optical Resolution Through a Randomly Inhomogeneous Medium for Very Long and Very Short Exposures. *J. Opt. Soc. Am.*, 56:1372–1379, 1966.
- [10] J. F. Goodman. *Introduction to Fourier Optics*. McGraw-Hill, Inc., San Francisco, 1968.
- [11] J. F. Goodman. *Statistical Optics*. John Wiley and Sons, Inc., New York, 1985.
- [12] A. K. Goroch. *Frequency of Occurrence of Atmospheric Turbulence Conditions Affecting USMC Modular Universal Laser Equipment*. Naval Environmental Prediction Research Facility, Monterey, 1980.
- [13] F. Hall. *Index of Refraction Structure Parameter in the Real Atmosphere*. Digest Printed by Optical Society of America, Boulder, 1977.

- [14] U.S. Army NVESD. *FLIR92 Thermal Imaging Systems Performance Model: User's Guide*. Visionics and Image Signal Processing Division, Fort Belvoir, VA, 1993.
- [15] U.S. Army NVESD. *Night Vision Thermal and Image Processing Performance Model: User's Manual*. Modeling and Simulation Division, Fort Belvoir, VA, 2005.
- [16] I. Overington. *Vision and Acquisition*. Crane, Russak and Co., Inc., New York, 1976.
- [17] L. Scott, J. A. D'Agostino, and C. Webb. Application of 3-D Noise to MRTD Prediction. *Proc. SPIE*, 2075, 1993.
- [18] V. I. Tatarski. *Wave Propagation in a Turbulent Medium*. McGraw-Hill Book Co, New York, 1961.
- [19] R. H. Vollmerhausen and E. Jacobs. *The Targeting Task Performance Metric*. NVESD Modeling and Simulation Division, Fort Belvoir, VA, 2004.
- [20] J. C. Wyngaard. On Surface-Layer Turbulence. *Workshop on Micrometeorology*, 1:101–149, 1973.
- [21] J. C. Wyngaard, Y. Izumi, and S. A. Collins. Behavior of the Refractive-Index-Structure Parameter near the Ground. *J. Opt. Soc. Am.*, 61:1646–1650, 1971.

## **INITIAL DISTRIBUTION LIST**

1. Defense Technical Information Center  
Ft. Belvoir, Virginia
2. Dudley Knox Library  
Naval Postgraduate School  
Monterey, California